ANALYTICAL AND EXPERIMENTAL STUDIES OF WING TIP VORTICES

By

Shizhong Duan

B. Sc. Tsinghua University, Beijing, 1984

M. Sc. Beijing University of Aeronautics and Astronautics, Beijing, 1987

A THESIS SUBMITTED IN PARTIAL FULFILLMENT OF
THE REQUIREMENTS FOR THE DEGREE OF
DOCTOR OF PHILOSOPHY
in
THE FACULTY OF GRADUATE STUDIES
MECHANICAL ENGINEERING

We accept this thesis as conforming
to the required standard

THE UNIVERSITY OF BRITISH COLUMBIA

September 1995

In presenting this thesis in partial fulfillment of the requirements for an advanced degree at the University of British Columbia, I agree that the Library shall make it freely available for reference and study. I further agree that permission for extensive copying of this thesis for scholarly purposes may be granted by the head of my department or by his or her representatives. It is understood that copying or publication of this thesis for financial gain shall not be allowed without my written permission.

Mechanical Engineering
The University of British Columbia
2324 Main Mall
Vancouver, Canada
V6T 1Z4

Date : Oct. 13, 1995

Abstract

Wing tip vortices, and their relationship to wing tip geometry and wing total drag, are investigated here both analytically and experimentally. The purpose of the analysis is to answer the basic question — what are the effects of wing drag on tip vortex structure? The purpose of the experiments is to determine the effect of wing tip geometry on wing tip vortices (tip vortex cavitation) and wing drag (vortex induced drag).

In the analytical work, a new method has been developed for wing tip vortices. This approach is referred to as the "quasi-similarity" method. This new method combines a polynomial solution with a similarity variable technique. A non-linear analytical tip vortex model is achieved for the first time. The first order (linear) velocity components and pressure of the polynomial solution for the new model can be expressed in complete function form. Higher order (non-linear) velocity components and pressure can be obtained analytically or numerically. The most important feature of this new tip vortex model is that the predicted wing drag due to such a single vortex is finite. To the author's knowledge, no other vortex model has this property. At distances fairly far downstream of the wing, tip vortex structure is found to be an explicit function of wing total drag, vortex circulation, freestream velocity, downstream distance and fluid properties.

It is verified that the first order tangential velocity component and pressure of the tip vortex model are exactly the same as that of the linear wing tip vortex model proposed by Batchelor (1964). The decay of the axial and tangential velocity components predicted by this theory compare well with experimental measurements.

In the experimental work, a novel ducted tip device was tested in a wind tunnel and a water tunnel. The ducted tip consists of a hollowed duct attached to the tip of a rectangular untwisted wing. This novel tip device was found to improve the Lift/Drag ratio by up to 6% at elevated angles of attack compared with a conventional round tip configuration with the same span. The wing tip vortex cavitation was substantially delayed by the ducted tip device. In view of its superior cavitation characteristics and aerodynamic performance, the ducted tip has potential application to marine propellers.

The ducted tip is effective because it redistributes the shed vorticity in the transverse plane (Trefftz plane) behind the wing. The shed vorticity is distributed along the wing and duct trailing edge for the ducted tip configuration, rather than solely along the wing trailing edge, which would be the case for a conventional wing tip configuration.

Table of Contents

List of Tables

Lists of Figures

Nomenclature

a_i	A constant for the i-th order problem
b	Wing span
b_i	A constant for the i-th order problem
c	Wing chord
C_D	Drag coefficient
Cf_i	A constant for the i-th order problem
Ch_i	A constant for the i-th order problem
c_i	A constant for the i-th order problem
$\overline{c}_p$	Pressure coefficient
C_L	Lift coefficient
D	Drag due to a single tip vortex
DAC	Dissolved air content [ppm]
D_w	Wing drag
$f(\eta)$	An arbitrary function
$f(z)$	An arbitrary function
$F_i(\eta)$	i-th order similarity function of axial velocity
$g(\eta)$	An arbitrary function
$G_i(\eta)$	i-th order similarity function of pressure
$H_i(\eta)$	i-th order similarity function of function ψ
$K(x)$	Vortex circulation
L	A constant in Batchelor's vortex
L_o	Operator for ordinary differential equations
L_p	Operator for partial differential equations
p	Pressure
p_v	Water vapour pressure
p_∞	Pressure at infinity
$P_i(z)$	i-th order amplitude function of pressure
$P_p(\xi)$	Similarity function for pressure in Batchelor's vortex

p_{ref}	Reference pressure
Q_1	A similarity function in Batchelor's vortex
Q_2	A similarity function in Batchelor's vortex
R	Radius of the control volume around a tip vortex
r	The radial distance from the vortex centerline
R_{1c}	The radius of a tip vortex
Re	Reynolds number
$R_i(\eta)$	i-th order similarity function of radial velocity
s	Distance between two trailing vortices
$T_i(\eta)$	i-th order similarity function of tangential velocity
U_∞	Freestream velocity
$U_i(z)$	i-th order amplitude function of axial velocity
$V_i(z)$	i-th order amplitude function of radial velocity
z	The axial distance along the vortex

Greek Symbols

β	A constant related to wing drag
ψ	A parameter defined as tangential velocity over the radius, υ_θ/r
λ	A positive number not far from unity
α	Angle of attack
ρ	Fluid density
ν	Kinematic viscosity
ξ	Similarity variable
η	Similarity variable
ζ	Similarity variable
ϕ	Stream function
θ	The azimuthal coordinate
Γ	Vortex circulation

υ_θ	Tangential velocity
$\varphi(z,r)$	An arbitrary function
Γ_0	Bound circulation at mid-span of a wing
β_i	A constant for the i-th order problem
α_i	A constant for the i-th order problem
σ_i	Cavitation inception index, $\sigma_i = (p_\infty - p_v)/0.5\rho U_\infty^2$
$\Psi_i(z)$	i-th order amplitude function of parameter ψ
υ_r	Radial velocity
υ_z	Axial velocity
ω_z	The axial vorticity

Acknowledgements

I would like to express my gratitude to my supervisor, Professor S. I. Green. His guidance throughout this program has been invaluable in finishing the work successfully.

I wish to express my sincere appreciation to Professor I. S. Gartshore, Professor P. G. Hill, Professor S. M. Calisal and Professor G. W. Bluman for their insightful discussions and suggestions. Thanks are also due to A. Schreinders, T. Besic, D. Camp, D. Bysouth and other technicians in the Mechanical Engineering Workshop for their skillful technical assistance in design and construction of the instruments and test models.

I wish also to thank Professor G. S. Schajer for proof-reading my thesis.

Financial support for this work by the Natural Science and Engineering Research Council of Canada and the University of British Columbia is gratefully acknowledged.

I would especially like to thank my parents, and my wife Belinda for their patience, love, faith and encouragement. It is to them that I dedicate this work.

Chapter 1 Introduction

Trailing vortices occur whenever a lifting surface terminates in a fluid. A simple explanation of the existence of trailing vortices derives from the application of Helmholtz vortex laws. Consider a finite length wing impulsively started from rest. For the simplest case, a lift line (with a constant circulation along the wing span) must exist in order for the wing to generate lift force. Kelvin's Theorem demands that this circulation be matched by an equal and opposite shed circulation (the "starting vortex"). Because vortex lines can never end in a fluid, these two vortices must be connected by tip vortices, as illustrated in Figure 1.1.

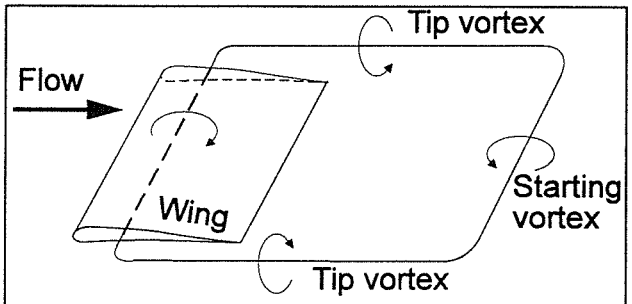

Figure 1.1 Helmholtz vortex laws interpretation of tip vortices.

A more realistic description involves a number of lifting lines distributed along the wing chord and span, as depicted in Figure 1.2. As a result of this distribution of lifting lines, a sheet of vorticity is shed by the wing. Such a vortex sheet is not stable; roll-up of the sheet occurs. The free edge of the sheet curls over, under the influence of the induced velocity field of the vortex sheet, and takes the form of a spiral with a continually increasing number of turns in the downstream direction (Figure 1.3). It has now been well established that trailing vortices generated by wings roll up exceptionally quickly. In general, roll up is complete, i.e. vortex circulation is virtually independent of downstream distance, 1-2 chords downstream of the trailing edge of an airfoil (Shekarriz et al. 1992, Stinebring et al. 1991, Green and Acosta 1991). Contraction of vorticity in a plane transverse to the freestream during roll-up results in an axial velocity in the vortex core. After the shed vorticity is fully

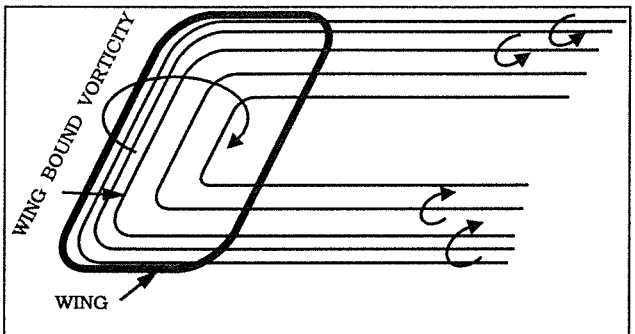

Figure 1.2 Shed vorticity from a finite wing.

rolled up, there are only two concentrated trailing vortices behind a finite wing — consistent, coincidentally, with the conclusion that resulted from the simplest interpretation of Helmholtz vortex laws.

1.1 Motivation for Tip Vortex Research

The wing tip vortex flow is one of great importance because it occurs often in practical problems. These problems include: landing separation distances for aircraft at runways — one airplane may experience a dangerous rolling moment if it accidentally flies into the tip wake of another (Donaldson 1971, Kantha et al. 1971, Snedeker 1972, Barber et al. 1975); blade/vortex interactions on helicopter blades, which is an undesirable source of noise and vibration (Martin et al. 1984, Summa 1982, Mosher and Peterson 1983, Lewy and Caplot 1982, Widnall and Wolf 1980); and propeller cavitation on ships due to the relatively low pressure in the vortex core (Ligneul and Latorre 1993, Arndt and Keller 1992, Chahine et al. 1993, Arndt et al. 1991).

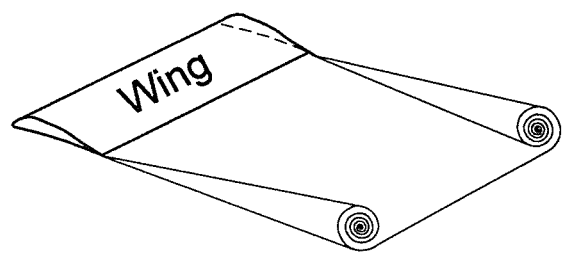

Figure 1.3 Rolling-up of a trailing vortex sheet.

In the following airplane problem, the tip vortices generated by one aircraft may be sufficiently strong that a following plane accidentally entering into one of the vortices experiences a loss of control. This accidental interaction is most likely to occur during aerial refueling and over airport runways. Critchley (1991) has documented that serious incidents involving such interactions occur at an average rate of 9 per year at Heathrow airport! The cost of maintaining sufficient plane separation distances on landing to limit the frequency of such hazardous interactions is about $10 million annually for every major airport (Winter 1991).

Helicopter rotor blades generate strong tip vortices. If the helicopter is hovering, following rotor blades will pass through the tip vortex generated by leading blades. In passing through the tip vortex, the following blade experiences large fluctuating forces

(due to the unsteady aerodynamic loading) that can cause premature rotor blade fatigue and excessive blade noise (Poling et al. 1989).

Finally, there is a tendency for tip vortices generated in marine applications to cavitate even at elevated inception indices (refer to section 1.4 for the definition of cavitation inception). The reason for the high values of cavitation inception index, σ_i, may be traced to the fact that the vortical motion is particularly strong (large $\upsilon_\theta / U_\infty$) in tip vortices. In order to sustain these large tangential velocities (and hence extremely high centripetal accelerations), there exists a large radial pressure gradient from the vortex core to the surrounding fluid. If the freestream pressure is low enough, or the tangential velocity is high, the pressure in the vortex core will locally fall below the water vapour pressure and cavitation may occur.

In every application, tip vortices act as lifting surface inefficiencies. Flow downwash caused by the vortices decreases the effective incidence angle of the wing. This tilting of the local incoming flow causes the lift force, which is perpendicular to the incoming flow direction, also to be tilted. The component of the lift force in the undisturbed freestream direction is the wing induced drag (Figure 1.4). Induced drag on wings is a particularly salient issue. Approximately 35% of the drag on a typical aircraft is lift-induced drag (Webber and Dansby 1983). Due to the small aspect ratio of marine propellers, induced drag on propellers is likely to be a greater percentage of the overall drag than in aeronautical applications. The potential savings to be reaped by reducing airplane induced drag, even fractionally, are staggering — roughly $100 million/year worldwide for each 1% induced drag reduction. Tip clearance flow in axial flow fans (Ruden 1974) and compressors (Raines 1954) decreases their efficiency. An understanding of the tip vortex flow is also pertinent to the design of propfan blades (Vaczy and McCormick 1987). Tip flow even plays an important role in the design of America's Cup yacht keels (Devoss 1986).

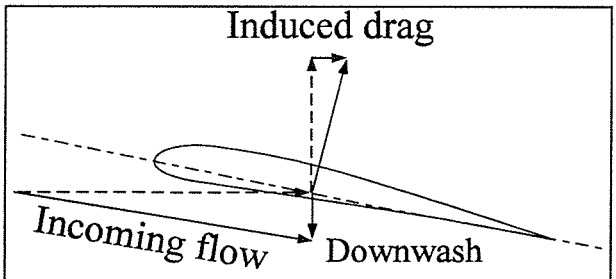

Figure 1.4 Induced drag acting on a finite wing.

1.2 Previous Measurements on Tip Vortex Structure

Attempts have been made to measure the tangential and axial velocity distributions around trailing vortices using Laser Doppler Velocimetry (LDV) (Orloff and Grant 1973, Baker et al. 1974, Higuchi et al.1986a), hot wire anemometers (Corsiglia et al. 1973, Chigier and Corsiglia 1972, Zalay 1976), five-hole or seven-hole probes (McCormick 1968, Logan 1971, Chow et al., 1993), and Particle Image Velocimetry (PIV) (Green 1987, Shekarriz et al. 1992, 1993). Any intrusive method used to measure tip vortices is subject to large experimental errors because tip vortices are extremely sensitive. LDV is accurate locally, but there is a risk, due to its small measurement volume and the tendency of trailing vortices to meander, that the measurement volume may miss the target. This unsteady movement of trailing vortices may lead to a large overall measurement error when LDV is employed. Particle Image Velocimetry (PIV) has the distinct advantage that particle tracers move with the vortex. Although the local accuracy of PIV is not as high as LDV, the overall error of PIV is possibly the lowest among all the methods discussed above. In view of the sensitivity of vortices to disturbances and their tendency to meander, one must view with suspicion many of the early experimental studies of tip vortices.

More recent studies, though, have produced some reliable and interesting results. For example, Pauchet et al. (1993) have measured vortex core axial velocities as big as 2.5 times the freestream velocity within two chord-lengths downstream of a particular hydrofoil. This axial velocity increases with the angle of attack, α. Typical vortex core radii (the radius at which the tangential velocity is a maximum) are approximately $0.01\bar{c}$, where $\bar{c}$ is the wing average chord (Green and Acosta 1991). This radius increases only slowly with downstream distance.

Further downstream, viscosity leads to a slow diffusive increase of the core diameter. The gradual slowing-down of the azimuthal motion by viscous action leads to an increased pressure at the axis (there being less centrifugal force then), and so to an axial deceleration of the core fluid (Batchelor 1964). It is found experimentally that the

tangential velocity decays slowly with downstream distance, whereas the axial velocity decays much faster. (Green 1991, Pauchet et al. 1993, Shekarriz et al. 1993). Maximum tangential velocities around the core in excess of U_∞ (Arndt et al. 1991) have been measured.

Much further downstream, trailing vortices typically "demise" after undergoing the Crow instability (Crow 1970). This instability takes the form of long wavelength sinusoidal disturbances on the vortex in fixed planes 48° from the wing planform. Eliason, Gartshore and Parkinson (1975) have verified experimentally the Crow instability. The amplitude of the disturbance grows in time. Following growth of the sinusoidal instability, the trailing vortices "link" in the regions where the two vortices approach most closely. Linking of vortices is followed closely by the formation of vortex rings. Vortex rings usually form hundreds or thousands of chord-lengths downstream of a wing; once vortex ring formation has occurred, the trailing vortex dissipates rapidly (Sarpkaya and Daly 1987).

The wing tip vortices are also known to be highly unsteady. The axial velocity on the centerline can fluctuate with an r.m.s amplitude up to $0.2U_\infty$ (Green and Acosta 1991).

Wing tip or strake vortices generated by delta wings may undergo an unusual phenomenon known as vortex "breakdown" or "bursting" (Peckham and Atkinson 1957). A stagnation point appears suddenly in the vortex core as vortex breakdown happens (normally at high angles of attack) and the flow downstream immediately becomes unsteady and irregular. The lift drops drastically and an asymmetrical rolling moment appears which may result in a loss of control.

1.3 Previously Developed Mathematical Models of Vortices

Mathematical models of vortex behaviour have become increasingly more sophisticated and realistic with the passage of time. The earliest and simplest model of an isolated vortex is the "Rankine vortex." The Rankine vortex model is a two region model of a vortex. The vortex core moves in solid body rotation ($r \leq r_c$), and the region outside

the core is irrotational. The vortex is purely two-dimensional and axisymmetric, with only a tangential velocity:

$$\upsilon_z(z,\theta,r) = 0$$

$$\upsilon_r(z,\theta,r) = 0$$

$$\upsilon_\theta(z,\theta,r) = \begin{Bmatrix} \Gamma r / 2\pi r_c^2 & r \le r_c \\ \Gamma / 2\pi r & r > r_c \end{Bmatrix}$$

$$p_\infty - p(z,\theta,r) = \begin{Bmatrix} \dfrac{\rho\Gamma^2}{4\pi^2 r_c^2} - \dfrac{\rho\Gamma^2 \cdot r^2}{8\pi^2 r_c^4} & r \le r_c \\ \dfrac{\rho\Gamma^2}{8\pi^2 r^2} & r > r_c \end{Bmatrix}$$

The Rankine vortex does not satisfy the Navier-Stokes equations; at $r = r_c$ the velocity gradient is discontinuous. Nonetheless, the pressure field result for a Rankine vortex is instructive — the pressure at the centerline falls with $1/r_c^2$. The pressure (and thus cavitation characteristics) of a Rankine vortex is very sensitive to r_c.

The diffusion of a two-dimensional axisymmetric vortex was analyzed by Oseen(1912). At time t = 0 an irrotational line vortex ($\upsilon_\theta = \Gamma / 2\pi r$) is placed in a viscous fluid. Viscosity causes the vorticity to diffuse radially in time:

$$\upsilon_z(z,\theta,r,t) = 0$$

$$\upsilon_r(z,\theta,r,t) = 0$$

$$\upsilon_\theta(z,\theta,r,t) = (\Gamma / 2\pi r) \cdot \left[1 - \exp(-r^2 / 4\nu t)\right]$$

The "Lamb-Oseen" vortex is an exact solution to the Navier-Stokes equation. The solution shows that viscous growth of a vortex is very slow; the core size varies as $\sqrt{4\nu t}$.

The Rankine and Lamb-Oseen models are both vortex models for which the axial velocity is zero. More complex vortex models that incorporate axial flow in the vortex have been developed. The "Burgers Vortex" (Burgers 1948) models the flow around a vortex that is stretched in the axial direction. The three velocity components in the Burgers vortex are

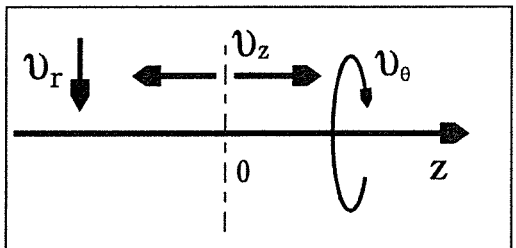

Figure 1.5 Burgers vortex model.

(refer to Figure 1.5):

$$\upsilon_z(z,r,t) = 2Cz$$

$$\upsilon_r(z,r,t) = -Cr$$

$$\upsilon_\theta(z,r,t) = \frac{\Gamma}{2\pi r}\cdot\left[1-\exp\left(\frac{-r^2}{4\delta^2}\right)\right]$$

This velocity field has associated vorticity distribution:

$$\omega_z(z,r,t) = \frac{\Gamma}{4\pi\delta^2}\cdot\exp\left(\frac{-r^2}{4\delta^2}\right)$$

where $\delta^2 = \frac{\nu}{2C} + \left(\delta_0^2 - \frac{\nu}{2C}\right)\cdot\exp(-2Ct)$.

The Burgers vortex solution reveals that axial stretching of vortex lines (e.g. as occurs immediately downstream of a wing) decreases the growth in vortex core size that arises from viscosity.

Long (1961) extended the work of Burgers by considering a viscous vortex in an infinite liquid. Similarity arguments lead to a solution for this viscous vortex,

$$\phi = \nu\cdot z\cdot f(\zeta), \qquad \upsilon_\theta = \frac{\Gamma}{r}\cdot k(\zeta), \qquad p = -\frac{\rho\cdot\Gamma^4}{\nu^2\cdot z^2}\cdot s(\zeta)$$

$$\upsilon_z = \frac{\Gamma}{\sqrt{2}\cdot r}\cdot f'(\zeta), \qquad \upsilon_r = -\frac{\nu}{r}\cdot f(\zeta) + \frac{\Gamma}{\sqrt{2}\cdot z}\cdot f'(\zeta)$$

where $\zeta = \frac{\Gamma\cdot r}{\sqrt{2}\cdot\nu\cdot z}$, and ϕ is the stream function. The similarity functions f, k, and s satisfy a set of ordinary differential equations. Long integrated these ODEs numerically, and found that the self-similar profiles have different characteristic shapes, depending on the value of the non-dimensional momentum transfer, M, given by:

$$M = \frac{1}{\Gamma^2}\cdot\int_0^\infty\left(\frac{p}{\rho} + \upsilon_z^2\right)\cdot 2\pi r\cdot dr$$

Batchelor (1964) has deduced the dynamical necessity of axial flow in a tip vortex core. In order to maintain the centripetal acceleration around the vortex, the pressure in the core of a trailing vortex is lower than that upstream of the wing. Thus, in the absence of viscous effects, fluid particles on a streamline originating ahead of the wing and entering the core are accelerated in the downstream direction (based on Bernoulli's

equation, flow velocity increases on a favorable-pressure-gradient streamline). Relative to the fluid at rest at infinity, the fluid in the core moves in a direction opposite to the direction of flight. In a coordinate system fixed to the wing, the component of velocity in the direction of the flow at infinity is increased in the core. Batchelor showed that a Rankine vortex with maximum tangential velocity $\upsilon_\theta = kU_\infty$ has maximum axial velocity in the vortex core $(\upsilon_z)_{\max} = U_\infty \cdot \sqrt{1+2k^2}$. In Batchelor's paper, a partly-linear theory was developed to predict the axial flow in a wing tip vortex core. The axial velocity deficit or excess was considered to be much smaller than the freestream velocity. Then, the tangential momentum equation could be linearized, and the following asymptotic form of the tangential velocity was obtained:

$$\upsilon_\theta(z,r) = \frac{C_0}{r} \cdot \left[1 - \exp\left(-\frac{U_\infty \cdot r^2}{4\nu z}\right)\right]$$

where C_0 is a constant, U_∞ is the freestream velocity, and ν is the kinematic viscosity.

By integrating all terms of the linearized axial momentum equation, Batchelor suggested the following asymptotic solution for the axial velocity in a wing tip vortex.

$$\upsilon_z(z,r) = U_\infty - \frac{C_0^2}{8\nu z} \cdot \log\frac{zU_\infty}{\nu} \cdot Q_1(\xi) + \frac{C_0^2}{8\nu z} \cdot Q_2(\xi) - L\frac{U_\infty^2}{8\nu z} \cdot e^{-\xi}$$

where $\xi = \dfrac{U_\infty^2 \cdot r^2}{4\nu z}$ and L is a constant related to any initial velocity defect which may be independent of the circulation.

Batchelor studied the vortex wake far downstream, where it decays under the action of viscosity. The vortex radius is $O(\nu z / U_\infty)^{0.5}$. Batchelor found that viscous effects produce an axial velocity deficit in the far field.

The principal limitations of Batchelor's theory are that it is only valid at large distances downstream of the vortex-generating wing, and that the theory requires that the axial velocity deficit or excess be much smaller than the freestream velocity. As described previously, the latter assumption is often violated by the flow around real wing tip vortices.

Moore and Saffman (1973) considered the structure of laminar trailing vortices rolling-up behind a wing. Their vortex structure consists of an inviscid roll-up region and

a viscous vortex core. For an elliptical loading case, the wing is replaced by a bound vortex along the wing span, $0 < x < b$, of strength

$$K(x) = \frac{2\Gamma_0}{b} \cdot [x(b-x)]^{\frac{1}{2}}$$

Kaden (1931) had remarked that roll up starts at the wing tips so that in the initial stages of the process, the rolled up portions at each end cannot significantly interact. Thus one can usefully consider a semi-infinite lifting line of circulation $K(x) = 2\gamma \cdot x^{\frac{1}{2}}$, where $\gamma = \Gamma_0 \cdot b^{-\frac{1}{2}}$. The vortex sheet rolls up into a spiral with an infinite number of turns and the velocity field near the centre of this spiral can be obtained by a simple argument — the velocity field, relative to the centre of the spiral, can be characterized by a distribution of circulation

$$\Gamma(r) = 2\gamma[\lambda \cdot r]^{\frac{1}{2}}$$

where λ is a constant. Thus if υ_θ is the transverse velocity relative to the centre of the spiral,

$$\upsilon_\theta = \gamma \cdot \frac{\lambda^{\frac{1}{2}}}{\pi \cdot r^{\frac{1}{2}}}$$

The pressure in the roll-up region is found by the radial equilibrium equation and is used to calculate the axial velocity, which is produced by streamwise pressure gradients. Moore assumed further that the tip loading is $2\gamma x^{1-n}$, where n is a positive constant and $0 < n < 1$. The case $n = 1/2$ represents elliptic loading. The axial velocity excess is then given by

$$w = (\upsilon_z - U_\infty) \sim \frac{\kappa^2}{2U_\infty} \cdot \left(\frac{1}{n} - 1\right) \cdot r^{-2n} \quad \text{at } r \to 0$$

provided $w << U_\infty$. κ is a constant. Note that $w > 0$, in agreement with Batchelor's general argument. However $w \to \infty$ as $r \to 0$. Therefore, the effect of viscosity has to be considered. Upon consideration of the viscosity, Moore and Saffman deduced that roll-up is 90% complete only tens of chords downstream of a wing, a result that differs from experiments (Shekarriz et al. 1992, Green and Acosta 1991). The discrepancy between theory and experiments may be due to their mathematical requirement that $|\upsilon_Z - U_\infty| << U_\infty$, which virtually never occurs in practice.

A class of self-similar solutions of the steady, axisymmetric Navier-Stokes equations, representing the flows in slender vortices was reported by Mayer and Powell (1992a). Such self-similar vortices will have constant axial velocity in the vortex core if the external axial flow is a constant (i.e. U_∞). In a wing tip vortex, the axial velocity in the vortex core decays along the downstream distance (based on experimental observations) while the freestream velocity is a constant, and hence wing tip vortices are not part of the family of self-similar vortices.

The inviscid and viscous stability of a vortex, which has the asymptotic structure obtained by Batchelor (1964), was first studied in the papers of Lessen et al. (1974a) and Lessen & Paillet (1974b). They used a Runge-Kutta-type scheme along with the asymptotic behavior of the solutions at large and small radial distance to integrate the disturbance equations. A spectral collocation and matrix eigenvalue method was used by Mayer and Powell (1992b) to study the linear stability of Batchelor's trailing line vortex. Their paper yielded the first global pictures of inviscid instabilities of the trailing vortex. Gartshore (1963) studied the quasi-cylindrical approximation of a trailing vortex using an integral approach. He found that a singularity may appear in the course of integration of the equations and the solution cannot be continued beyond the singular point. He suggested that these singularities may be mathematical indications of vortex breakdown. This work was continued by Mager (1972) who also used the integral approach to solve the quasi-cylindrical approximation equation. He made an attempt to connect the solutions he obtained with the concept of the breakdown as a supercritical-subcritical jump (suggested by Benjamin (1962)). Trigub et al. (1994) performed a consistent asymptotic study of steady axisymmetrical trailing vortices by using the quasi-cylindrical approximation. They presented numerical solutions for unbounded vortex breakdown parabolically expanding far downstream.

As discussed previously, pairs of trailing vortices do not decay by simple diffusion. Usually they undergo a symmetric and nearly sinusoidal instability, until eventually they join at intervals to form a train of vortex rings. Crow (1970) developed a theory that describes the early stage of this instability. The equation relating induced velocity to vortex displacement gives rise to an eigenvalue problem for the growth rate of sinusoidal

perturbations. The perturbation that grows most rapidly is a sinusoid of wavelength approximately 6 wing spans, which makes an angle of 48° to the wing planform.

Most practical wing tip vortex flows are turbulent. The mechanisms involved in turbulent flows may be entirely different from those of laminar flows. Hoffmann et al. (1963) predicted by theory, and confirmed by experiment, that the circulation in a turbulent vortex is proportional to the logarithm of the radius under certain conditions. They described a universal distribution of circulation in the inner region of the vortex, analogous to the turbulent boundary layer.

Govindaraju and Saffman (1971) showed that a turbulent vortex must develop an overshoot of circulation — the circulation rises above Γ_∞ for a finite r and then falls back to Γ_∞ as $r \to \infty$. They stressed this prediction is independent of any hypothesis about the Reynolds stress. Any numerical calculation involving any closure approximation should demonstrate an overshoot of circulation, provided the closure approximation is self-consistent with the conservation of angular momentum. The overshoot was found independently by Donaldson and Sullivan (1970), who studied the turbulent vortex numerically with a particular closure approximation. However, experiments do not indicate the presence of any significant overshoot in the circulation profile.

1.4 Scope of the Present Work

The decay of wing tip vortices due to viscosity is investigated analytically in this thesis. As previously mentioned, Batchelor's linear vortex model is the most advanced wing tip vortex model so far, and is valid far downstream of the wing where the axial velocity excess or deficit is much less than the freestream velocity. This downstream distance is estimated to be thousands of wing chords for a practical wing tip vortex (Moore and Saffman 1973). To understand the vortex structure fairly close to the vortex-generating wing, non-linear effects must be considered.

An analytical quasi-similarity method is developed for wing tip vortices. This new approach incorporates non-linear effects and velocity decay in a 3-D tip vortex. The central idea of the quasi-similarity method is that the solution consists of a polynomial in

which each term looks like a self-similar solution in complete function form — an amplitude function times the similarity function. The amplitude function is a function of downstream distance only, and the similarity function depends on a similarity variable. The similarity variable in turn is a non-dimensional combination of the downstream distance and radius coordinates. The limitation of this new method is that the axial velocity deficit or excess must not be significantly greater than the freestream velocity. This is much less restrictive than the limitation on Batchelor's linear theory.

The geometric details of the wing that generates a tip vortex has a substantial influence on the vortex flow. Changing simply the airfoil section shape (e.g. from an NACA 0020 to an NACA 16020), while keeping the wing planform constant, can dramatically change the tip vortex flow (Pauchet et al. 1993). Similarly, changing the wing planform has a marked influence on the tip vortex (Fruman et al. 1995). For example, elliptic wing planforms tend to behave quite differently from rectangular planforms (e.g. compare Figure 4 of Arndt et al. 1991 with Figure 1 of Green and Acosta 1991). Changing the wing tip shape and even roughness (Green et al. 1988, Stinebring et al. 1991) can also dramatically alter the tip vortex.

The search for a new wing geometry that avoids cavitation and/or reduces aerodynamic drag has been attractive to researchers. A novel ducted tip device, consisting of a small diameter flow-through duct, was attached to a rectangular untwisted wing and tested experimentally. Because the wing tip vortex generated by a ducted tip configuration would be expected to have a larger core than the tip vortex of a conventional tip, the pressure in the core would be higher than that of a conventional tip configuration. Therefore one might expect, and the expectation has been confirmed experimentally (Green et al. 1988), that the cavitation inception could be delayed by addition of a ducted tip device. A ducted tip is believed to reduce the induced drag of a wing as well, although it may cause a parasitic drag increase due to the extra wetted area at the tip.

Experiments on two kinds of ducted tip devices mounted on a NACA 66-209 rectangular planform wing have been done in a wind tunnel. The two tip devices studied were a ring-wing tip and a ducted bi-wing tip. Several configurations were considered for

each specific device. The lift and drag dependence on angle of attack, α, and pressure distribution on the wing surface were measured. All the results were compared with the baseline case of a rounded tip wing of identical span.

The cavitation characteristics of the ring-wing tip device were investigated in a water tunnel. With the hydrofoil and tip device in the tunnel, gradually U_∞ was increased and p_∞ decreased. At the moment of cavitation inception (as evidenced by the appearance of at least one macroscopic bubble per second in the trailing vortex core under stroboscopic illumination) U_∞ and p_∞ were measured. The cavitation performance is characterized by a parameter called the cavitation inception index, which is defined as $(p_\infty - p_v)/0.5\rho U_\infty^2$, where p_v is the water vapor pressure. The smaller the index, the better the cavitation performance.

In the next chapter, the quasi-similarity method for vortices in a freestream (e.g. wing tip vortices) is discussed. Chapter 3 contains quasi-similarity solutions for wing tip vortex structure. The cavitation and aerodynamic performance of the novel ducted tip device is documented in chapter 4. Chapter 5 presents a summary and the main conclusions of the present work.

Chapter 2 Quasi-Similarity Method for Vortices in a Freestream

In this chapter, a quasi-similarity method for 3-D viscous vortices in a freestream (e.g. wing tip vortices) is discussed. Polynomial solutions for the velocity components and pressure distribution in such a vortex are obtained. The analysis shows that the tangential velocity in a tip vortex decays much more slowly along the downstream direction than the axial velocity, an observation that is consistent with experimental findings.

2.1 Overview of Quasi-Similarity Method

The main idea of the quasi-similarity method is described briefly below. We start with the Navier-Stokes (N-S) equations in cylindrical coordinates. Some assumptions are made to simplify the N-S equations. The simplified governing equations, including the continuity equation, are a nonlinear system, which can be represented mathematically as

$$L_p\left[\upsilon_z(z,r),\upsilon_\theta(z,r),\upsilon_r(z,r),p(z,r)\right]=0 \tag{2.1.1}$$

L_p is an operator for partial differential equations, and (2.1.1) can be either the continuity or momentum equations.

The following polynomials are found to be the solution of (2.1.1), provided the summations are convergent.

$$\upsilon_z(z,r)=U_\infty\cdot\left[1+\sum_{i=1}^{\infty}\left(\frac{Cf_i}{z^i}\cdot F_i(\eta)\right)\right] \tag{2.1.2a}$$

$$\upsilon_\theta(z,r)=U_\infty\cdot\sum_{i=1}^{\infty}\left(\frac{Ct_i}{z^{i-0.5}}\cdot T_i(\eta)\right) \tag{2.1.2b}$$

$$\upsilon_r(z,r)=\frac{U_\infty\cdot\nu}{\Gamma}\cdot\sum_{i=1}^{\infty}\left(\frac{Cr_i}{z^{i+0.5}}\cdot R_i(\eta)\right) \tag{2.1.2c}$$

$$p(z,r)-p_\infty=\rho U_\infty^2\cdot\sum_{i=1}^{\infty}\left(\frac{Cg_i}{z^i}\cdot G_i(\eta)\right) \tag{2.1.2d}$$

Here $\eta=r\cdot\sqrt{\frac{U_\infty}{\nu\cdot z}}$ is a "similarity variable" and the coefficients denoted by capital C are constants (we will verify that only one constant is independent in the first order of the polynomial, and two constants are independent in each higher order of the polynomials). Γ is the circulation of the vortex, ν is the kinematic viscosity, U_∞ is the freestream

velocity, z is the axial distance along the vortex, r is the radial distance from the vortex centerline, and p_∞ is the pressure at infinity. Note that this is not a true similarity solution because the velocity components and pressure cannot be expressed solely in terms of η.

Substitution of (2.1.2) into (2.1.1) yields,

$$\sum_{i=1}^{\infty} \frac{C_i}{z^{i+1}} \cdot L_o\left[F_i(\eta), T_i(\eta), R_i(\eta), G_i(\eta)\right] = 0 \tag{2.1.3}$$

where L_o is the operator for an ordinary differential equation.

Because z is an arbitrary positive variable, for each of $i = 1,2,3,\cdots$, the following ordinary differential equation (ODE) must hold:

$$L_o\left[F_i(\eta), T_i(\eta), R_i(\eta), G_i(\eta)\right] = 0 \tag{2.1.4}$$

The ODE (2.1.4) can be solved with proper boundary conditions.

Only one constant is involved in the first order problem. It will be shown in the next chapter that this constant in the first order problem ($i = 1$) is related to the total drag of a wing. The constants in each of the higher order problems ($i \geq 2$) will be discussed later. It will be shown in Chapter 3 that the quasi-similarity solutions meet the following two requirements. One requirement is the conservation of the vortex circulation. The other requirement is the independence of wing total drag on the downstream distance.

With this overview of the quasi-similarity method completed, we proceed in the next sections to a detailed discussion thereof.

2.2 The Governing Equations

2.2.1 General governing equations

The incompressible Navier-Stokes equations in a cylindrical coordinate system are:

Continuity equation:

$$\frac{1}{r} \cdot \frac{\partial (r\upsilon_r)}{\partial r} + \frac{1}{r} \cdot \frac{\partial \upsilon_\theta}{\partial \theta} + \frac{\partial \upsilon_z}{\partial z} = 0 \tag{2.2.1}$$

Tangential momentum equation:

$$\frac{\partial \upsilon_\theta}{\partial t} + \vec{V} \bullet \nabla \upsilon_\theta + \frac{\upsilon_r \upsilon_\theta}{r} = -\frac{1}{\rho r}\frac{\partial p}{\partial \theta} + \nu \cdot \left(\nabla^2 \upsilon_\theta - \frac{\upsilon_\theta}{r^2} + \frac{2}{r^2} \cdot \frac{\partial \upsilon_r}{\partial \theta} \right) \qquad (2.2.2)$$

Radial momentum equation:

$$\frac{\partial \upsilon_r}{\partial t} + \vec{V} \bullet \nabla \upsilon_r - \frac{\upsilon_\theta^2}{r} = -\frac{1}{\rho} \cdot \frac{\partial p}{\partial r} + \nu \cdot \left(\nabla^2 \upsilon_r - \frac{\upsilon_r}{r^2} - \frac{2}{r^2} \cdot \frac{\partial \upsilon_\theta}{\partial \theta} \right) \qquad (2.2.3)$$

Axial momentum equation:

$$\frac{\partial \upsilon_z}{\partial t} + \vec{V} \bullet \nabla \upsilon_z = -\frac{1}{\rho} \cdot \frac{\partial p}{\partial z} + \nu \cdot \nabla^2 \upsilon_z \qquad (2.2.4)$$

where,

$$\vec{V} \bullet \nabla = \upsilon_r \frac{\partial}{\partial r} + \frac{\upsilon_\theta}{r}\frac{\partial}{\partial \theta} + \upsilon_z \frac{\partial}{\partial z}$$

$$\nabla^2 = \frac{1}{r} \cdot \frac{\partial}{\partial r}\left(r \frac{\partial}{\partial r} \right) + \frac{1}{r^2}\frac{\partial^2}{\partial \theta^2} + \frac{\partial^2}{\partial z^2}$$

In the above equations ρ is the density, υ_z the axial velocity, υ_θ the tangential velocity, υ_r the radial velocity, p the pressure, z the axial distance along the vortex, r the radial distance from the vortex centerline, and θ the azimuthal coordinate. We can simplify the above equations by making the following assumptions for a vortex in a freestream:

(1) The flow is incompressible, steady, and laminar

(2) The flow is axisymmetric

(3) $\upsilon_r << \upsilon_\theta$

(4) $\frac{\partial^2 \upsilon_\theta}{\partial z^2} << \frac{\partial^2 \upsilon_\theta}{\partial r^2}$; $\qquad \frac{\partial^2 \upsilon_z}{\partial z^2} << \frac{\partial^2 \upsilon_z}{\partial r^2}$

Then, the governing equations can be simplified and rewritten as:

$$\frac{1}{r} \cdot \frac{\partial (r \upsilon_r)}{\partial r} + \frac{\partial \upsilon_z}{\partial z} = 0 \qquad (2.2.5)$$

$$\upsilon_r \cdot \left(\frac{\partial \upsilon_\theta}{\partial r} + \frac{\upsilon_\theta}{r} \right) + \upsilon_z \frac{\partial \upsilon_\theta}{\partial z} = \nu \cdot \left(\frac{\partial^2 \upsilon_\theta}{\partial r^2} + \frac{1}{r}\frac{\partial \upsilon_\theta}{\partial r} - \frac{\upsilon_\theta}{r^2} \right) \qquad (2.2.6)$$

$$\frac{\upsilon_\theta^2}{r} = \frac{1}{\rho}\frac{\partial p}{\partial r} \tag{2.2.7}$$

$$\upsilon_r \frac{\partial \upsilon_z}{\partial r} + \upsilon_z \frac{\partial \upsilon_z}{\partial z} = -\frac{1}{\rho}\frac{\partial p}{\partial z} + \nu \cdot \left(\frac{\partial^2 \upsilon_z}{\partial r^2} + \frac{1}{r}\frac{\partial \upsilon_z}{\partial r} \right) \tag{2.2.8}$$

It is convenient to define a new variable $\psi = \upsilon_\theta / r$. With this definition of ψ, (2.2.6) and (2.2.7) become:

$$\upsilon_r \cdot \left(\frac{\partial \psi}{\partial r} + \frac{2\psi}{r} \right) + \upsilon_z \frac{\partial \psi}{\partial z} = \nu \left\{ \frac{\partial^2 \psi}{\partial r^2} + \frac{3}{r}\frac{\partial \psi}{\partial r} \right\} \tag{2.2.9}$$

$$\psi^2 \cdot r = \frac{1}{\rho}\frac{\partial p}{\partial r} \tag{2.2.10}$$

The function ψ has a definite physical meaning. For an axisymmetric vortex flow,

$$\psi(z,r)\Big|_{r=0} = \frac{\partial \upsilon_\theta}{\partial r}\Big|_{r=0} = \frac{\omega_z}{2}\Big|_{r=0}$$

where ω_z is the axial vorticity. $\psi(r=0)$ is thus half the value of the vorticity at $r=0$. Because the vorticity is non-zero in a real vortex at $r=0$, so too is ψ. (In fact, because the central core of a vortex is forced by the action of viscosity into solid body rotation, the vorticity on the axis of a vortex is 2Ω, where Ω is the angular frequency of the rotation.) This form of ψ is useful because it makes the tangential momentum and axial momentum equations take a similar form. It is therefore convenient in numerical calculations.

2.2.2 Non-dimensional governing equations

The dimensional information in the governing equations (2.2.5)-(2.2.8) can be expressed as

$$\frac{\upsilon_r}{r} \propto \frac{\upsilon_z}{z} \tag{2.2.11}$$

$$\frac{\upsilon_r \cdot \upsilon_\theta}{r} \propto \frac{\upsilon_z \cdot \upsilon_\theta}{z} \propto \nu \cdot \frac{\upsilon_\theta}{r^2} \tag{2.2.12}$$

$$\frac{\upsilon_\theta^2}{r} \propto \frac{1}{\rho} \cdot \frac{p}{r} \tag{2.2.13}$$

$$\frac{\upsilon_r \cdot \upsilon_z}{r} \propto \frac{\upsilon_z \cdot \upsilon_z}{z} \propto \frac{1}{\rho} \cdot \frac{p}{z} \propto \nu \frac{\upsilon_z}{r^2} \tag{2.2.14}$$

The non-repeated information is listed below

$$\frac{\upsilon_r}{r} \propto \frac{\upsilon_z}{z} \tag{2.2.15}$$

$$\upsilon_r \propto \frac{\nu}{r} \tag{2.2.16}$$

$$p \propto \rho \upsilon_\theta^2 \tag{2.2.17}$$

$$p \propto \rho \upsilon_z^2 \tag{2.2.18}$$

Now we assume that the circulation of the vortex, Γ, is a constant along the axis of the vortex. Thus

$$\upsilon_\theta \cdot r \propto \Gamma \tag{2.2.19}$$

Furthermore, it is reasonable to nondimensionize the axial velocity by the freestream velocity U_∞.

$$\upsilon_z \propto U_\infty \tag{2.2.20}$$

Therefore, the variables describing a viscous vortex in a freestream can be non-dimensionized using the following characteristic physical parameters — the freestream velocity U_∞, the circulation of the vortex Γ, the fluid density ρ, and the kinematic viscosity ν:

$$z = \frac{\Gamma^2}{U_\infty \cdot \nu} \cdot \tilde{z} \tag{2.2.21}$$

$$r = \frac{\Gamma}{U_\infty} \cdot \tilde{r} \tag{2.2.22}$$

$$\upsilon_z = U_\infty \cdot \tilde{\upsilon}_z \tag{2.2.23}$$

$$\upsilon_r = \frac{U_\infty \cdot \nu}{\Gamma} \cdot \tilde{\upsilon}_r \tag{2.2.24}$$

$$p = \rho U_\infty^2 \cdot \tilde{p} \tag{2.2.25}$$

$$\psi = \frac{U_\infty^2}{\Gamma} \cdot \tilde{\psi} \qquad \text{or} \qquad \upsilon_\theta = U_\infty \cdot \tilde{\upsilon}_\theta \tag{2.2.26}$$

where the variables with a symbol "~" are non-dimensional parameters. The dimensionless governing equations are therefore:

$$\frac{1}{\tilde{r}}\cdot\frac{\partial(\tilde{r}\tilde{\upsilon}_r)}{\partial\tilde{r}}+\frac{\partial\tilde{\upsilon}_z}{\partial\tilde{z}}=0 \tag{2.2.27}$$

$$\tilde{\upsilon}_r\cdot\left(\frac{\partial\tilde{\psi}}{\partial\tilde{r}}+\frac{2\tilde{\psi}}{\tilde{r}}\right)+\tilde{\upsilon}_z\frac{\partial\tilde{\psi}}{\partial\tilde{z}}=\frac{\partial^2\tilde{\psi}}{\partial\tilde{r}^2}+\frac{3}{\tilde{r}}\frac{\partial\tilde{\psi}}{\partial\tilde{r}} \tag{2.2.28}$$

$$\tilde{\psi}^2\cdot\tilde{r}=\frac{\partial\tilde{p}}{\partial\tilde{r}} \tag{2.2.29}$$

$$\tilde{\upsilon}_r\frac{\partial\tilde{\upsilon}_z}{\partial\tilde{r}}+\tilde{\upsilon}_z\frac{\partial\tilde{\upsilon}_z}{\partial\tilde{z}}=-\frac{\partial\tilde{p}}{\partial\tilde{z}}+\frac{\partial^2\tilde{\upsilon}_z}{\partial\tilde{r}^2}+\frac{1}{\tilde{r}}\frac{\partial\tilde{\upsilon}_z}{\partial\tilde{r}} \tag{2.2.30}$$

The boundary conditions for the above equations will be discussed later.

2.2.3 Structure of the solutions

In the derivation that follows, we will assume that a "quasi-similarity" solution describes the vortex in a freestream. The phrase "quasi-similarity" is here used to describe a polynomial solution in which each term of the polynomial is a power product of some function of the axial distance (the amplitude function), and a different function of the similarity variable (the similarity function). If a quasi-similarity solution exists for the flow in such a vortex in a freestream, one might expect the similarity variable to take much the same form as that of a free jet or boundary layer, i.e.:

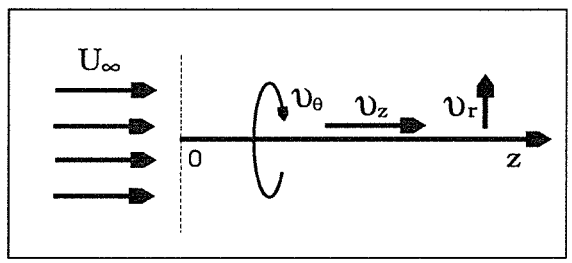

Figure 2.1 Vortex in a freestream

$$\eta=\frac{\tilde{r}}{\sqrt{\tilde{z}}}=r\cdot\sqrt{\frac{U_\infty}{\nu\cdot z}} \tag{2.2.31}$$

With this choice of similarity variable, the quasi-similarity solution for the three velocity components and pressure is then posited to take the form:

$$\tilde{\upsilon}_z(\tilde{z},\tilde{r})=1+\sum_{i=1}^{\infty}U_i(\tilde{z})\cdot F_i(\eta)=1+\sum_{i=1}^{\infty}\tilde{\upsilon}_{z(i)} \tag{2.2.32}$$

$$\tilde{\upsilon}_r(\tilde{z},\tilde{r})=\sum_{i=1}^{\infty}V_i(\tilde{z})\cdot R_i(\eta)=\sum_{i=1}^{\infty}\tilde{\upsilon}_{r(i)} \tag{2.2.33}$$

$$\tilde{\psi}(\tilde{z},\tilde{r}) = \sum_{i=1}^{\infty} \Psi_i(\tilde{z}) \cdot H_i(\eta) = \sum_{i=1}^{\infty} \tilde{\psi}_{(i)} \tag{2.2.34}$$

$$\tilde{p}(\tilde{z},\tilde{r}) - \tilde{p}_\infty = \sum_{i=1}^{\infty} P_i(\tilde{z}) \cdot G_i(\eta) = \sum_{i=1}^{\infty} \tilde{p}_{(i)} \tag{2.2.35}$$

where the amplitude functions (those to be functions of $\tilde{z}$ only) will be verified in section 2.5 to take the form:

$$U_i(\tilde{z}) = \frac{Cf_i}{\tilde{z}^i}, \quad V_i(\tilde{z}) = \frac{Cr_i}{\sqrt{\tilde{z}} \cdot \tilde{z}^i}, \quad \Psi_i(\tilde{z}) = \frac{Ch_i}{\tilde{z}^i}, \quad P_i(\tilde{z}) = \frac{Cg_i}{\tilde{z}^i} \tag{2.2.36}$$

The coefficients denoted by capital C are constants. Substitution of (2.2.32) and (2.2.33) into (2.2.27), yields

$$\sum_{i=1}^{\infty} \frac{1}{\tilde{z}^{i+1}} \cdot L_o\left[F_i(\eta), R_i(\eta)\right] = 0$$

where L_o is an ODE operator. $L_o\left[F_i(\eta), R_i(\eta)\right] = 0$ must hold because $\tilde{z}$ is arbitrary. Similarly, substituting (2.2.33)-(2.2.36) into (2.2.28)-(2.2.30) results in three other ordinary differential equations for each order (i.e. $\frac{1}{\tilde{z}^i}$, $i = 1,2,3,\cdots$) of the polynomial solution.

2.2.4 Governing equations of the first order

The first order partial differential equations consist of all the terms inversely proportional to the distance $\tilde{z}$ that occur when (2.2.32)-(2.2.36) are substituted into (2.2.27)-(2.2.30):

$$\frac{\partial(\tilde{\upsilon}_r)_1}{\partial\tilde{r}} + \frac{(\tilde{\upsilon}_r)_1}{\tilde{r}} + \frac{\partial(\tilde{\upsilon}_z)_1}{\partial\tilde{z}} = 0 \tag{2.2.37a}$$

$$\frac{\partial\tilde{\psi}_1}{\partial\tilde{z}} = \frac{\partial^2\tilde{\psi}_1}{\partial\tilde{r}^2} + \frac{3}{\tilde{r}} \cdot \frac{\partial\tilde{\psi}_1}{\partial\tilde{r}} \tag{2.2.37b}$$

$$\tilde{\psi}_1^2 \cdot \tilde{r} = \frac{\partial\tilde{p}_1}{\partial\tilde{r}} \tag{2.2.37c}$$

$$\frac{\partial(\tilde{\upsilon}_z)_1}{\partial\tilde{z}} = -\frac{\partial\tilde{p}_1}{\partial\tilde{z}} + \frac{\partial^2(\tilde{\upsilon}_z)_1}{\partial\tilde{r}^2} + \frac{1}{\tilde{r}} \cdot \frac{\partial(\tilde{\upsilon}_z)_1}{\partial\tilde{r}} \tag{2.2.37d}$$

Note that $\tilde{r}^2/\tilde{z}$ can be replaced by the similarity variable η^2 in the above equations.

2.2.5 Governing equations of the second order

Like the first order differential equations, the second order partial differential equations consist of all the terms inversely proportional to the square of the distance $\tilde{z}$:

$$\frac{\partial(\tilde{\upsilon}_r)_2}{\partial\tilde{r}}+\frac{(\tilde{\upsilon}_r)_2}{\tilde{r}}+\frac{\partial(\tilde{\upsilon}_z)_2}{\partial\tilde{z}}=0 \tag{2.2.38a}$$

$$\frac{\partial\tilde{\psi}_2}{\partial\tilde{z}}=\frac{\partial^2\tilde{\psi}_2}{\partial\tilde{r}^2}+\frac{3}{\tilde{r}}\cdot\frac{\partial\tilde{\psi}_2}{\partial\tilde{r}}-\left\{(\tilde{\upsilon}_r)_1\cdot\left(\frac{\partial\tilde{\psi}_1}{\partial\tilde{r}}+\frac{2\tilde{\psi}_1}{\tilde{r}}\right)+(\tilde{\upsilon}_z)_1\cdot\frac{\partial\tilde{\psi}_1}{\partial\tilde{z}}\right\} \tag{2.2.38b}$$

$$2\tilde{\psi}_1\tilde{\psi}_2\tilde{r}=\frac{\partial\tilde{p}_2}{\partial\tilde{r}} \tag{2.2.38c}$$

$$\frac{\partial(\tilde{\upsilon}_z)_2}{\partial\tilde{z}}=-\frac{\partial\tilde{p}_2}{\partial\tilde{z}}+\frac{\partial^2(\tilde{\upsilon}_z)_2}{\partial\tilde{r}^2}+\frac{1}{\tilde{r}}\cdot\frac{\partial(\tilde{\upsilon}_z)_2}{\partial\tilde{r}}-\left\{(\tilde{\upsilon}_r)_1\cdot\frac{\partial(\tilde{\upsilon}_z)_1}{\partial\tilde{r}}+(\tilde{\upsilon}_z)_1\cdot\frac{\partial(\tilde{\upsilon}_z)_1}{\partial\tilde{z}}\right\} \tag{2.2.38d}$$

Similarly, $\tilde{r}^2/\tilde{z}$ can be replaced by the similarity variable η^2 in the above equations.

2.2.6 Governing equations of the arbitrary *i*-th order

Substitution of (2.2.32)-(2.2.36) into (2.2.27)-(2.2.30), and retention of all the terms proportional to $\frac{1}{\tilde{z}^i}$, yields the governing equations for the *i*-th order problem:

$$\frac{\partial(\tilde{\upsilon}_r)_i}{\partial\tilde{r}}+\frac{(\tilde{\upsilon}_r)_i}{\tilde{r}}+\frac{\partial(\tilde{\upsilon}_z)_i}{\partial\tilde{z}}=0 \tag{2.2.39a}$$

$$\begin{aligned}\frac{\partial^2\tilde{\psi}_i}{\partial\tilde{r}^2}+\frac{3}{\tilde{r}}\cdot\frac{\partial\tilde{\psi}_i}{\partial\tilde{r}}-\frac{\partial\tilde{\psi}_i}{\partial\tilde{z}}&=\sum_{j=1}^{i-1}\left\{(\tilde{\upsilon}_z)_j\cdot\frac{\partial\tilde{\psi}_{i-j}}{\partial\tilde{z}}\right\}\\&+\sum_{j=1}^{i-1}\left\{(\tilde{\upsilon}_r)_j\cdot\left[\frac{\partial\tilde{\psi}_{i-j}}{\partial\tilde{r}}+\frac{2\tilde{\psi}_{i-j}}{\tilde{r}}\right]\right\}\end{aligned} \tag{2.2.39b}$$

$$\frac{\partial\tilde{p}_i}{\partial\tilde{r}}=\tilde{r}\cdot\sum_{j=1}^{i}\left(\tilde{\psi}_j\cdot\tilde{\psi}_{i-j+1}\right) \tag{2.2.39c}$$

$$\frac{\partial^2(\tilde{\upsilon}_z)_i}{\partial\tilde{r}^2}+\frac{1}{\tilde{r}}\cdot\frac{\partial(\tilde{\upsilon}_z)_i}{\partial\tilde{r}}-\frac{\partial(\tilde{\upsilon}_z)_i}{\partial\tilde{z}}=\frac{\partial\tilde{p}_i}{\partial\tilde{z}}+\sum_{j=1}^{i-1}\left\{(\tilde{\upsilon}_z)_j\cdot\frac{\partial(\tilde{\upsilon}_z)_{i-j}}{\partial\tilde{z}}\right\}$$
$$+\sum_{j=1}^{i-1}\left\{(\tilde{\upsilon}_r)_j\cdot\frac{\partial(\tilde{\upsilon}_z)_{i-j}}{\partial\tilde{r}}\right\} \tag{2.2.39d}$$

In like fashion to the first order problem, the combination $\tilde{r}^2/\tilde{z}$ can be replaced by the similarity variable η^2 in the above equations.

2.3 The First Order Problem

2.3.1 Derivation of the Governing Quasi-Similarity Equations

To simplify subsequent mathematical manipulations, we state below some simple identities. First, we recognize that the following fundamental relations hold for the similarity variable defined by $\eta=\tilde{r}/\sqrt{\tilde{z}}$:

$$\frac{\partial\eta}{\partial\tilde{r}}=\frac{1}{\sqrt{\tilde{z}}}=\frac{\eta}{\tilde{r}} \tag{2.3.1}$$

$$\frac{\partial\eta}{\partial\tilde{z}}=-\frac{\eta}{2\tilde{z}} \tag{2.3.2}$$

Next, considering an arbitrary function $\varphi(\tilde{z},\tilde{r})=f(\tilde{z})\cdot g(\eta)$, the following differential relations are found to be valid:

$$\frac{\partial\varphi}{\partial\tilde{z}}=\frac{f(\tilde{z})}{2\tilde{z}}\cdot\left\{\frac{2\tilde{z}\cdot f'(\tilde{z})}{f(z)}\cdot g(\eta)-\eta\cdot g'(\eta)\right\} \tag{2.3.3}$$

$$\frac{\partial\varphi}{\partial\tilde{r}}=\frac{\eta}{\tilde{r}}f(\tilde{z})\cdot g'(\eta) \tag{2.3.4}$$

$$\frac{\partial^2\varphi}{\partial\tilde{r}^2}=\frac{\eta^2}{\tilde{r}^2}f(\tilde{z})\cdot g''(\eta) \tag{2.3.5}$$

Making use of the above relations, the continuity equation (2.2.37a) for the first order problem can be rewritten as

$$\frac{2\sqrt{\tilde{z}}\cdot V_1(\tilde{z})}{U_1(\tilde{z})}\left\{R_1'(\eta)+\frac{R_1(\eta)}{\eta}\right\}+\frac{2\tilde{z}\cdot U_1'(\tilde{z})}{U_1(\tilde{z})}F_1(\eta)-\eta F_1'(\eta)=0 \tag{2.3.6}$$

A "quasi-similarity" solution can exist for the continuity equation (Equation 2.3.6) if the equation can be made to be solely a function of the independent variable, η. Equation 2.3.6 is a function of η alone provided:

$$V_1(\tilde{z}) = K \cdot \frac{U_1(\tilde{z})}{\sqrt{\tilde{z}}} \tag{2.3.7}$$

$$U_1(\tilde{z}) = C_1 \cdot \tilde{z}^{a_1} \tag{2.3.8}$$

where C_1, a_1 and K are constants. The constant K does not affect the computed velocities, and is set to 1 for simplicity. Using equations (2.3.7) and (2.3.8), the continuity equation can be rewritten as

$$2\eta R_1'(\eta) + 2R_1(\eta) = \eta^2 \cdot F_1'(\eta) - 2a_1 \cdot \eta \cdot F_1(\eta) \tag{2.3.9}$$

The tangential momentum equation (2.2.37b) can similarly be simplified to read

$$\frac{2\tilde{z} \cdot \Psi_1'(\tilde{z})}{\Psi_1(\tilde{z})} H_1(\eta) - \eta H_1'(\eta) = 2H_1''(\eta) + \frac{6}{\eta} H_1'(\eta) \tag{2.3.10}$$

A quasi-similarity solution exists for the tangential momentum equation if and only if

$$\Psi_1(\tilde{z}) = C_2 \cdot \tilde{z}^{b_1} \tag{2.3.11}$$

where C_2 and b_1 are constants. The simplified ODE of the tangential momentum equation is thus,

$$2\eta \cdot H_1''(\eta) + \left[\eta^2 + 6\right] \cdot H_1'(\eta) - 2b_1 \cdot \eta \cdot H_1(\eta) = 0 \tag{2.3.12}$$

In similar fashion to the derivation of (2.3.6) above, the ODE form of the radial momentum equation (2.2.37c) can be shown to be

$$G_1'(\eta) = \frac{\tilde{z} \cdot \Psi_1^2(\tilde{z})}{P_1(\tilde{z})} \cdot \eta \cdot H_1^2(\eta) \tag{2.3.13}$$

for which a quasi-similarity solution exists only if

$$P_1(\tilde{z}) = \tilde{z} \cdot \Psi_1^2(\tilde{z}) \tag{2.3.14}$$

Finally, the axial momentum equation (2.2.27d) can be rewritten as

$$\begin{aligned} &2\eta \cdot F_1''(\eta) + \left[\eta^2 + 2\right] \cdot F_1'(\eta) - 2a_1 \cdot \eta F_1(\eta) \\ &\quad = \frac{P_1(\tilde{z})}{U_1(\tilde{z})} \cdot \left[2(1+2b_1)\eta \cdot G_1(\eta) - \eta^2 \cdot G_1'(\eta)\right] \end{aligned} \tag{2.3.15}$$

The following relation must hold for a quasi-similarity solution of (2.3.15) to exist,

$$\frac{P_1(\tilde{z})}{U_1(\tilde{z})} = \beta \tag{2.3.16}$$

where β is a constant.

The ODE form of the axial momentum equation is then,

$$\begin{aligned} &2\eta \cdot F_1''(\eta) + \left[\eta^2 + 2\right] \cdot F_1'(\eta) - 2a_1 \cdot \eta F_1(\eta) \\ &\quad = \beta \cdot \left[2(1+2b_1)\eta \cdot G_1(\eta) - \eta^2 \cdot G_1'(\eta)\right] \end{aligned} \tag{2.3.17}$$

Combining (2.3.8) with (2.3.11), (2.3.14) and (2.3.16), one obtains

$$\beta = \frac{P_1(\tilde{z})}{U_1(\tilde{z})} = \frac{\tilde{z} \cdot \Psi_1^2(\tilde{z})}{U_1(\tilde{z})} = \frac{C_2^2}{C_1} \cdot \tilde{z}^{2b_1+1-a_1} \tag{2.3.18}$$

Because β is a constant, we have

$$a_1 = 2b_1 + 1 \qquad \text{and} \qquad \beta = \frac{C_2^2}{C_1} \tag{2.3.19}$$

The constants b_1 and C_2 can also be determined by applying the condition that the circulation around the vortex far from the vortex axis is independent of downstream distance (a consequence of Kelvin's Theorem):

$$\Gamma = \left(2\pi r \cdot \upsilon_\theta\right)_{r\to\infty} = \text{constant} \tag{2.3.20}$$

The dimensionless form of (2.3.20) is $(\tilde{r} \cdot \tilde{\upsilon}_\theta)_{\tilde{r}\to\infty} = \frac{1}{2\pi}$, thus

$$\left(\tilde{r} \cdot \tilde{\upsilon}_\theta\right)_{\tilde{r}\to\infty} = \left(\tilde{r}^2 \cdot \tilde{\psi}\right)_{\tilde{r}\to\infty} = \left(\tilde{r}^2 \cdot \sum_{i=1}^{\infty} \tilde{\psi}_i\right)_{\tilde{r}\to\infty} = \frac{1}{2\pi} \tag{2.3.21}$$

It can be verified that for the second or higher order, $\left(\tilde{r}^2 \cdot \tilde{\psi}_i\right)_{\tilde{r}\to\infty} \propto \left[\eta^2 \cdot H_i(\eta)\right]_{\eta\to\infty} \equiv 0$ (refer to section 4.1 in Chapter 3). Thus, (2.3.21) can be rewritten as

$$C_2 \cdot \tilde{z}^{b_1+1} \cdot \left[\eta^2 \cdot H_1(\eta)\right]_{\eta\to\infty} = \frac{1}{2\pi} \tag{2.3.22}$$

and therefore, $b_1 = -1$ and $C_2 = \dfrac{1}{2\pi\left[\eta^2 \cdot H_1(\eta)\right]_{\eta\to\infty}}$ (2.3.23a)

thus $a_1 = 2b_1 + 1 = -1$, $C_1 = \dfrac{C_2^2}{\beta} = \dfrac{1}{4\pi^2\beta\left[\eta^2 \cdot H_1(\eta)\right]_{\eta\to\infty}^2}$ (2.3.23b)

To summarize, the following amplitude functions have been obtained for the first order problem:

$$U_1(\tilde{z}) = \frac{1}{4\pi^2\beta\left[\eta^2 \cdot H_1(\eta)\right]^2_{\eta\to\infty} \cdot \tilde{z}} \tag{2.3.24a}$$

$$V_1(\tilde{z}) = \frac{U_1(\tilde{z})}{\sqrt{\tilde{z}}} \tag{2.3.24b}$$

$$P_1(\tilde{z}) = \beta \cdot U_1(\tilde{z}) \tag{2.3.24c}$$

$$\Psi_1(\tilde{z}) = \frac{1}{2\pi\left[\eta^2 \cdot H_1(\eta)\right]_{\eta\to\infty} \cdot \tilde{z}} = 2\pi\beta\left[\eta^2 H_1(\eta)\right]_{\eta\to\infty} \cdot U_1(\tilde{z}) \tag{2.3.24d}$$

where β is a constant.

2.3.2 Boundary Conditions on the Quasi-Similarity Equations

With all the unknown constants (except β) evaluated, we may rewrite the governing ODEs that determine the first order similarity functions:

$$2\eta R_1'(\eta) + 2R_1(\eta) = \eta^2 \cdot F_1'(\eta) + 2\eta \cdot F_1(\eta) \tag{2.3.25a}$$

$$2\eta \cdot H_1''(\eta) + (\eta^2 + 6) \cdot H_1'(\eta) + 2\eta \cdot H_1(\eta) = 0 \tag{2.3.25b}$$

$$G_1'(\eta) = \eta \cdot H_1^2(\eta) \tag{2.3.25c}$$

$$2\eta \cdot F_1''(\eta) + (\eta^2 + 2) \cdot F_1'(\eta) + 2\eta \cdot F_1(\eta) = -\beta \cdot \left[2\eta \cdot G_1(\eta) + \eta^3 \cdot H_1^2(\eta)\right] \tag{2.3.25d}$$

Equations 2.3.25a-d are four coupled ordinary differential equations in the four unknown functions R_1, F_1 ,G_1 , and H_1. The equations are first order in R_1 and G_1, and second order in F_1 and H_1, and consequently require one boundary condition on R_1 and G_1, and two each on the F_1 and H_1. The boundary conditions that apply to these equations are:

$$R_1(0) = 0 \tag{2.3.26a}$$

$$H_1(0) = 1, \qquad H_1'(0) = 0 \tag{2.3.26b}$$

$$F_1(0) = 1, \qquad F_1'(0) = 0 \tag{2.3.26c}$$

$$G_1(\infty) = 0 \tag{2.3.26d}$$

(2.3.26a) must hold to ensure the flow is symmetrical about the vortex centerline. $H_1(0)$ is set equal to one for simplicity (2.3.26b); a constant different from one will not affect the calculated tangential velocity. The second equation of (2.3.26b) ensures the second

derivative at the origin has a finite value for symmetrical flow ($\left.\frac{\partial\psi}{\partial r}\right|_{r=0} = 0$). The first equation of (2.3.26c) holds because β in the amplitude function $U_1(z)$ is a free constant. A non-unity value of the constant $F_1(0)$ will not affect the final results. The second condition of (2.3.26c) ensures the second derivative exists at the origin for a symmetrical flow ($\left.\frac{\partial\upsilon_z}{\partial r}\right|_{r=0} = 0$). (2.3.26d) arises from the freestream velocity condition.

The ODEs given by Equations (2.3.25a-d) form a decoupled system. We can solve (2.3.25b) for $H_1(\eta)$ first, then (2.3.25c) for $G_1(\eta)$, then (2.3.25d) for $F_1(\eta)$, and finally (2.3.25a) for $R_1(\eta)$, as will be discussed in Chapter 3.

The limit on $\eta^2 \cdot H_1(\eta)$ in the amplitude functions (2.3.24a-d) can be evaluated. The non-singular solution of (2.3.25b) with the boundary conditions (2.3.26b) is

$$H_1(\eta) = \frac{4}{\eta^2}\left(1 - e^{-\frac{\eta^2}{4}}\right) \tag{2.3.27}$$

Thus,

$$\left[\eta^2 \cdot H_1(\eta)\right]_{\eta\to\infty} = 4 \tag{2.3.28}$$

The amplitude functions (2.3.24a-d) for the first order problem can therefore be simplified and rewritten as:

$$U_1(\tilde{z}) = \frac{1}{64\pi^2\beta \cdot \tilde{z}} \tag{2.3.32a}$$

$$V_1(\tilde{z}) = \frac{U_1(\tilde{z})}{\sqrt{\tilde{z}}} \tag{2.3.32b}$$

$$P_1(\tilde{z}) = \frac{1}{64\pi^2 \cdot \tilde{z}} = \beta \cdot U_1(\tilde{z}) \tag{2.3.32c}$$

$$\Psi_1(\tilde{z}) = \frac{1}{8\pi \cdot \tilde{z}} = 8\pi\beta \cdot U_1(\tilde{z}) \tag{2.3.32d}$$

where β is a constant. There is only one constant, β, which is undetermined in the first order problem. We will show in the next chapter that this constant is closely related to the total drag of the wing that generates the wing tip vortices.

2.4 The Second Order Problem

The ODE form of the second order continuity equation (2.2.38a) is similar to the form of the first order continuity equation:

$$2\eta R_2'(\eta)+2R_2(\eta)=\eta^2\cdot F_2'(\eta)-2a_2\cdot\eta F_2(\eta) \tag{2.4.1}$$

where $a_2=\dfrac{\tilde{z}\cdot U_2'(\tilde{z})}{U_2(\tilde{z})}$ (2.4.2)

A quasi-similarity solution exists for (2.4.1) if and only if

$$V_2(\tilde{z})=\frac{U_2(\tilde{z})}{\sqrt{\tilde{z}}} \tag{2.4.3}$$

The tangential momentum equation for the second order problem (2.2.38b) can be simplified to:

$$\begin{aligned}&\frac{2\tilde{z}\Psi_2'(\tilde{z})}{\Psi_2(\tilde{z})}H_2(\eta)-\eta H_2'(\eta)=2H_2''(\eta)+\frac{6}{\eta}H_2'(\eta)\\&-\frac{U_1(\tilde{z})\cdot\Psi_1(\tilde{z})}{\Psi_2(\tilde{z})}\cdot\frac{1}{\eta}\cdot\left\{\left[2\eta H_1'(\eta)+4H_1(\eta)\right]R_1(\eta)-\left[2\eta H_1(\eta)+\eta^2H_1'(\eta)\right]F_1(\eta)\right\}\end{aligned} \tag{2.4.4}$$

The following relation has to hold for a quasi-similarity solution of (2.4.4) to exist.

$$\frac{U_1(\tilde{z})\cdot\Psi_1(\tilde{z})}{\Psi_2(\tilde{z})}=\alpha_2 \tag{2.4.5}$$

where α_2 is a constant.

thus $\dfrac{\tilde{z}\cdot\Psi_2'(\tilde{z})}{\Psi_2(\tilde{z})}=\dfrac{\tilde{z}\cdot U_1'(\tilde{z})}{U_1(\tilde{z})}+\dfrac{\tilde{z}\cdot\Psi_1'(\tilde{z})}{\Psi_1(\tilde{z})}=a_1+b_1=-2$ (2.4.6)

The tangential momentum equation thus can be rewritten as

$$\begin{aligned}&2\eta\cdot H_2''(\eta)+(\eta^2+6)\cdot H_2'(\eta)+4\eta\cdot H_2(\eta)\\&=\alpha_2\cdot\left\{\left[2\eta H_1'(\eta)+4H_1(\eta)\right]\cdot R_1(\eta)-\left[\eta^2\cdot H_1'(\eta)+2\eta H_1(\eta)\right]\cdot F_1(\eta)\right\}\end{aligned} \tag{2.4.7}$$

The radial momentum equation (2.2.38c) can be rewritten as the following ODE:

$$G_2'(\eta)=2\eta H_1(\eta)\cdot H_2(\eta) \tag{2.4.8}$$

Quasi-similarity solutions exist for (2.4.8) as long as

$$P_2(\tilde{z})=\tilde{z}\cdot\Psi_1(\tilde{z})\cdot\Psi_2(\tilde{z})=\frac{1}{\alpha_2}\cdot P_1(\tilde{z})\cdot U_1(\tilde{z}) \tag{2.4.9}$$

Finally, the axial momentum equation (2.2.38d) can be rewritten as

$$
\begin{aligned}
&2\eta F_2''(\eta)+(\eta^2+2)F_2'(\eta)-2a_2\eta F_2(\eta)= \\
&-\frac{P_2(\tilde{z})}{U_2(\tilde{z})}\left[4\eta G_2(\eta)+2\eta^3 H_1(\eta)\cdot H_2(\eta)\right] \\
&+\frac{U_1^2(\tilde{z})}{U_2(\tilde{z})}\left\{2\eta R_1(\eta)F_1'(\eta)-\eta F_1(\eta)\cdot\left[2F_1(\eta)+\eta F_1'(\eta)\right]\right\}
\end{aligned}
\tag{2.4.10}
$$

A quasi-similarity solution exists only if the following relations hold

$$\frac{P_2(\tilde{z})}{U_2(\tilde{z})}=\beta_2 \tag{2.4.11}$$

$$\frac{U_1^2(\tilde{z})}{U_2(\tilde{z})}=c_2 \tag{2.4.12}$$

where β_2 and c_2 are constants.

thus $$a_2=\frac{\tilde{z}\cdot U_2'(\tilde{z})}{U_2(\tilde{z})}=\frac{2\tilde{z}\cdot U_1'(\tilde{z})}{U_1(\tilde{z})}=-2 \tag{2.4.13}$$

By applying the relations (2.4.9), (2.4.11), (2.4.12) and (2.3.16), one finds

$$\frac{P_2(\tilde{z})}{U_2(\tilde{z})}=\frac{c_2\cdot P_1(\tilde{z})\cdot U_1(\tilde{z})}{\alpha_2\cdot U_1^2(\tilde{z})}=\frac{c_2\cdot\beta}{\alpha_2} \tag{2.4.14}$$

Comparing (2.4.11) with (2.4.14), one obtains

$$\alpha_2=\frac{\beta\cdot c_2}{\beta_2} \tag{2.4.15}$$

To summarize, the following relations must be satisfied in order for quasi-similarity solutions to exist:

$$U_2(\tilde{z})=\frac{1}{c_2}\cdot U_1^2(\tilde{z})=\left(\frac{1}{64\pi^2\tilde{z}}\right)^2\cdot\frac{1}{\beta^2\cdot c_2} \tag{2.4.16a}$$

$$V_2(\tilde{z})=\frac{1}{c_2}\cdot V_1(\tilde{z})\cdot U_1(\tilde{z})=\frac{1}{\sqrt{\tilde{z}}}\cdot\left(\frac{1}{64\pi^2\tilde{z}}\right)^2\cdot\frac{1}{\beta^2\cdot c_2} \tag{2.4.16b}$$

$$P_2(\tilde{z})=\frac{\beta_2}{\beta\cdot c_2}\cdot P_1(\tilde{z})\cdot U_1(\tilde{z})=\left(\frac{1}{64\pi^2\tilde{z}}\right)^2\cdot\frac{\beta_2}{\beta^2\cdot c_2} \tag{2.4.16c}$$

$$\Psi_2(\tilde{z})=\frac{\beta_2}{\beta\cdot c_2}\cdot\Psi_1(\tilde{z})\cdot U_1(\tilde{z})=\left(\frac{1}{64\pi^2\tilde{z}}\right)^2\cdot\frac{8\pi\beta_2}{\beta^2\cdot c_2} \tag{2.4.16d}$$

Notice that there are only two independent constants in the second order problem (except β). It is permissible to select $c_2=1$ and $\alpha_2=1$, and let $H_2(0)=Ch_2$ and $F_2(0)=Cf_2$,

without loss of generality. From equation (2.4.15), $\beta_2 = \beta$. Therefore, the amplitude functions can be expressed as

$$U_2(\tilde{z}) = U_1^2(\tilde{z}) \tag{2.4.17a}$$

$$V_2(\tilde{z}) = \frac{1}{\sqrt{\tilde{z}}} \cdot U_1^2(\tilde{z}) \tag{2.4.17b}$$

$$P_2(\tilde{z}) = \beta \cdot U_1^2(\tilde{z}) \tag{2.4.17c}$$

$$\Psi_2(\tilde{z}) = 8\pi\beta \cdot U_1^2(\tilde{z}) \tag{2.4.17d}$$

The second order quasi-similarity solutions of the vortex flow in a freestream can be obtained by solving the following ODEs with their boundary conditions:

$$2\eta R_2'(\eta) + 2R_2(\eta) = \eta^2 \cdot F_2'(\eta) + 4\eta \cdot F_2(\eta) \tag{2.4.18a}$$

$$\begin{aligned} &2\eta \cdot H_2''(\eta) + (\eta^2 + 6) \cdot H_2'(\eta) + 4\eta \cdot H_2(\eta) \\ &\quad = \left[2\eta H_1'(\eta) + 4H_1(\eta)\right] \cdot R_1(\eta) - \left[\eta^2 \cdot H_1'(\eta) + 2\eta H_1(\eta)\right] \cdot F_1(\eta) \end{aligned} \tag{2.4.18b}$$

$$G_2'(\eta) = 2\eta \cdot H_1(\eta) \cdot H_2(\eta) \tag{2.4.18c}$$

$$\begin{aligned} &2\eta \cdot F_2''(\eta) + (\eta^2 + 2) \cdot F_2'(\eta) + 4\eta \cdot F_2(\eta) \\ &\quad = -\beta \cdot \left[4\eta \cdot G_2(\eta) + 2\eta^3 \cdot H_1(\eta) \cdot H_2(\eta)\right] \\ &\quad + 2\eta R_1(\eta) \cdot F_1'(\eta) - \eta F_1(\eta) \cdot \left[2F_1(\eta) + \eta F_1'(\eta)\right] \end{aligned} \tag{2.4.18d}$$

where β is the constant that appeared in the first order problem. The boundary conditions of this second order problem are

$$R_2(0) = 0 \tag{2.4.19a}$$

$$H_2(0) = Ch_1 = \text{constant}, \qquad H_2'(0) = 0 \tag{2.4.19b}$$

$$F_2(0) = Cf_2 = \text{constant}, \qquad F_2'(0) = 0 \tag{2.4.19c}$$

$$G_2(\infty) = 0 \tag{2.4.19d}$$

Analogously to the first order boundary conditions, (2.4.19a) must hold to ensure the flow is symmetrical about the vortex centerline. The constant in the first equation of (2.4.19b) is related to the second order vorticity at the origin $r = 0$. The second equation of (2.4.19b) ensures the second derivative at the origin has a finite value for symmetrical flow ($\left.\frac{\partial \psi}{\partial r}\right|_{r=0} = 0$). The constant in the first equation of (2.4.19c) represents the amplitude of the second order axial velocity on the vortex centerline. The second condition of

(2.4.19c) ensures the second derivative exists at the origin for a symmetrical flow ($\left.\frac{\partial \upsilon_z}{\partial r}\right|_{r=0} = 0$). (2.4.19d) arises from the freestream velocity condition.

There are two constants, Ch_2 and Cf_2 (in addition to β), involved in the second order problem. They will be discussed in the next chapter.

2.5 The i-th Order Problem ($i = 2,3,4\cdots$)

We will prove by mathematical induction the proposition that the i-th order quasi-similarity solution of the tip vortex can be obtained by solving the following ODEs with their boundary conditions:

$$2\eta R_i' + 2R_i = \eta^2 \cdot F_i' + 2i \cdot \eta \cdot F_i \tag{2.5.1a}$$

$$\begin{aligned} &2\eta H_i'' + (\eta^2 + 6)H_i' + 2i\eta H_i \\ &= \sum_{j=1}^{i-1} \left\{ \left(2\eta H_{i-j}' + 4H_{i-j}\right)R_j - \left(\eta^2 H_{i-j}' + 2(i-j)\eta H_{i-j}\right)F_j \right\} \end{aligned} \tag{2.5.1b}$$

$$G_i' = \eta \cdot \sum_{j=1}^{i} \left(H_j \cdot H_{i-j+1}\right) \tag{2.5.1c}$$

$$\begin{aligned} &2\eta F_i'' + (\eta^2 + 2)F_i' + 2i\eta F_i = -\beta \cdot \left[2i\eta G_i + \eta^3 \sum_{j=1}^{i} \left(H_j \cdot H_{i-j+1}\right) \right] \\ &+ \sum_{j=1}^{i-1} \left\{ 2\eta R_j \cdot F_{i-j}' - \eta F_j \cdot \left[2(i-j)F_{i-j} + \eta F_{i-j}' \right] \right\} \end{aligned} \tag{2.5.1d}$$

where β is the constant that was established in the first order problem solution. Like the second order problem, the boundary conditions of this i-th order problem are:

$$R_i(0) = 0 \tag{2.5.2a}$$

$$H_i(0) = Ch_i, \quad H_i'(0) = 0 \tag{2.5.2b}$$

$$F_i(0) = Cf_i, \quad F_i'(0) = 0 \tag{2.5.2c}$$

$$G_i(\infty) = 0 \tag{2.5.2d}$$

The following relations have to be satisfied if the quasi-similarity solutions exist:

$$U_i(\tilde{z}) = U_1^{\,i}(\tilde{z}) \tag{2.5.3a}$$

$$V_i(\tilde{z}) = \frac{1}{\sqrt{\tilde{z}}} \cdot U_1^i(\tilde{z}) \tag{2.5.3b}$$

$$P_i(\tilde{z}) = \beta \cdot U_1^i(\tilde{z}) \tag{2.5.3c}$$

$$\Psi_i(\tilde{z}) = 8\pi\beta \cdot U_1^i(\tilde{z}) \tag{2.5.3d}$$

We begin our proof by first substituting the quasi-similarity parameters into the governing equations of the i-th order problem (2.2.39), yielding:

$$\sqrt{\tilde{z}} \cdot V_i(\tilde{z}) \cdot (2\eta R_i' + 2R_i) + U_i(\tilde{z}) \cdot \left(\frac{2\tilde{z} \cdot U_i'(\tilde{z})}{U_i(\tilde{z})} \cdot \eta F_i - \eta^2 \cdot F_i' \right) = 0 \tag{2.5.4a}$$

$$\begin{aligned} &\Psi_i(\tilde{z}) \cdot \left[2\eta H_i'' + (\eta^2 + 6) \cdot H_i' - \frac{2\tilde{z} \cdot \Psi_i'(\tilde{z})}{\Psi_i(\tilde{z})} \cdot \eta H_i \right] \\ &= \sum_{j=1}^{i-1} \left\{ U_j(\tilde{z}) \cdot \Psi_{i-j}(\tilde{z}) \cdot \left[\frac{2\tilde{z} \cdot \Psi_{i-j}'(\tilde{z})}{\Psi_{i-j}(\tilde{z})} \cdot \eta H_{i-j} - \eta^2 \cdot H_{i-j}' \right] \cdot F_j \right\} \\ &+ \sum_{j=1}^{i-1} \left\{ \sqrt{\tilde{z}} \cdot V_j(\tilde{z}) \cdot \Psi_{i-j}(\tilde{z}) \cdot \left[2\eta H_{i-j}' + 4H_{i-j} \right] \cdot R_j \right\} \end{aligned} \tag{2.5.4b}$$

$$P_i(\tilde{z}) \cdot G_i' = \tilde{z} \cdot \sum_{j=1}^{i} \left\{ \Psi_j(\tilde{z}) \cdot \Psi_{i-j+1}(\tilde{z}) \cdot \left[\eta \cdot H_i \cdot H_{i-j+1} \right] \right\} \tag{2.5.4c}$$

$$\begin{aligned} &U_i(\tilde{z}) \cdot \left[2\eta F_i'' + (\eta^2 + 6) \cdot F_i' - \frac{2\tilde{z} \cdot U_i'(\tilde{z})}{U_i(\tilde{z})} \cdot \eta F_i \right] \\ &= \left[\frac{2\tilde{z} \cdot P_i'(\tilde{z})}{P_i(\tilde{z})} \cdot \eta \cdot G_i - \eta^2 \cdot G_i' \right] \cdot P_i(\tilde{z}) \\ &+ \sum_{j=1}^{i-1} \left\{ U_j(\tilde{z}) \cdot U_{i-j}(\tilde{z}) \cdot \left[\frac{2\tilde{z} \cdot U_{i-j}'(\tilde{z})}{U_{i-j}(\tilde{z})} \cdot \eta F_{i-j} - \eta^2 \cdot F_{i-j}' \right] \cdot F_j \right\} \\ &+ \sum_{j=1}^{i-1} \left\{ \sqrt{\tilde{z}} \cdot V_j(\tilde{z}) \cdot U_{i-j}(\tilde{z}) \cdot \left[2\eta F_{i-j}' \cdot R_j \right] \right\} \end{aligned} \tag{2.5.4d}$$

Now, we proceed with the proof by induction by checking that the proposition is correct for $i = 2$.

For $i = 2$, we have shown in section 2.4 that

$$U_2(\tilde{z}) = U_1^{\,2}(\tilde{z}) \tag{2.5.5a}$$

$$V_2(\tilde{z}) = \frac{1}{\sqrt{\tilde{z}}} \cdot U_1^2(\tilde{z}) \tag{2.5.5b}$$

$$P_2(\tilde{z}) = \beta \cdot U_1^2(\tilde{z}) \tag{2.5.5c}$$

$$\Psi_2(\tilde{z}) = 8\pi\beta \cdot U_1^2(\tilde{z}) \tag{2.5.5d}$$

while the quasi-similarity functions satisfy the following ODEs,

$$2\eta R_2' + 2R_2 = \eta^2 \cdot F_2' + 4\eta \cdot F_2 \tag{2.5.6a}$$

$$\begin{aligned} &2\eta \cdot H_2'' + (\eta^2 + 6) \cdot H_2' + 4\eta \cdot H_2 \\ &\quad = \left[2\eta H_1' + 4H_1\right] \cdot R_1 - \left[\eta^2 \cdot H_1' + 2\eta H_1\right] \cdot F_1 \end{aligned} \tag{2.5.6b}$$

$$G_2' = 2\eta \cdot H_1 \cdot H_2 \tag{2.5.6c}$$

$$\begin{aligned} &2\eta \cdot F_2'' + (\eta^2 + 2) \cdot F_2' + 4\eta \cdot F_2 = -\beta \cdot \left[4\eta \cdot G_2 + 2\eta^3 \cdot H_1 \cdot H_2\right] \\ &\quad + 2\eta R_1 \cdot F_1' - \eta F_1 \cdot \left[2F_1 + \eta F_1'\right] \end{aligned} \tag{2.5.6d}$$

The proposition is obviously correct for $i = 2$.

Next, we assume the proposition is correct for $i = l, \quad l \le k$. This means that for the l-th order problem:

$$U_l(\tilde{z}) = U_1^l(\tilde{z}) \tag{2.5.7a}$$

$$V_l(\tilde{z}) = \frac{1}{\sqrt{\tilde{z}}} \cdot U_1^l(\tilde{z}) \tag{2.5.7b}$$

$$P_l(\tilde{z}) = \beta \cdot U_1^l(\tilde{z}) \tag{2.5.7c}$$

$$\Psi_l(\tilde{z}) = 8\pi\beta \cdot U_1^l(\tilde{z}) \tag{2.5.7d}$$

and the quasi-similarity functions satisfy

$$2\eta R_l' + 2R_l = \eta^2 \cdot F_l' + 2l \cdot \eta \cdot F_l \tag{2.5.8a}$$

$$\begin{aligned} &2\eta H_l'' + (\eta^2 + 6) H_l' + 2l\eta H_l \\ &\quad = \sum_{j=1}^{l-1} \left\{ \left(2\eta H_{l-j}' + 4H_{l-j}\right) R_j - \left(\eta^2 H_{l-j}' + 2(l-j)\eta H_{l-j}\right) F_j \right\} \end{aligned} \tag{2.5.8b}$$

$$G_l' = \eta \cdot \sum_{j=1}^{l} \left(H_j \cdot H_{l-j+1}\right) \tag{2.5.8c}$$

$$\begin{aligned} &2\eta F_l'' + (\eta^2 + 2) F_l' + 2l\eta F_l = -\beta \cdot \left[2l\eta G_l + \eta^3 \sum_{j=1}^{l} \left(H_j \cdot H_{l-j+1}\right)\right] \\ &\quad + \sum_{j=1}^{l-1} \left\{ 2\eta R_j \cdot F_{l-j}' - \eta F_j \cdot \left[2(l-j) F_{l-j} + \eta F_{l-j}'\right] \right\} \end{aligned} \tag{2.5.8d}$$

Now, we prove the proposition is correct for $i = k+1$.

The general governing equations for (k+1)-st order problem (2.5.4), replacing i with k+1, can be written as

$$\sqrt{\tilde{z}} \cdot V_{k+1}(\tilde{z}) \cdot (2\eta R'_{k+1} + 2R_{k+1}) + U_{k+1}(\tilde{z}) \cdot \left(\frac{2\tilde{z} \cdot U'_{k+1}(\tilde{z})}{U_{k+1}(\tilde{z})} \cdot \eta F_{k+1} - \eta^2 \cdot F'_{k+1} \right) = 0 \quad (2.5.9a)$$

$$\begin{aligned} &\Psi_{k+1}(\tilde{z}) \cdot \left[2\eta H''_{k+1} + (\eta^2 + 6) \cdot H'_{k+1} - \frac{2\tilde{z} \cdot \Psi'_{k+1}(\tilde{z})}{\Psi_{k+1}(\tilde{z})} \cdot \eta H_{k+1} \right] \\ &= \sum_{j=1}^{k+1-1} \left\{ U_j(\tilde{z}) \cdot \Psi_{k+1-j}(\tilde{z}) \cdot \left[\frac{2\tilde{z} \cdot \Psi'_{k+1-j}(\tilde{z})}{\Psi_{k+1-j}(\tilde{z})} \cdot \eta H_{k+1-j} - \eta^2 \cdot H'_{k+1-j} \right] \cdot F_j \right\} \\ &+ \sum_{j=1}^{k+1-1} \left\{ \sqrt{\tilde{z}} \cdot V_j(\tilde{z}) \cdot \Psi_{k+1-j}(\tilde{z}) \cdot \left[2\eta H'_{k+1-j} + 4H_{k+1-j} \right] \cdot R_j \right\} \end{aligned} \quad (2.5.9b)$$

$$P_{k+1}(\tilde{z}) \cdot G'_{k+1} = \tilde{z} \cdot \sum_{j=1}^{k+1} \left\{ \Psi_j(\tilde{z}) \cdot \Psi_{k+1-j+1}(\tilde{z}) \cdot \left[\eta \cdot H_{k+1} \cdot H_{k+1-j+1} \right] \right\} \quad (2.5.9c)$$

$$\begin{aligned} &U_{k+1}(\tilde{z}) \cdot \left[2\eta F''_{k+1} + (\eta^2 + 6) \cdot F'_{k+1} - \frac{2\tilde{z} \cdot U'_{k+1}(\tilde{z})}{U_{k+1}(\tilde{z})} \cdot \eta F_{k+1} \right] \\ &= \left[\frac{2\tilde{z} \cdot P'_{k+1}(\tilde{z})}{P_{k+1}(\tilde{z})} \cdot \eta \cdot G_{k+1} - \eta^2 \cdot G'_{k+1} \right] \cdot P_{k+1}(\tilde{z}) \\ &+ \sum_{j=1}^{k+1-1} \left\{ U_j(\tilde{z}) \cdot U_{k+1-j}(\tilde{z}) \cdot \left[\frac{2\tilde{z} \cdot U'_{k+1-j}(\tilde{z})}{U_{k+1-j}(\tilde{z})} \cdot \eta F_{k+1-j} - \eta^2 \cdot F'_{k+1-j} \right] \cdot F_j \right\} \\ &+ \sum_{j=1}^{k+1-1} \left\{ \sqrt{\tilde{z}} \cdot V_j(\tilde{z}) \cdot U_{k+1-j}(\tilde{z}) \cdot \left[2\eta F'_{k+1-j} \cdot R_j \right] \right\} \end{aligned} \quad (2.5.9d)$$

By using (2.5.7), it is apparent the following equations must be satisfied for quasi-similarity solutions to exist,

$$U_{k+1}(\tilde{z}) = \frac{1}{c_{k+1}} \cdot U_1^{k+1}(\tilde{z}) \quad (2.5.10a)$$

$$V_{k+1}(\tilde{z}) = \frac{1}{c_{k+1} \cdot \sqrt{\tilde{z}}} \cdot U_1^{k+1}(\tilde{z}) \quad (2.5.10b)$$

$$P_{k+1}(\tilde{z}) = \frac{\beta_{k+1}}{\beta \cdot c_{k+1}} \cdot P_1(\tilde{z}) \cdot U_1^k(\tilde{z}) \tag{2.5.10c}$$

$$\Psi_{k+1}(\tilde{z}) = \frac{1}{\alpha_{k+1}} \cdot \Psi_1(\tilde{z}) \cdot U_1^k(\tilde{z}) = \frac{\beta_{k+1}}{\beta \cdot c_{k+1}} \cdot \Psi_1(\tilde{z}) \cdot U_1^k(\tilde{z}) \tag{2.5.10d}$$

where c_{k+1} , β_{k+1} and α_{k+1} are constants. β is the constant appearing in the first order problem. Like the second order problem, there are only two independent constants (except β). It is permissible to select $c_{k+1}=1$ and $\alpha_{k+1}=1$, and at the same time let $H_i(0)=Ch_i$ and $F_i(0)=Cf_i$ without loss of generality. Thus $\beta_{k+1} = \beta \cdot \frac{c_{k+1}}{\alpha_{k+1}} = \beta$. Therefore the amplitude functions (2.5.10a-d) can be rewritten as

$$U_{k+1}(\tilde{z}) = U_1^{k+1}(\tilde{z}) \tag{2.5.11a}$$

$$V_{k+1}(\tilde{z}) = \frac{1}{\sqrt{\tilde{z}}} \cdot U_1^{k+1}(\tilde{z}) \tag{2.5.11b}$$

$$P_{k+1}(\tilde{z}) = \beta \cdot U_1^{k+1}(\tilde{z}) \tag{2.5.11c}$$

$$\Psi_{k+1}(\tilde{z}) = 8\pi\beta \cdot U_1^{k+1}(\tilde{z}) \tag{2.5.11d}$$

Thus, (2.5.9) can be rewritten as:

$$2\eta R'_{k+1} + 2R_{k+1} = \eta^2 \cdot F'_{k+1} + 2(k+1) \cdot \eta \cdot F_{k+1} \tag{2.5.12a}$$

$$\begin{aligned} &2\eta H''_{k+1} + \left[\eta^2 + 6\right] H'_{k+1} + 2(k+1)\eta H_{k+1} \\ &= \sum_{j=1}^{k+1-1} \left\{ \left(2\eta H'_{k+1-j} + 4H_{k+1-j}\right) R_j - \left[\eta^2 H'_{k+1-j} + 2(k+1-j)\eta H_{k+1-j}\right] F_j \right\} \end{aligned} \tag{2.5.12b}$$

$$G'_{k+1} = \eta \cdot \sum_{j=1}^{k+1} \left(H_j \cdot H_{k+1-j+1}\right) \tag{2.5.12c}$$

$$
\begin{aligned}
&2\eta F''_{k+1} + (\eta^2+2)F'_{k+1} + 2(k+1)\eta F_{k+1} \\
&\quad = -\beta\cdot\left[2(k+1)\eta G_{k+1} + \eta^3\sum_{j=1}^{k+1}\left(H_j\cdot H_{k+1-j+1}\right)\right] \\
&\quad + \sum_{j=1}^{k+1-1}\left\{2\eta R_j\cdot F'_{k+1-j} - \eta F_j\cdot\left[2(k+1-j)F_{k+1-j} + \eta F'_{k+1-j}\right]\right\}
\end{aligned}
\tag{2.5.12d}
$$

where β is the constant of the first order problem.

The proposition is correct for $i = k+1$, provided that it is correct for $i = l$, $l \le k$. Since the proposition is correct for i=2, this concludes the proof by mathematical induction.

2.6 The Solutions in Complete Function Form

Combining all the results obtained previously, the quasi-similarity solution of vortex flow in a freestream is given by:

$$\upsilon_z(z,r) = U_\infty\cdot\left[1+\sum_{i=1}^{\infty}U_1^i(z)\cdot F_i(\eta)\right] \tag{2.6.1}$$

$$\upsilon_r(z,r) = \sqrt{\frac{U_\infty\nu}{z}}\cdot\sum_{i=1}^{\infty}U_1^i(z)\cdot R_i(\eta) \tag{2.6.2}$$

$$\psi(z,r) = \frac{8\pi\beta\cdot U_\infty^2}{\Gamma}\cdot\sum_{i=1}^{\infty}U_1^i(z)\cdot H_i(\eta) \tag{2.6.3}$$

or $$\upsilon_\theta(z,r) = \frac{8\pi\beta\cdot\sqrt{U_\infty^3\cdot\nu\cdot z}}{\Gamma}\cdot\sum_{i=1}^{\infty}U_1^i(z)\cdot T_i(\eta) \tag{2.6.4}$$

where $T_i(\eta) = \eta H_i(\eta)$

$$p(z,r) - p_\infty = \rho U_\infty^2\beta\cdot\sum_{i=1}^{\infty}U_1^i(z)\cdot G_i(\eta) \tag{2.6.5}$$

where $\eta = r\sqrt{\dfrac{U_\infty}{\nu z}}$, and

$$U_1(z) = \frac{1}{64\pi^2\beta}\cdot\frac{\Gamma^2}{U_\infty\cdot\nu\cdot z} \tag{2.6.6}$$

where β is a constant. The solutions (2.6.1)-(2.6.5) are convergent provided that the similarity functions are of the order of unity and

$$|U_1(z)| < 1 \tag{2.6.7}$$

The quasi-similarity functions of arbitrary i-th order $H_i(\eta)$, $G_i(\eta)$, $F_i(\eta)$ and $R_i(\eta)$ can be solved one by one from lower order to higher order by solving the ODEs (2.5.1) with the boundary conditions (2.5.2). Details will be discussed in the next chapter.

2.7 Discussion Of Assumptions

Five assumptions have been made to derive the governing equations (2.2.5) - (2.2.9) used in this analysis. Those assumptions are:

(1) incompressible, steady, laminar flow

(2) axisymmetric flow

(3) $\upsilon_r << \upsilon_\theta$

(4) $\dfrac{\partial^2 \upsilon_\theta}{\partial z^2} << \dfrac{\partial^2 \upsilon_\theta}{\partial r^2}$; $\quad \dfrac{\partial^2 \upsilon_z}{\partial z^2} << \dfrac{\partial^2 \upsilon_z}{\partial r^2}$

(5) the circulation of the vortex is independent of the downstream distance

The first two assumptions are straightforward, although they will be violated by any mechanism that causes vortex instability. Consider now the third and fourth assumptions. Using (2.6.2) and (2.6.4), one finds

$$\frac{\upsilon_r}{\upsilon_\theta} \propto \sqrt{\frac{U_\infty \cdot \nu}{z}} \cdot \left\{ \frac{\Gamma}{8\pi\sqrt{U_\infty^3 \cdot \nu z}} \right\} \propto \frac{\nu}{\Gamma} \cdot U_1(z) \tag{2.7.1}$$

Also, because $\eta = r\sqrt{\dfrac{U_\infty}{\nu z}}$, (2.3.3) together with (2.3.5) yields

$$\frac{\dfrac{\partial^2}{\partial z^2}}{\dfrac{\partial^2}{\partial r^2}} = \left(\frac{\nu}{\Gamma}\right)^2 \cdot \frac{\dfrac{\partial^2}{\partial \tilde{z}^2}}{\dfrac{\partial^2}{\partial \tilde{r}^2}} \propto \left(\frac{\nu}{\Gamma}\right)^2 \cdot \frac{\dfrac{1}{4 \cdot \tilde{z}^2}}{\dfrac{\eta^2}{\tilde{r}^2}} = \left(\frac{\nu}{\Gamma}\right)^2 \cdot \frac{1}{4 \cdot \tilde{z}} \propto \left(\frac{\nu}{\Gamma}\right)^2 \cdot U_1(z) \tag{2.7.2}$$

One can verify that the terms in the governing equations neglected due to assumptions (3) and (4) are proportional to $\left(\dfrac{\nu}{\Gamma}\right)^2 \cdot U_1(z)$. In contrast, other terms in the governing

equations are of order unity. Assumptions (3) and (4) are justified provided that the vortex circulation is much greater than the kinematic viscosity of the fluid. Because the kinematic viscosity is commonly very small ($\nu \approx 10^{-6} m^2 / s$ for the laminar flow of water, $\nu \approx 10^{-5} m^2 / s$ for the laminar flow of air), these assumptions will almost always be justified for real wing tip vortex flows.

The fifth assumption — that the circulation of the tip vortex is independent of downstream distance — is a consequence of the Helmholtz vortex law requirement that vortex lines not terminate in a fluid. The assumption could be violated if vortex lines doubled back on themselves to form vortex rings, but this behaviour does not occur in the quasi-similarity solution. Alternatively, it can be viewed as a consequence of Kelvin's Theorem ($D\Gamma / Dt = 0$). Kelvin's Theorem applies here because on a material loop far from the vortex axis there is negligible effect of viscosity, and this flow is incompressible and without body forces.

The assumptions made in the derivation of the quasi-similarity solutions are thus not particularly restrictive. Rather, convergence problems of the quasi-similarity solutions more significantly limit their application. In particular, these limitations can be represented mathematically by,

$$|U_1(z)| < 1 \tag{2.7.3}$$

The first order axial velocity excess or deficit in the vortex in a freestream is thus constrained to being less than the magnitude of the freestream velocity.

Finally, let us discuss the quasi-similarity solutions. The quasi-similarity expressions (2.6.1)-(2.6.5) can be verified to be the solution of the governing system (2.2.5)-(2.2.8) consisting of the continuity equation and simplified N-S equation. Substitution of (2.6.1)-(2.6.5) into (2.2.5)-(2.2.8) yields:

$$\frac{1}{2\tilde{z}} \cdot \sum_{i=1}^{\infty} \left\{ U_1^i(\tilde{z}) \cdot C_{Oi}(R_i, F_i) \right\} \equiv 0 \tag{2.7.4a}$$

$$\frac{8\pi\beta}{2\tilde{z}} \cdot \sum_{i=1}^{\infty} \left\{ U_1^i(\tilde{z}) \cdot M_{Oi}^T(H_i, \beta) \right\} \equiv 0 \tag{2.7.4b}$$

$$\frac{\beta}{2\tilde{z}} \cdot \sum_{i=1}^{\infty} \left\{ U_1^i(\tilde{z}) \cdot M_{Oi}^R(G_i, H_i) \right\} \equiv 0 \tag{2.7.4c}$$

$$\frac{1}{2\tilde{z}} \cdot \sum_{i=1}^{\infty} \left\{ U_1^i(\tilde{z}) \cdot M_{Oi}^A(F_i, G_i, H_i, \beta) \right\} \equiv 0 \qquad (2.7.4d)$$

provided $|U_1(\tilde{z})| < 1$, because

$$C_{Oi}(R_i, F_i) = M_{Oi}^T(H_i, \beta) = M_{Oi}^R(G_i, H_i) = M_{Oi}^A(F_i, G_i, H_i, \beta) \equiv 0, \qquad i=1,2,3,...$$

where C_{Oi} represents the continuity similarity equation (2.5.1a), M_{Oi}^T the tangential momentum similarity equation (2.5.1b), M_{Oi}^R the radial momentum similarity equation (2.5.1c), and M_{Oi}^A the axial momentum similarity equation (2.5.1d).

Therefore, the first order terms in the polynomial are the approximate solution of the governing equation with accuracy of $O(U_1^2(\tilde{z}))$ (order $U_1^2(\tilde{z})$). The residue for the second order solution is $O(U_1^3(\tilde{z}))$. To summarize, the quasi-similarity solution exists provided $|U_1(\tilde{z})| < 1$. The more terms in the polynomial we obtain, the more accurate is the solution.

2.8 Conclusions

A quasi-similarity method for 3-D vortices in a freestream is discussed in this chapter. The general solution in polynomial form has been found. The quasi-similarity solutions are divergent when $z < \frac{1}{64\pi^2\beta} \cdot \frac{\Gamma^2}{U_\infty \cdot \nu}$ (or $U_1(z) > 1$). Thus, these solutions are most accurate far downstream. The quasi-similarity solutions have some interesting features. All three velocity components decrease with increasing downstream distance. The radial velocity diminishes mostly rapidly, followed by the axial velocity. The tangential velocity changes most slowly. For example, for the first order problem, the tangential velocity decays as one over the square root of the downstream distance, while the axial velocity is proportional to one over the downstream distance, and the radial velocity is proportional to one over the downstream distance to the power of 1.5.

Chapter 3 Quasi-Similarity Solutions for Wing Tip Vortices

In the previous chapter, the quasi-similarity method was discussed. The solutions in polynomial form of the nonlinear governing equations have been presented. Each term in the polynomial consists of the product of two functions. One function is called the amplitude function, and is a function of downstream distance only. The other function, called the similarity function, is a function of a similarity variable that is a combination of the radial coordinate and the axial coordinate. The amplitude functions of each polynomial term have been obtained in the previous chapter. The ODEs and boundary conditions for the similarity functions in each order of the polynomial have also been listed. There is one constant, β, involved in the first order problem, whereas two constants, Ch_i and Cf_i , are involved in the higher order problems ($i \geq 2$). In this chapter, we solve the first and second order problems numerically and analytically. It is found that the constant β is closely related to the total wing drag. The two constants Ch_i and Cf_i ($i \geq 2$) can be evaluated as well. The quasi-similarity solutions meet the requirements that the vortex circulation and wing total drag are independent of the downstream distance. Fortunately, first order velocity components and pressure in completed functional form can be obtained. The tangential velocity component and pressure in the second order problem can be presented in completed functional form as well. Second order axial velocity and radial velocity similarity functions can only be calculated numerically. The numerical procedure to be used for solving higher order problems will also be mentioned briefly.

3.1 The First Order Solutions

3.1.1 General first order solution in complete function form

The first order problem consists of four ODEs for the similarity functions, along with the proper boundary conditions:

$$2\eta R_1'(\eta) + 2R_1(\eta) = \eta^2 \cdot F_1'(\eta) + 2\eta \cdot F_1(\eta) \tag{3.1.1}$$

$$2\eta \cdot H_1''(\eta) + (\eta^2 + 6) \cdot H_1'(\eta) + 2\eta \cdot H_1(\eta) = 0 \tag{3.1.2}$$

$$G_1'(\eta) = \eta \cdot H_1^2(\eta) \tag{3.1.3}$$

$$2\eta \cdot F_1''(\eta) + (\eta^2 + 2) \cdot F_1'(\eta) + 2\eta \cdot F_1(\eta) = -\beta \cdot \left[2\eta \cdot G_1(\eta) + \eta^3 \cdot H_1^2(\eta)\right] \tag{3.1.4}$$

where β is a constant. The boundary conditions of this first order problem are

$$R_1(0) = 0 \tag{3.1.5}$$

$$H_1(0) = 1.0, \quad H_1'(0) = 0 \tag{3.1.6}$$

$$F_1(0) = 1.0, \quad F_1'(0) = 0 \tag{3.1.7}$$

$$G_1(\infty) = 0 \tag{3.1.8}$$

(3.1.5) must hold to ensure the flow is symmetrical about the vortex centerline. We apply the first equation of (3.1.6) because the choice of value of $H_1(0)$ does not affect the final results (one of the characteristics of the similarity method). The second equation of (3.1.6) ensures the second derivative at the origin has a finite value for an axisymmetric flow. The first equation of (3.1.7) holds because β is a free constant, the second condition ensures the second derivative exists at the origin for a symmetrical flow. (3.1.8) arises from the freestream velocity condition.

The following relations must hold if quasi-similarity solutions exist:

$$U_1(\tilde{z}) = \frac{1}{64\pi^2\beta \cdot \tilde{z}} \tag{3.1.9}$$

$$V_1(\tilde{z}) = \frac{U_1(\tilde{z})}{\sqrt{\tilde{z}}} \tag{3.1.10}$$

$$P_1(\tilde{z}) = \beta \cdot U_1(\tilde{z}) \tag{3.1.11}$$

$$\Psi_1(\tilde{z}) = \frac{1}{8\pi \cdot \tilde{z}} = 8\pi\beta \cdot U_1(\tilde{z}) \tag{3.1.12}$$

The ODEs (3.1.1)-(3.1.4) are decoupled. The non-singular solution of (3.1.2) with the boundary conditions (3.1.6) is

$$H_1(\eta) = \frac{4}{\eta^2}\left(1 - e^{-\frac{\eta^2}{4}}\right) \tag{3.1.13}$$

Thus, the solution of (3.1.3) with boundary condition (3.1.8) is

$$G_1(\eta)=\frac{-8+16e^{-\frac{\eta^2}{4}}-8e^{-\frac{\eta^2}{2}}}{\eta^2}-4Ei\left(1,\frac{\eta^2}{4}\right)+4Ei\left(1,\frac{\eta^2}{2}\right) \tag{3.1.14}$$

where $Ei(n,x)=\int_1^{\infty}\frac{e^{-xt}}{t^n}\cdot dt$ is the exponential integral function. Substituting (3.1.13) and (3.1.14) into (3.1.4), one finds that the solution of (3.1.4) with the boundary conditions (3.1.7) is

$$F_1(\eta)=4\beta\cdot e^{-\frac{\eta^2}{4}}\cdot\int_0^{\eta}\left\{\frac{1}{y}e^{\frac{y^2}{4}}\cdot\left[Ei\left(2,\frac{y^2}{2}\right)-2Ei\left(2,\frac{y^2}{4}\right)+1\right]\right\}\cdot dy+e^{-\frac{\eta^2}{4}} \tag{3.1.15}$$

The solution of (3.1.1) with the boundary condition (3.1.5) is

$$R_1(\eta)=\frac{\eta}{2}\cdot F_1(\eta) \tag{3.1.16}$$

where $F_1(\eta)$ is given by (3.1.15).

By combining the amplitude functions and similarity functions obtained above, one can get the first order solutions in completed function form.

$$\upsilon_{z(1)}=\frac{\Gamma^2}{16\pi^2\nu z}\cdot\left\{e^{-\frac{\eta^2}{4}}\cdot\int_0^{\eta}\frac{1}{y}e^{\frac{y^2}{4}}\left[Ei\left(2,\frac{y^2}{2}\right)-2Ei\left(2,\frac{y^2}{4}\right)+1\right]\cdot dy+\frac{1}{4\beta}\cdot e^{-\frac{\eta^2}{4}}\right\} \tag{3.1.17}$$

$$\upsilon_{\theta(1)}=\sqrt{\frac{U_\infty}{\nu z}}\cdot\frac{\Gamma}{2\pi\eta}\cdot\left(1-e^{-\frac{\eta^2}{4}}\right)=\frac{\Gamma}{2\pi r}\cdot\left(1-e^{-\frac{\eta^2}{4}}\right) \tag{3.1.18}$$

$$\upsilon_{r(1)}=\frac{\Gamma^2}{32\pi^2\sqrt{U_\infty\cdot\nu}\cdot z^{1.5}}\cdot\left\{\eta e^{-\frac{\eta^2}{4}}\cdot\int_0^{\eta}\frac{1}{y}e^{\frac{y^2}{4}}\left[Ei\left(2,\frac{y^2}{2}\right)-2Ei\left(2,\frac{y^2}{4}\right)+1\right]\cdot dy+\frac{1}{4\beta}\cdot\eta e^{-\frac{\eta^2}{4}}\right\} \tag{3.1.19}$$

$$p_{(1)}=\frac{\rho U_\infty\cdot\Gamma^2}{16\pi^2\nu\cdot z}\cdot\left\{-\frac{2}{\eta^2}\left(1-e^{-\frac{\eta^2}{4}}\right)^2+Ei\left(1,\frac{\eta^2}{2}\right)-Ei\left(1,\frac{\eta^2}{4}\right)\right\} \tag{3.1.20}$$

Equations (3.1.17)-(3.1.19) show that the radial velocity in a tip vortex falls most rapidly (as $z^{-1.5}$) with downstream distance. The axial velocity changes more slowly with z (roughly as z^{-1}), and the tangential velocity varies most slowly with downstream distance (as $z^{-0.5}$).

It is interesting to note that this first order tangential velocity distribution is identical to that of the Lamb-Oseen vortex provided one replaces the time variable in the Lamb-Oseen problem with its equivalent, z/U_∞, in the tip vortex problem.

The Runge-Kutta method was also used to solve the first order problem. The Runge-Kutta results agree to within numerical error with the exact analytical results given by (3.1.13)-(3.1.16). The results corresponding to $\beta = 0.361$ (this is the case when the second derivative of the axial velocity component in the radial direction at the origin is zero) are shown in Figure 3.1. $T_1(\eta) = \eta \cdot H_1(\eta)$ is the similarity function for the tangential velocity component in the tip vortex.

3.1.2 Tangential velocity and pressure

Notice that the first order tangential velocity component and pressure distribution are independent of the constant β. We note in addition that

$$G_1(0) \approx -2.773 \qquad (3.1.21)$$

and this result is also independent of β.

Furthermore, $T_1(\eta) = \eta H_1(\eta)$, the function describing the radial distribution of tangential velocity, is a maximum when $\eta = 2.25$, and its maximum value is

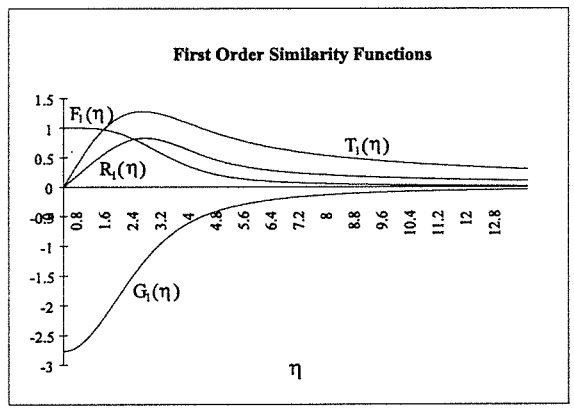

Figure 3.1 The first order quasi-similarity functions. $\beta = 0.361$

$$T_1(\eta = 2.25) = 1.2763 \qquad (3.1.22)$$

Thus, to first order, the radius of a tip vortex (R_{1c}) is given by

$$R_{1c} = 2.25 \cdot \sqrt{\frac{\nu \cdot z}{U_\infty}}, \qquad \text{or} \quad \frac{R_{1c}}{z} = \frac{2.25}{\sqrt{\mathrm{Re}_z}} \qquad (3.1.23)$$

The similarity between the growth of a tip vortex and the growth of a laminar, zero-pressure-gradient boundary layer (for which $\delta/x \approx 5/\sqrt{\mathrm{Re}_x}$) is apparent.

The first order vortex radius is independent of the constant β. This independence implies that the radius of the wing tip vortex far downstream (where the first order solution is a good approximation) increases as the square root of the downstream distance.

3.1.3 Effects of the constant β on the axial similarity functions

The first order axial velocity consists of an amplitude function multiplied by a similarity function. The amplitude function is always positive if the constant β is positive. The similarity functions corresponding to several positive values of the constant β are plotted in Figure 3.2. When β equals 0.361, the second order derivative at the origin is zero. For β >0.361 the peak in the axial velocity distribution occurs away from the vortex axis. This finding is consistent with observations by Mason and Marchman (1972) of a real wing tip vortex. For 0<β <0.361 there is still an axial velocity excess in the tip vortex, although the axial velocity decreases monotonically from the centerline. Green and Acosta (1991) have observed similar behaviour.*

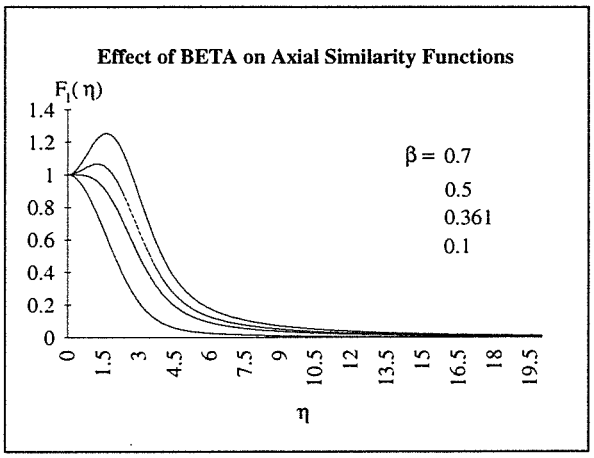

Figure 3.2 Axial velocity excess in wing tip vortices. (The curves from top to bottom correspond with the values of β listed in the column to the right)

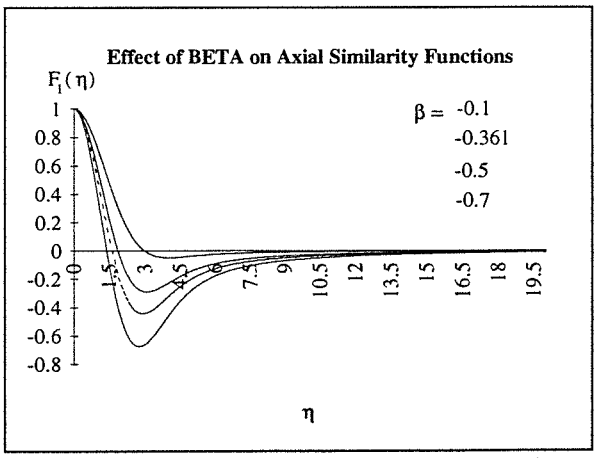

Figure 3.3 Axial velocity deficit in wing tip vortices. (The curves from top to bottom correspond with the values of β listed in the column to the right)

When β is negative, the first order

* One must be careful with these comparisons. As we shall see, β>0 corresponds with negative wing drag, which was not the case for either of the two experiments mentioned. In addition, both experiments were carried out for small z, where this theory likely does not apply.

amplitude function is always negative. The first order similarity function is shown in Figure 3.3. Because the axial velocity is the product of these two functions, the behaviour shown in Figure 3.3 implies a centerline axial velocity deficit combined with a small core edge velocity excess. This kind of axial velocity distribution was reported by Logan (1971) and Thompson(1975).

Baker (1974) and Green and Acosta (1991) also observed an axial velocity deficit by using LDV and PIV respectively. However, they did not report a core edge velocity excess, possibly because of the small downstream distance in their experiments, or their comparatively high (and therefore turbulent) vortex Reynolds number.

3.2 Drag due to a single quasi-similar vortex in viscous flow

A single trailing vortex is considered in this section. The axial momentum equation will be applied to a control surface enclosing the wing tip region. The control surface has the form of a right cylinder with generator parallel to the z-axis, which marks the centerline of the wing tip vortex, and the area A at each end face (Figure 3.4). The upstream end face and the curved surface of the cylinder are both at a large distance from the wing tip (compared with the vortex radius*), so that conditions there are approximately as in the freestream. Then, in the usual way, we find

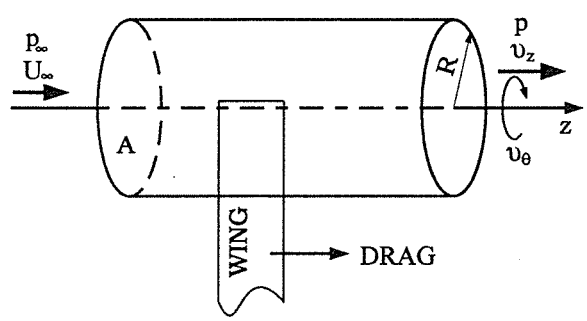

Figure 3.4 Control volume around the wing tip.

z-momentum flux outwards across curved surface = $\rho U_\infty \cdot \int (U_\infty - \upsilon_z) \cdot dA$

z-momentum flux outwards across end face = $\rho \int (\upsilon_z^2 - U_\infty^2) \cdot dA$

resultant normal force on end faces = $\int (p_\infty - p) \cdot dA$

* Tip vortex radius is just a few percent of the chord (Green and Acosta 1991, Fruman et al. 1995), so it is possible to select a radius that is large relative to the vortex yet small relative to the wing. Batchelor (1964) used the same control volume.

where υ_z and p are, respectively, the z-component of the velocity and the pressure at the downstream end face, a distance z from the wing tip. One can verify that the ratio of the shearing force on the curved surface of the control volume over the force due to pressure gradient and momentum exchange is proportional to $\tilde{z}/\tilde{R}^2$. The viscous stress at the control surface is therefore small and can be neglected, when $\tilde{R}$ approaches infinity. The drag D on the wing due to this single vortex is thus given by

$$D = \int \left\{ p_\infty - p + \rho \upsilon_z \cdot (U_\infty - \upsilon_z) \right\} \cdot dA \tag{3.2.1}$$

The integral of (3.2.1) can be represented as a polynomial by using the previously derived formulae for pressure and axial velocity components in the vortex.

$$\begin{aligned} & p_\infty - p + \rho \upsilon_z \cdot (U_\infty - \upsilon_z) \\ & = -\rho U_\infty^2 \cdot \sum_{i=1}^{\infty} \left\{ U_1^i(\tilde{z}) \cdot \left[\beta \cdot G_i(\eta) + F_i(\eta) + \sum_{j=1}^{i-1} F_j(\eta) \cdot F_{i-j}(\eta) \right] \right\} \end{aligned} \tag{3.2.2}$$

Substituting (3.2.2) into (3.2.1), the drag of this single vortex can be represented as

$$D = -2\pi\rho \cdot \Gamma^2 \cdot \sum_{i=1}^{\infty} \left\{ \tilde{z} U_1^i(\tilde{z}) \cdot \int_0^\infty \left[\beta \cdot G_i(\eta) + F_i(\eta) + \sum_{j=1}^{i-1} F_j(\eta) \cdot F_{i-j}(\eta) \right] \cdot \eta \cdot d\eta \right\}$$

or

$$D = -2\pi\rho \cdot \Gamma^2 \cdot \sum_{i=1}^{\infty} \left\{ \left(\frac{1}{64\pi^2\beta} \right)^i \cdot \frac{1}{\tilde{z}^{i-1}} \cdot \int_0^\infty \left[\beta \cdot G_i(\eta) + F_i(\eta) + \sum_{j=1}^{i-1} F_j(\eta) \cdot F_{i-j}(\eta) \right] \cdot \eta \cdot d\eta \right\} \tag{3.2.3}$$

Because the wing drag is independent of downstream distance $\tilde{z}$, (3.2.3) implies

$$D = -\frac{\rho\Gamma^2}{32\pi} \cdot \lim_{\eta_R \to \infty} \int_0^{\eta_R} \left[G_1(\eta) + \frac{F_1(\eta)}{\beta} \right] \cdot \eta \cdot d\eta, \qquad \text{for } i = 1 \tag{3.2.4}$$

and $$\int_0^\infty \left[\beta \cdot G_i(\eta) + F_i(\eta) + \sum_{j=1}^{i-1} F_j(\eta) \cdot F_{i-j}(\eta) \right] \cdot \eta \cdot d\eta = 0, \quad \text{for } i \geq 2 \tag{3.2.5}$$

At first glance, $G_1(\eta) \propto \frac{1}{\eta^2}$ at large radius, and therefore the integration in (3.2.4) seems to be logarithmically divergent in the outer field (which is why the limit has been

taken in that integration). However, we will verify that the integration is finite because $\frac{F_1(\eta)}{\beta} \propto \frac{1}{\eta^2}$ for large radii too, and fortuitously the $1/\eta^2$ terms cancel.

Now let us consider the integration in the first order drag. Because

$$\lim_{\eta_R\to\infty}\int_0^{\eta_R}\frac{F_1(\eta)}{\beta}\eta\cdot d\eta = \lim_{\eta_R\to\infty}\int_0^{\eta_R}\left\{4e^{-\frac{\eta^2}{4}}\cdot\int_0^{\eta}\frac{e^{\frac{y^2}{4}}}{y}\cdot\left[Ei\left(2,\tfrac{y^2}{2}\right)-2Ei\left(2,\tfrac{y^2}{4}\right)+1\right]\cdot dy+\frac{1}{\beta}\cdot e^{-\frac{\eta^2}{4}}\right\}\cdot\eta d\eta$$

$$=-8\lim_{\eta_R\to\infty}\int_0^{\eta_R}\left\{\int_0^{\eta}\frac{e^{\frac{y^2}{4}}}{y}\cdot\left[Ei\left(2,\frac{y^2}{2}\right)-2Ei\left(2,\frac{y^2}{4}\right)+1\right]\cdot dy\right\}\cdot d\left(e^{-\frac{\eta^2}{4}}\right)+\frac{2}{\beta}$$

$$=\lim_{\eta_R\to\infty}\int_0^{\eta_R}\left\{\frac{8}{\eta}\cdot\left[Ei\left(2,\frac{\eta^2}{2}\right)-2Ei\left(2,\frac{\eta^2}{4}\right)+1\right]\right\}\cdot d\eta+\frac{2}{\beta} \qquad (3.2.6)$$

Thus,

$$\lim_{\eta_R\to\infty}\int_0^{\eta_R}\left[G_1(\eta)+\frac{F_1(\eta)}{\beta}\right]\cdot\eta d\eta$$

$$=\lim_{\eta_R\to\infty}\int_0^{\eta_R}\left\{\frac{-8}{\eta}\left(1-e^{-\frac{\eta^2}{4}}\right)^2+4\eta\left[Ei\left(1,\frac{\eta^2}{2}\right)-Ei\left(1,\frac{\eta^2}{4}\right)\right]+\frac{8}{\eta}\left[Ei\left(2,\frac{\eta^2}{2}\right)-2Ei\left(2,\frac{\eta^2}{4}\right)+1\right]\right\}\cdot d\eta+\frac{2}{\beta}$$

$$=\int_0^{\infty}\left\{\frac{16e^{-\frac{\eta^2}{4}}-8e^{-\frac{\eta^2}{2}}+8Ei\left(2,\frac{\eta^2}{2}\right)-16Ei\left(2,\frac{\eta^2}{4}\right)}{\eta}+4\eta\left[Ei\left(1,\tfrac{\eta^2}{2}\right)-Ei\left(1,\tfrac{\eta^2}{4}\right)\right]\right\}\cdot d\eta+\frac{2}{\beta} \qquad (3.2.7)$$

The integration on the right side of the above equation was proved to be zero using Maple V, a symbol manipulation software package. The drag due to a single quasi-similar wing tip vortex is therefore inversely proportional to the constant β:

$$D=-\frac{\rho\Gamma^2}{32\pi}\cdot\lim_{\eta_R\to\infty}\int_0^{\eta_R}\left[G_1(\eta)+\frac{F_1(\eta)}{\beta}\right]\cdot\eta\cdot d\eta=-\frac{\rho\Gamma^2}{16\pi\beta} \qquad (3.2.8)$$

It has been assumed in the analysis of Chapter 2 that the distance between the two wing tip vortices is much larger than the vortex radius, and therefore that interference between the two vortices (e.g. the Crow instability) is negligible. The total drag on the wing is thus two times the drag due to a single vortex:

$$D_w=2\cdot D=-\frac{\rho\Gamma^2}{8\pi\beta} \qquad (3.2.9a)$$

Thus, $\beta = -\dfrac{\rho\Gamma^2}{8\pi \cdot D_w}$ (3.2.9b)

In Figure 3.5 the non-dimensional axial velocity (defined as the axial velocity divided by the term $\dfrac{\Gamma^2}{16\pi^2 \nu \cdot z}$) is plotted against the non-dimensional drag (defined as $\dfrac{2\pi \cdot D_w}{\rho\Gamma^2}$). The larger the drag, the greater the deficit of the axial velocity on the vortex centerline. In a real trailing vortex, an axial velocity excess is often observed just downstream of the trailing edge (Green and Acosta 1991). This velocity excess occurs as a result of the wing tip roll up. After the shed vorticity has been fully rolled-up into the wing tip vortices, usually far downstream of the wing, only an axial velocity deficit can exist for a wing experiencing a positive drag force. An axial velocity excess can exist far downstream of a wing generating thrust (e.g. with tip mounted engines).

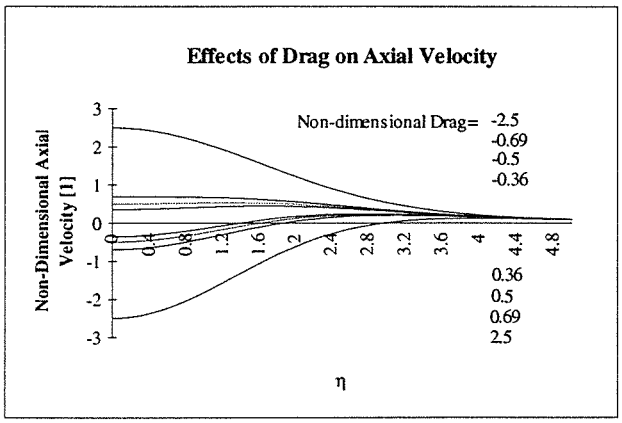

Figure 3.5 The effects of wing total drag on the axial velocity. (The different curves from top to bottom correspond with the different non-dimensional drags tabulated to the right)

Figure 3.6 shows the non-dimensional radial velocity (defined as the radial velocity divided by the term $\dfrac{\Gamma^2}{16\pi^2\sqrt{U_\infty \nu} \cdot z^{1.5}}$) as a function of the non-dimensional drag. The amplitude of radial velocity is small ($\dfrac{\upsilon_{r(1)}}{\upsilon_{z(1)}} \propto \dfrac{\nu}{\Gamma}\sqrt{U_1(\tilde{z})} \propto \dfrac{\nu}{\Gamma}$), and it decays more rapidly along z than does the axial velocity. Despite its small value, the radial velocity has important effect on the second order terms. As will be mentioned in section 3.3, the existence of a radial velocity leads

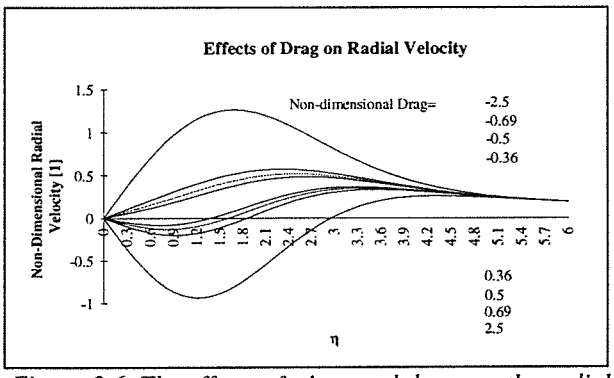

Figure 3.6 The effects of wing total drag on the radial velocity. (The different curves from top to bottom correspond with the different non-dimensional drags tabulated to the right)

to one important conclusion of this chapter — the second order tangential velocity must be zero.

3.3 The second order solutions

Substitution of the first order solution (3.1.16) into ODEs (2.4.18a-d), which specify the second order problem, yields

$$2\eta R_2'(\eta)+2R_2(\eta)=\eta^2\cdot F_2'(\eta)+4\eta\cdot F_2(\eta) \tag{3.3.1a}$$

$$2\eta\cdot H_2''(\eta)+(\eta^2+6)\cdot H_2'(\eta)+4\eta\cdot H_2(\eta)=0 \tag{3.3.1b}$$

$$G_2'(\eta)=2\eta\cdot H_1(\eta)\cdot H_2(\eta) \tag{3.3.1c}$$

$$\begin{aligned}&2\eta\cdot F_2''(\eta)+(\eta^2+2)\cdot F_2'(\eta)+4\eta\cdot F_2(\eta)\\&\quad=-\beta\cdot\left[4\eta\cdot G_2(\eta)+2\eta^3\cdot H_1(\eta)\cdot H_2(\eta)\right]-2\eta F_1^2(\eta)\end{aligned} \tag{3.3.1d}$$

where β is the constant that was established in the first order problem. The boundary conditions of this second order problem are

$$R_2(0)=0 \tag{3.3.2a}$$

$$H_2(0)=Ch_2=\text{constant},\qquad H_2'(0)=0 \tag{3.3.2b}$$

$$F_2(0)=Cf_2=\text{constant},\qquad F_2'(0)=0 \tag{3.3.2c}$$

$$G_2(\infty)=0 \tag{3.3.2d}$$

(3.3.2a) must hold to ensure the flow is symmetrical about the vortex centerline. The constant in the first equation of (3.3.2b) is related to the value of second order vorticity at r=0. The second equation of (3.3.2b) ensures the second derivative at the origin has a finite value for symmetrical flow. The constant in the first equation of (3.3.2c) is related to the second order axial velocity on the vortex centerline, the second condition ensures the second derivative exists at the origin for a symmetrical flow. (3.3.2d) arises from the freestream velocity condition.

The following relations have to be satisfied in order for the quasi-similarity solutions to exist,

$$U_2(\tilde{z})=U_1^2(\tilde{z}) \tag{3.3.3a}$$

$$V_2(\tilde{z}) = \frac{1}{\sqrt{\tilde{z}}} \cdot U_1^2(\tilde{z}) \tag{3.3.3b}$$

$$P_2(\tilde{z}) = \beta \cdot U_1^2(\tilde{z}) \tag{3.3.3c}$$

$$\Psi_2(\tilde{z}) = 8\pi\beta \cdot U_1^2(\tilde{z}) \tag{3.3.3d}$$

There are two constants, Ch_2 and Cf_2, in this second order problem. Two conditions must be satisfied by the second order solution — the downstream independence of both the vortex circulation and the total drag of the wing. These conditions are represented mathematically by

$$\lim_{\eta\to\infty}\left[\eta^2 \cdot H_2(\eta)\right] = 0 \tag{3.3.4a}$$

$$\int_0^\infty \left[\beta_2 \cdot G_2(\eta) + F_2(\eta) + F_1^2(\eta)\right] \cdot \eta \cdot d\eta = 0 \tag{3.3.4b}$$

3.3.1 Second order tangential velocity and pressure

The non-singular solution of ODE (3.3.1b) with boundary condition (3.3.2b) is

$$H_2(\eta) = Ch_2 \cdot e^{-\frac{\eta^2}{4}} \tag{3.3.5}$$

The solution of (3.3.1c) therefore is

$$G_2(\eta) = Ch_2 \cdot \left[4Ei\left(1, \tfrac{\eta^2}{2}\right) - 4Ei\left(1, \tfrac{\eta^2}{4}\right)\right] \tag{3.3.6}$$

The tangential velocity component and pressure distribution are therefore

$$\upsilon_{\theta(2)}(z,r) = U_\infty \cdot \tilde{r} \cdot \tilde{\psi}_{(2)}(z,\eta) = U_\infty \cdot \tilde{r} \cdot 8\pi\beta \cdot U_1^2(z) \cdot H_2(\eta) \tag{3.3.7}$$

$$p_{(2)}(z,r) = \rho U_\infty^2 \cdot \beta \cdot U_1^2(z) \cdot G_2(\eta) \tag{3.3.8}$$

thus, $$\upsilon_{\theta(2)}(z,\eta) = \frac{Ch_2 \cdot \Gamma^3}{512\pi^3\beta \cdot U_\infty^{0.5} \cdot (\nu z)^{1.5}} \cdot \eta e^{-\frac{\eta^2}{4}} \tag{3.3.9}$$

$$p_{(2)}(z,r) = \frac{Ch_2 \cdot \rho\Gamma^4}{1024\pi^4\beta(\nu z)^2} \cdot \left[Ei\left(1, \tfrac{\eta^2}{2}\right) - Ei\left(1, \tfrac{\eta^2}{4}\right)\right] \tag{3.3.10}$$

Now let us consider the constraints (3.3.4a). Since

$$\lim_{\eta\to\infty}\left[\eta^2 \cdot H_2(\eta)\right] = Ch_2 \cdot \lim_{\eta\to\infty}\left(\eta^2 \cdot e^{-\frac{\eta^2}{4}}\right) = 0 \tag{3.3.11}$$

(3.3.4a) is satisfied without placing any constraint on the constant Ch_2. (3.3.4b) can be evaluated by integrating all the terms in (3.3.1d), yielding

$$\begin{aligned}&\int_0^\infty \left\{2\eta\cdot F_2''(\eta)+(\eta^2+2)\cdot F_2'(\eta)+4\eta\cdot F_2(\eta)\right\}\cdot d\eta\\&=\int_0^\infty\left\{-\beta\cdot\left[4\eta\cdot G_2(\eta)+2\eta^3\cdot H_1(\eta)\cdot H_2(\eta)\right]-2\eta F_1^2(\eta)\right\}\cdot d\eta\end{aligned}\tag{3.3.12}$$

Because

$$\begin{aligned}&\int_0^\infty(\eta^2+2)\cdot F_2'(\eta)\cdot d\eta=(\eta^2+2)\cdot F_2(\eta)\Big|_0^\infty-2\int_0^\infty F_2(\eta)\cdot\eta d\eta\\&=-2Cf_2-2\int_0^\infty F_2(\eta)\cdot\eta d\eta\end{aligned}\tag{3.3.13}$$

and

$$\begin{aligned}&\int_0^\infty 2\eta F_2''(\eta)\cdot d\eta=2\left\{\eta F_2'(\eta)\Big|_0^\infty-\int_0^\infty F_2'(\eta)\cdot d\eta\right\}\\&=-2\left\{F_2(\eta)\Big|_0^\infty\right\}=2Cf_2\end{aligned}\tag{3.3.14}$$

thus, (3.3.12) can be rewritten as

$$\begin{aligned}\int_0^\infty\left\{\eta\cdot F_2(\eta)+\eta F_1^2(\eta)\right\}\cdot d\eta&=-\frac{\beta}{2}\cdot\int_0^\infty\left\{2\eta\cdot G_2(\eta)+\left[\eta^2\cdot G_2(\eta)\right]'\right\}\cdot d\eta\\&=-\beta\int_0^\infty G_2(\eta)\eta\cdot d\eta\end{aligned}\tag{3.3.15}$$

That is

$$\int_0^\infty\left\{\beta\cdot G_2(\eta)+F_2(\eta)+F_1^2(\eta)\right\}\cdot\eta\cdot d\eta=0\tag{3.3.16}$$

(3.3.16) is exactly (3.3.4b). The equivalence implies that the second order drag equals zero, independent of the constants Ch_2 and Cf_2.

To determine these two constants, let us consider the physics behind the quasi-similarity method. The first order problem consists of the most important terms. Because the first order solutions include information on the vortex circulation and drag due to the vortex, they construct the first order approximation to the solution. The second order problem can be considered to be an ODE system with the lower order results as inputs. Higher order solutions are used to compensate for the non-linear terms (or higher order

terms with respect to the downstream distance) in the governing equation. For the second order ODE system, complementary functions, which are the solutions of the homogeneous equation, exist. The non-singular complementary functions of (3.3.1b) and (3.3.1d) are $Ch_2 \cdot e^{-\frac{\eta^2}{4}}$ and $Cf_2 \cdot (\eta^2 - 4) \cdot e^{-\frac{\eta^2}{4}}$ respectively. These solutions are unrelated to the circulation of the vortex and the wing total drag, and are also not functions of the lower order solutions as well. Physically, it is reasonable to select the constants Ch_2 and Cf_2 as zero so that only the part of the second order solution beyond the first order results remains:

$$Ch_2 = Cf_2 = 0 \tag{3.3.17}$$

The second order tangential velocity and pressure are thus,

$$\upsilon_{\theta(2)}(z,r) = 0 \tag{3.3.18}$$

$$p_{(2)}(z,r) = 0 \tag{3.3.19}$$

Therefore the first order tangential velocity and pressure are actually the second order approximation of the solution. In other words, the first order solution are accurate up to the third order, $O(U_1^3(z))$.

3.3.2 Second order axial and radial velocity components

The governing equations (3.3.1a) and (3.3.1d) can be rewritten as

$$2\eta R_2'(\eta) + 2R_2(\eta) = \eta^2 \cdot F_2'(\eta) + 4\eta \cdot F_2(\eta) \tag{3.3.20}$$

$$2\eta \cdot F_2''(\eta) + (\eta^2 + 2) \cdot F_2'(\eta) + 4\eta \cdot F_2(\eta) = -2\eta F_1^2(\eta) \tag{3.3.21}$$

The boundary conditions of this second order problem are

$$R_2(0) = 0 \tag{3.3.22}$$

$$F_2(0) = Cf_2 = 0, \qquad F_2'(0) = 0 \tag{3.3.23}$$

The axial and radial velocity components can be obtained numerically by the Runge-Kutta method. Notice that because F_1 is a function of the constant β, F_2 must be a function of β as well.

By using the Runge-Kutta method and the first order functions, one can obtain the second order functions for any value of β. The numerical results for the axial similarity function are shown in Figures 3.7 and 3.8. For all values of β, the second order axial similarity function is negative near η=0, whereas the second order axial amplitude function is always positive. Therefore, the first order solution underpredicts the axial velocity defect in the vortex core when β <0 (i.e. when the wing experiences a positive drag). For the case β >0 (a wing generating thrust), the first order solution overestimates the axial velocity excess in the vortex core.

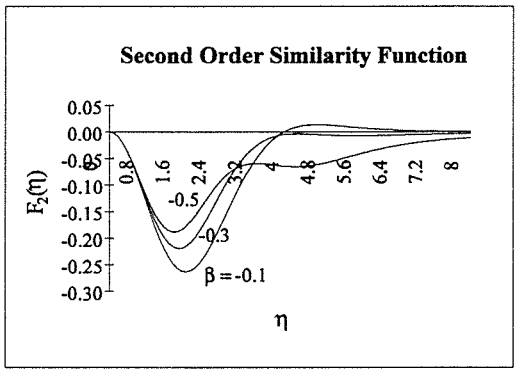

Figure 3.7 The second order axial quasi-similarity function. β <0

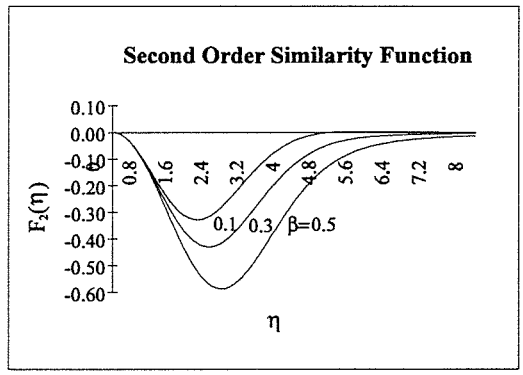

Figure 3.8 The second order axial quasi-similarity function. β >0

The second order radial similarity function can be expressed in terms of the axial similarity function,

$$R_2(\eta) = \frac{\eta}{2} F_2(\eta) + \frac{1}{\eta} \cdot \int_0^{\eta} F_2(x) \cdot x dx \qquad (3.3.24)$$

Numerical values of the radial similarity function for different values of β are plotted in Figures 3.9 and 3.10.

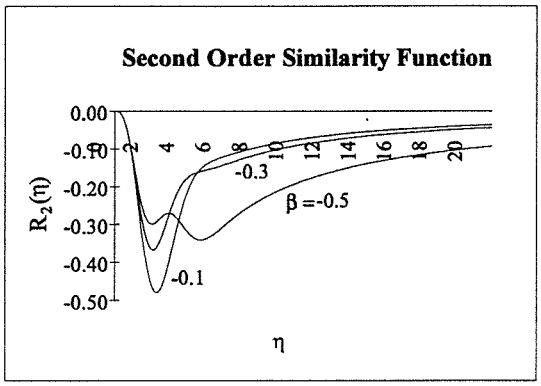

Figure 3.9 The second order radial quasi-similarity function. $\beta<0$

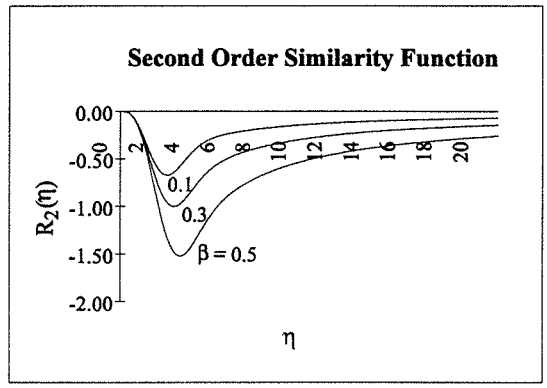

Figure 3.10 The second order radial quasi-similarity function. $\beta>0$

3.4 The procedure for i-th order solution ($i>2$)

The i-th order solution can be obtained by solving the following ODEs with the boundary conditions and constraints:

$$2\eta R_i' + 2R_i = \eta^2 \cdot F_i' + 2i \cdot \eta \cdot F_i \tag{3.4.1}$$

$$\begin{aligned} &2\eta H_i'' + (\eta^2+6)H_i' + 2i\eta H_i \\ &= \sum_{j=1}^{i-1}\left\{\left(2\eta H_{i-j}' + 4H_{i-j}\right)R_j - \left(\eta^2 H_{i-j}' + 2(i-j)\eta H_{i-j}\right)F_j\right\} \end{aligned} \tag{3.4.2}$$

$$G_i' = \eta \cdot \sum_{j=1}^{i}\left(H_j \cdot H_{i-j+1}\right) \tag{3.4.3}$$

$$\begin{aligned} &2\eta F_i'' + (\eta^2+2)F_i' + 2i\eta F_i = -\beta \cdot \left[2i\eta G_i + \eta^3 \sum_{j=1}^{i}\left(H_j \cdot H_{i-j+1}\right)\right] \\ &+ \sum_{j=1}^{i-1}\left\{2\eta R_j \cdot F_{i-j}' - \eta F_j \cdot \left[2(i-j)F_{i-j} + \eta F_{i-j}'\right]\right\} \end{aligned} \tag{3.4.4}$$

where β is the constant that was established in the first order problem solution.

Like the second order problem, the boundary conditions of this i-th order problem are

$$R_i(0) = 0 \tag{3.4.5}$$

$$H_i(0) = Ch_i = 0, \qquad H_i'(0) = 0 \tag{3.4.6}$$

$$F_i(0) = Cf_i = 0, \qquad F_i'(0) = 0 \tag{3.4.7}$$

$$G_i(\infty) = 0 \tag{3.4.8}$$

There are two conditions the i-th order solutions must satisfy — conservation of the vortex circulation and the independence of the wing total drag with the downstream distance. Respectively,

$$\lim_{\eta\to\infty}\left[\eta^2 \cdot H_i(\eta)\right] = 0 \tag{3.4.9}$$

and
$$\int_0^\infty \left[\beta_i \cdot G_i(\eta) + F_i(\eta) + \sum_{j=1}^{i-1} F_j(\eta)\cdot F_{i-j}(\eta)\right]\cdot \eta \cdot d\eta = 0 \tag{3.4.10}$$

Meanwhile, the following relations have to be satisfied if the quasi-similarity solutions exist,

$$U_i(\tilde{z}) = U_1^{\,i}(\tilde{z}) \tag{3.4.11}$$

$$V_i(\tilde{z}) = \frac{1}{\sqrt{\tilde{z}}}\cdot U_1^i(\tilde{z}) \tag{3.4.12}$$

$$P_i(\tilde{z}) = \beta \cdot U_1^i(\tilde{z}) \tag{3.4.13}$$

$$\Psi_i(\tilde{z}) = 8\pi\beta \cdot U_1^i(\tilde{z}) \tag{3.4.14}$$

The following procedure could be used to solve these coupled ordinary differential equations. Suppose that the lower order (less than i-th order) solutions have been obtained. Then the i-th order problem can be calculated numerically by solving ODEs (3.4.1)-(3.4.4) with the boundary conditions (3.4.5)-(3.4.8) to find R_i, F_i, H_i, and G_i. In summary, the i-th order results can be expressed as

$$\upsilon_{z(i)}(z,r) = U_\infty \cdot U_1^i(z)\cdot F_i(\eta) \tag{3.4.15}$$

$$\upsilon_{\theta(i)}(z,r) = U_\infty \cdot \tilde{r}\cdot \tilde{\psi}_{(i)}(z,r) = \frac{8\pi\sqrt{U_\infty^3 \cdot \nu z}}{\Gamma}\cdot \beta \cdot U_1^i(z)\cdot \eta H_i(\eta) \tag{3.4.16}$$

$$\upsilon_{r(i)}(z,r) = \sqrt{\frac{U_\infty \cdot \nu}{z}}\cdot U_1^i(z)\cdot R_i(\eta) \tag{3.4.17}$$

$$p_{(i)}(z,r) = \rho U_\infty^2 \cdot \beta \cdot U_1^i(z)\cdot G_i(\eta) \tag{3.4.18}$$

where
$$U_1(z) = \frac{1}{64\pi^2\beta}\cdot\frac{\Gamma^2}{U_\infty \cdot \nu \cdot z}$$

3.4.1 Conservation of the vortex circulation Γ

We have assumed in section 3.1 of Chapter 2 that, in order to conserve the vortex circulation, the following equation must hold,

$$\left[\eta^2 H_i(\eta)\right]_{\eta\to\infty} = 0, \qquad (i \geq 2) \tag{3.4.19}$$

Now we will verify that this relation does hold for the higher order problem. According to the results of the first order problem, the following asymptotic characteristics can be found,

$$H_1(\eta) \xrightarrow{\eta\to\infty} \frac{1}{\eta^2} \tag{3.4.20a}$$

$$G_1(\eta) \xrightarrow{\eta\to\infty} \frac{1}{\eta^2} \tag{3.4.20b}$$

$$F_1(\eta) \xrightarrow{\eta\to\infty} \frac{1}{\eta^2} \tag{3.4.20c}$$

$$R_1(\eta) \xrightarrow{\eta\to\infty} \frac{1}{\eta} \tag{3.4.20d}$$

Based on the ODEs governing the high order problems, one can prove by mathematical induction the proposition that the asymptotic results for the i-th order problem are

$$H_i(\eta) \xrightarrow{\eta\to\infty} \frac{1}{\eta^{2i}} \tag{3.4.21a}$$

$$G_i(\eta) \xrightarrow{\eta\to\infty} \frac{1}{\eta^{2i}} \tag{3.4.21b}$$

$$F_i(\eta) \xrightarrow{\eta\to\infty} \frac{1}{\eta^{2i}} \tag{3.4.21c}$$

$$R_i(\eta) \xrightarrow{\eta\to\infty} \frac{1}{\eta^{2i-1}} \tag{3.4.21d}$$

We begin our proof by checking the first order problem (3.4.20). Obviously the proposition (3.4.21) is correct when i=1.

Next, we assume the proposition is correct for $i=l$, $l\leq k$. This assumption means that for the l-th order problem,

$$H_l(\eta) \xrightarrow{\eta\to\infty} \frac{1}{\eta^{2l}} \tag{3.4.22a}$$

$$G_l(\eta) \xrightarrow{\eta\to\infty} \frac{1}{\eta^{2l}} \tag{3.4.22b}$$

$$F_l(\eta) \xrightarrow{\eta\to\infty} \frac{1}{\eta^{2l}} \tag{3.4.22c}$$

$$R_l(\eta) \xrightarrow{\eta\to\infty} \frac{1}{\eta^{2l-1}} \tag{3.4.22d}$$

Now, we prove the proposition is correct for i=k+1. We are going to use L'Hopital's Rule in our proof. For an arbitrary function $f(\eta)$, if $\lim_{\eta\to\infty} f(\eta)=0$ and $\lim_{\eta\to\infty} f'(\eta)=0$, then one has,

$$\lim_{\eta\to\infty}\frac{f(\eta)}{\eta^{-1}} = -\lim_{\eta\to\infty}\frac{f'(\eta)}{\eta^{-2}} = \frac{1}{2}\cdot\lim_{\eta\to\infty}\frac{f''(\eta)}{\eta^{-3}} \tag{3.4.23}$$

provided these limits exist or are +∞ or -∞ (Barnett and Ziegler 1991). The above relation can be rearranged as

$$\lim_{\eta\to\infty}\eta^2\cdot f'(\eta) = -\lim_{\eta\to\infty}\eta\cdot f(\eta) \tag{3.4.24}$$

$$\lim_{\eta\to\infty}\eta^3\cdot f''(\eta) = 2\cdot\lim_{\eta\to\infty}\eta\cdot f(\eta) \tag{3.4.25}$$

Replacing i with k+1 in equation (3.4.2) and taking the limit on both sides, one can obtain the following equation using (3.4.22a-d):

$$\lim_{\eta\to\infty}\left[2\eta H''_{k+1}\right]+\lim_{\eta\to\infty}\left[\left(\eta^2+6\right)H'_{k+1}\right]+2(k+1)\cdot\lim_{\eta\to\infty}\left[\eta H_{k+1}\right]\to\frac{1}{\eta^{2(k+1-j)}}\cdot\frac{1}{\eta^{2j-1}} \tag{3.4.26}$$

The value 6 is small compared with η^2 when η approaches infinity, and based on (3.4.25) $\eta\cdot H''_{k+1}$ is much smaller than $\eta\cdot H_{k+1}$ at large η. Therefore, (3.4.26) can be rewritten as

$$\lim_{\eta\to\infty}\eta H_{k+1}(\eta)\to\frac{1}{\eta^{2k+1}}$$

or

$$H_{k+1}(\eta) \xrightarrow{\eta\to\infty} \frac{1}{\eta^{2(k+1)}} \tag{3.4.27}$$

Similarly, replacing i in (3.4.3) with (k+1), multiplying by η^2 on both sides, and taking the limit yields

$$\lim_{\eta\to\infty}\left[\eta^2\cdot G'_{k+1}(\eta)\right]\to\eta^3\cdot\frac{1}{\eta^{2j}}\cdot\frac{1}{\eta^{2(k+1-j+1)}}$$

or $$\lim_{\eta\to\infty}\left[\eta\cdot G'_{k+1}(\eta)\right]\to\frac{1}{\eta^{2k+1}}$$

Therefore,

$$G_{k+1}(\eta)\xrightarrow{\eta\to\infty}\frac{1}{\eta^{2(k+1)}} \tag{3.4.28}$$

We can do the same thing to equation (3.4.4) as we did to equation (3.4.2):

$$\lim_{\eta\to\infty}\left[2\eta F''_{k+1}\right]+\lim_{\eta\to\infty}\left[\left(\eta^2+2\right)F'_{k+!}\right]+2(k+1)\cdot\lim_{\eta\to\infty}\left[\eta F_{k+1}\right]\to\eta\frac{1}{\eta^{2j}}\cdot\frac{1}{\eta^{2(k+1-j)}} \tag{3.4.29}$$

The first term on the left side of the above equation is much less than the third term. The value 2 in the second term can be neglected compared with η^2 at large η. Consequently, (3.4.28) can be rewritten as

$$\lim_{\eta\to\infty}\eta F_{k+1}\to\frac{1}{\eta^{2k+1}}$$

or $$F_{k+1}(\eta)\xrightarrow{\eta\to\infty}\frac{1}{\eta^{2(k+1)}} \tag{3.4.30}$$

(3.4.1), along with boundary condition (3.4.5), can be solved. The solution is

$$2\eta R_i(\eta)=\eta^2\cdot F_i(\eta)+2(i-1)\int_0^\eta xF_i(x)\cdot dx \tag{3.4.31}$$

Replacing i with k+1 in the above equation, and dividing by 2η on both sides, yields

$$R_{k+1}(\eta)=\frac{\eta}{2}F_{k+1}(\eta)+\frac{k}{\eta}\int_0^\eta xF_{k+!}(x)\cdot dx \tag{3.4.32}$$

Taking the limit on both sides of the above equation, one has

$$\lim_{\eta\to\infty}R_{k+1}(\eta)=\lim_{\eta\to\infty}\left[\tfrac{\eta}{2}F_{k+1}(\eta)\right]+k\cdot\lim_{\eta\to\infty}\left[\eta F_{k+1}(\eta)\right] \tag{3.4.33}$$

Therefore,

$$R_{k+1}(\eta)\xrightarrow{\eta\to\infty}\frac{1}{\eta^{2(k+1)-1}} \tag{3.4.34}$$

We have therefore proved that the proposition is correct for k+1, provided that it is correct for $i=l$, $l\le k$. Since the proposition is correct for i=1, this concludes the proof by mathematical induction. Hence*

* The second order tangential equation happened to be a homogeneous ODE. Therefore the second order similarity functions described by (3.3.5) and (3.3.6) are different from that described by (3.4.21a-b). The

$$\left[\eta^2 \cdot H_i(\eta)\right] \xrightarrow{\eta\to\infty} \left.\frac{1}{\eta^{2(i-1)}}\right|_{\eta\to\infty} \equiv 0, \quad \text{for} \qquad i \geq 2$$

Thus, we have verified that

$$\left[\eta^2 H_i(\eta)\right]_{\eta\to\infty} = 0 \qquad (i \geq 2)$$

3.4.2 The i-th order drag

In this sub-section, we will prove that the i-th order solutions satisfy the condition that the higher order drag is zero.

Integrating the axial momentum equation from zero to infinity, yields

$$\begin{aligned}\int_0^\infty \left\{2\eta F_i'' + (\eta^2+2)F_i' + 2i\eta F_i\right\}\cdot d\eta &= -\beta \cdot \int_0^\infty \left[2i\eta G_i + \eta^3 \sum_{j=1}^{i}\left(H_j \cdot H_{i-j+1}\right)\right]\cdot d\eta \\ &+ \sum_{j=1}^{i-1}\int_0^\infty \left\{2\eta R_j \cdot F_{i-j}' - \eta F_j \cdot \left[2(i-j)F_{i-j} + \eta F_{i-j}'\right]\right\}\cdot d\eta\end{aligned} \tag{3.4.35}$$

Because

$$\begin{aligned}\int_0^\infty 2\eta F_i''(\eta)\cdot d\eta &= 2\left\{\eta F_i'(\eta)\Big|_0^\infty - \int_0^\infty F_i(\eta)\cdot d\eta\right\} \\ &= -2\left\{F_i(\eta)\Big|_0^\infty\right\} \\ &= 2Cf_i\end{aligned} \tag{3.4.36}$$

and

$$\begin{aligned}\int_0^\infty (\eta^2+2)F_i'(\eta)\cdot d\eta &= (\eta^2+2)\cdot F_i(\eta)\Big|_0^\infty - 2\int_0^\infty F_i(\eta)\cdot \eta d\eta \\ &= -2Cf_i - 2\int_0^\infty F_i(\eta)\cdot \eta d\eta\end{aligned} \tag{3.4.37}$$

the left side of the equation (3.4.35) is thus,

$$\int_0^\infty \left\{2\eta F_i'' + (\eta^2+2)F_i' + 2i\eta F_i\right\}\cdot d\eta = 2(i-1)\cdot \int_0^\infty F_i(\eta)\cdot \eta d\eta \tag{3.4.38}$$

Furthermore

---

difference does not affect the validity of the assumption, it only hastens the approach of the similarity functions to zero as the similarity variable approaches infinity.

$$-\beta\cdot\int_0^\infty\left[2i\eta G_i+\eta^3\sum_{j=1}^{i}\left(H_j\cdot H_{i-j+1}\right)\right]\cdot d\eta=-\beta\cdot\int_0^\infty\left\{2(i-1)\eta G_i+\left[\eta^2G_i(\eta)\right]'\right\}\cdot d\eta$$
$$=-\beta\cdot\left\{\int_0^\infty 2(i-1)\cdot G_i(\eta)\cdot\eta d\eta+\left[\eta^2G_i(\eta)\right]\Big|_0^\infty\right\} \tag{3.4.39}$$

For the higher order problem ($i\geq 2$), $\left[\eta^2G_i(\eta)\right]\Big|_0^\infty=0$. Therefore

$$-\beta\cdot\int_0^\infty\left[2i\eta G_i+\eta^3\sum_{j=1}^{i}\left(H_j\cdot H_{i-j+1}\right)\right]\cdot d\eta=-2(i-1)\beta\cdot\int_0^\infty G_i(\eta)\cdot\eta d\eta \tag{3.4.40}$$

Now, consider the last term in equation (3.4.35). We can replace R_i with F_i based on the continuity equation (3.4.1). (3.4.1) can be rewritten as

$$2\left[\eta R_i(\eta)\right]'=\left[\eta^2F_i(\eta)\right]'+2(i-1)\eta F_i(\eta)$$

or
$$2\eta R_i(\eta)=\eta^2F_i(\eta)+2(i-1)\int_0^\eta xF_i(x)dx \tag{3.4.41}$$

Thus,

$$\sum_{j=1}^{i-1}\int_0^\infty\left\{2\eta R_j\cdot F'_{i-j}-\eta F_j\cdot\left[2(i-j)F_{i-j}+\eta F'_{i-j}\right]\right\}\cdot d\eta$$
$$=\sum_{j=1}^{i-1}\int_0^\infty\left\{2(j-1)\cdot F'_{i-j}\cdot\int_0^\eta xF_i\cdot dx-2(i-j)\eta F_jF_{i-j}\right\}\cdot d\eta$$
$$=\sum_{j=1}^{i-1}\left\{2(j-1)\cdot\int_0^\infty\eta F_iF_{i-j}\cdot d\eta-2(i-j)\int_0^\infty\eta F_jF_{i-j}\cdot d\eta\right\} \tag{3.4.42}$$
$$=-2(i-1)\sum_{j=1}^{i-1}\int_0^\infty\eta F_jF_{i-j}\cdot d\eta$$

Substitution of (3.4.38), (3.4.40) and (3.4.42) into (3.4.35), yields

$$2(i-1)\left\{\int_0^\infty\left[\beta\cdot G_i(\eta)+F_i(\eta)+\sum_{j=1}^{i-1}F_j(\eta)\cdot F_{i-j}(\eta)\right]\cdot\eta d\eta\right\}=0 \tag{3.4.43}$$

For the higher order problem ($i\geq 2$)

$$\int_0^\infty\left[\beta\cdot G_i(\eta)+F_i(\eta)+\sum_{j=1}^{i-1}F_j(\eta)\cdot F_{i-j}(\eta)\right]\cdot\eta d\eta\equiv 0,\quad i\geq 2 \tag{3.4.44}$$

This result means that the higher order solutions satisfy the requirement that the wing total drag is independent of the downstream distance because the higher order drags are all zero.

3.5 The axial velocity on the vortex centerline

The axial velocity on the vortex centerline is

$$\upsilon_z(z,0) = U_\infty \cdot [1 + U_1(z)] = U_\infty \cdot \left[1 - \frac{D_w}{8\pi\rho\nu z U_\infty}\right] \tag{3.5.1}$$

since $F_i(0)=0$ for $i \geq 2$. The result given by (3.5.1) is valid provided

$$|U_1(z)| = \left|\frac{D_w}{8\pi\rho\nu z \cdot U_\infty}\right| < 1 \tag{3.5.2}$$

where D_w is the wing total drag, U_∞ is the freestream velocity, z is the downstream distance from the wing tip, ρ is the density, and ν is the laminar kinematic viscosity. The axial velocity component on the tip vortex centerline can be evaluated by using (3.5.1) if the wing total drag is known. The axial velocity deficit on the vortex centerline is proportional to the wing total drag, and inversely proportional to the downstream distance. At a cursory glance it would appear that the axial velocity is not related to the circulation of the wing tip vortices. This impression is not correct. The total drag of the wing is the sum of the friction drag and the tip vortex induced drag, and because the induced drag is a function of the wing circulation, so too is the vortex axial veloctiy.

3.6 Comparison with Batchelor's vortex

Batchelor (1964) made a first effort to solve the wing tip vortex flow analytically. Batchelor's analysis involves a linearization of the governing equations. Is there any connection between Batchelor's vortex and the first order quasi-similarity solutions? As we shall see, the tangential velocity component and pressure distribution in Batchelor's vortex are exactly the same as our first order tangential velocity and pressure, because the

ODEs and boundary conditions for the tangential velocity and pressure are the same for both models. In contrast, the axial velocity is different between the two models. The axial velocity field of Batchelor's vortex results in a single vortex with an infinite drag. Batchelor resolves this problem by invoking the (somewhat artificial) concept of a "drag associated with the vortex core of a trailing vortex." There is no equivalent limitation in the quasi-similar solutions; the axial velocity distribution does not lead to infinite values of drag. The limitation on our quasi-similarity method is $|U_1(z)| < 1$, which is a significant improvement over Batchelor's vortex, for which the constraint is equivalent to $\left|\frac{U_\infty - \upsilon_z(z,r)}{U_\infty}\right| \sim |U_1(z)| << 1$.

A summary of the procedure Batchelor used to obtain his similarity solution, along with commentary, follows.

Far downstream, where the boundary-layer-type approximations (assumptions (3) and (4) in section 2 of Chapter 2) are supplemented by the approximation

$$|U_\infty - \upsilon_z| << U_\infty \tag{3.6.1}$$

the governing equations (2.2.5)-(2.2.8) reduce to

$$\frac{1}{r}\cdot\frac{\partial(r\upsilon_r)}{\partial r} + \frac{\partial \upsilon_z}{\partial z} = 0 \tag{3.6.2a}$$

$$U_\infty \cdot \frac{\partial \upsilon_\theta}{\partial z} = \nu \cdot \left(\frac{\partial^2 \upsilon_\theta}{\partial r^2} + \frac{1}{r}\frac{\partial \upsilon_\theta}{\partial r} - \frac{\upsilon_\theta}{r^2}\right) \tag{3.6.2b}$$

$$\frac{\upsilon_\theta^2}{r} = \frac{1}{\rho}\frac{\partial p}{\partial r} \tag{3.6.2c}$$

$$U_\infty \cdot \frac{\partial \upsilon_z}{\partial z} = -\frac{\partial p}{\partial z} + \nu \cdot \left(\frac{\partial^2 \upsilon_z}{\partial r^2} + \frac{1}{r}\frac{\partial \upsilon_z}{\partial r}\right) \tag{3.6.2d}$$

Batchelor solved the tangential and radial momentum equations by similarity methods. The tangential velocity and pressure obtained by him are found to be exactly the same as our first order solutions.

Batchelor found

$$\upsilon_\theta = \frac{\Gamma}{2\pi r}\left(1 - e^{-\xi}\right) \tag{3.6.3}$$

$$p - p_\infty = -\frac{\rho U_\infty \cdot \Gamma^2}{32\pi^2 \nu z} \cdot P_p(\xi), \quad P_p(\xi) = \left\{ \frac{\left(1 - e^{-\xi}\right)^2}{\xi} + 2ei(\xi) - 2ei(2\xi) \right\} \tag{3.6.4}$$

where the similarity variable $\xi = \frac{U_\infty r^2}{4\nu z} = \frac{\eta^2}{4}$, and the function $ei(\xi) = \int_\xi^\infty \left\{ \frac{e^{-y}}{y} \right\} \cdot dy$. It is not difficult to show that (3.6.3) and (3.6.4) are the same as the first order quasi-similar solutions. The axial momentum equation (3.6.2d) now becomes

$$U_\infty \cdot \frac{\partial \upsilon_z}{\partial z} - \nu \cdot \left(\frac{\partial^2 \upsilon_z}{\partial r^2} + \frac{1}{r} \frac{\partial \upsilon_z}{\partial r} \right) = -\frac{U_\infty \cdot \Gamma^2}{32\pi^2 \nu z^2} \left[P_p(\xi) + \xi \frac{dP_p(\xi)}{d\xi} \right] \tag{3.6.5}$$

In order to obtain a clearer view of the asymptotic dependence of υ_z on z, all the terms of above equation were integrated over a cross-sectional plane:

$$\begin{aligned} \frac{d}{dz} \int_0^\infty (U_\infty - \upsilon_z) \cdot r dr &= \frac{\Gamma^2}{16\pi^2 U_\infty z} \int_0^\infty \frac{d(\xi P_p)}{d\xi} d\xi \\ &= \frac{\Gamma^2}{16\pi^2 U_\infty \cdot z} \end{aligned} \tag{3.6.6}$$

since $P_p \sim \xi^{-1}$ as $\xi \to \infty$. Thus

$$\int_0^\infty (U_\infty - \upsilon_z) \cdot r dr = \frac{\Gamma^2}{16\pi^2 U_\infty} \cdot \log \frac{z U_\infty}{\nu} + \text{const.} \tag{3.6.7}$$

where ν / U_∞ has been used as a convenient unit of length in the logarithm.

The relation (3.6.7) suggests the following form for an asymptotic solution of the axial momentum equation:

$$\upsilon_z = U_\infty - \frac{\Gamma^2}{32\pi^2 \nu z} \cdot \log \frac{z U_\infty}{\nu} Q_1(\xi) + \frac{\Gamma^2}{32\pi^2 \nu z} \cdot Q_2(\xi) - L \frac{U_\infty^2}{8\nu z} e^{-\xi} \tag{3.6.8}$$

where L is a constant with the dimensions of area, and the last term, the complementary function, accounts for any initial velocity defect that may be independent of the circulation. The similarity functions Q_1 and Q_2 can be obtained and expressed as

$$Q_1(\xi) = e^{-\xi} \tag{3.6.9}$$

$$Q_2(\xi) = e^{-\xi} \int_0^\xi \left[\frac{1 - e^\xi}{\xi} + P_p(\xi) \cdot e^\xi \right] \cdot d\xi \tag{3.6.10}$$

The axial velocity given by (3.6.8) is obviously different from our first order axial velocity.

Now, let us consider the drag on the wing:

$$\frac{D}{\rho}=\int_0^\infty\left\{\frac{p_\infty-p}{\rho}+\upsilon_z(U_\infty-\upsilon_z)\right\}\cdot 2\pi r dr \tag{3.6.11}$$

Batchelor found that the integral of (3.6.11) is logarithmically divergent as $r\to\infty$, and therefore that the drag associated with his isolated trailing vortex is infinite. Batchelor argued that the divergence does not dependent on the structure of the core of the trailing vortex, and on this basis he defined the "drag associated with the core of a trailing vortex" as

$$\frac{D_c}{\rho}=\lim_{R\to\infty}\left[2\pi\int_0^R\left\{\frac{p_\infty-p}{\rho}+\upsilon_z(U_\infty-\upsilon_z)\right\}\cdot r dr-\frac{\Gamma^2}{4\pi}\cdot\log\frac{RU_\infty}{\nu}\right] \tag{3.6.12}$$

D_c differs from half the total drag on the wing by an amount that depends only on Γ and the distance between the two trailing vortices far downstream. In the case of two trailing vortices a distance s apart far downstream, it may be shown quite readily, from an evaluation of the kinetic energy of the motion in the lateral plane, that the total drag D_w is

$$D_w=2D_c+\frac{\rho\Gamma^2}{2\pi}\log\frac{sU_\infty}{\nu} \tag{3.6.13}$$

Substituting the pressure and axial velocity solutions ((3.6.3) and (3.6.4)) into (3.6.12), Batchelor found

$$\frac{D_c}{\rho}=-\frac{\lambda\Gamma^2}{8\pi}+\frac{\pi}{2}\cdot L\cdot U_\infty^2 \tag{3.6.14}$$

where λ is a positive number not far from unity. The solution (3.6.8) can now be rewritten as

$$\upsilon_z=U_\infty-\frac{1}{8\nu z}e^{-\xi}\left\{\frac{2}{\pi}\frac{D_c}{\rho}+\frac{\Gamma^2}{4\pi^2}\left(\lambda+\log\frac{zU_\infty}{\nu}\right)\right\}+\frac{\Gamma^2}{32\pi^2\nu z}Q_2(\xi) \tag{3.6.15}$$

If the trailing vortex system from a wing on which the total drag D_w consists of two vortices with centres a distance s apart, the axial velocity can be written in the further alternative form

$$\upsilon_z = U_\infty - \frac{1}{8\nu z} e^{-\xi} \left\{ \frac{1}{\pi} \frac{D_w}{\rho} + \frac{\Gamma^2}{4\pi^2} \left(\lambda + \log \frac{zU_\infty}{\nu} - 2 \log \frac{sU_\infty}{\nu} \right) \right\} + \frac{\Gamma^2}{32\pi^2 \nu z} Q_2(\xi) \qquad (3.6.16)$$

In summary, Batchelor's linearized analysis yields the same tangential velocity and pressure distribution as our first order quasi-similarity solution. Batchelor's vortex has an axial velocity distribution that results in a single vortex with an infinite drag, a problem that Batchelor resolves by defining the "drag associated with the vortex core." Our axial velocity distribution is different from Batchelor's and does not have infinite drag. Batchelor's analysis is limited to $\left|\frac{U_\infty - \upsilon_z}{U_\infty}\right| << 1$; by way of contrast, our analysis has the less restrictive limitation $\left|\frac{U_\infty - \upsilon_z}{U_\infty}\right| \sim \left|U_1(z)\right| < 1$.

3.7 Comparison with experimental data

3.7.1 Axial velocity decay on the vortex centerline

The axial velocity defect in the cores of trailing vortices behind a lifting airfoil of rectangular planform was measured using a scanning laser Doppler velocimeter (Ciffone and Orloff, 1974). Data were obtained at several different angles of attack and downstream distances ranging from 30 to 1000 chord lengths. The experiments were performed in a water tow-tank facility 61m long, 2.44m wide, and 1.7m deep. The test Reynolds number based on the wing chord was nominally 2.43×10^5. The wing used has an NACA 0015 airfoil section, an aspect ratio of 5.33, and a span of 0.61m. The test was designed to obtain continuous data from the near field to the far field by the hydrogen bubble technique.

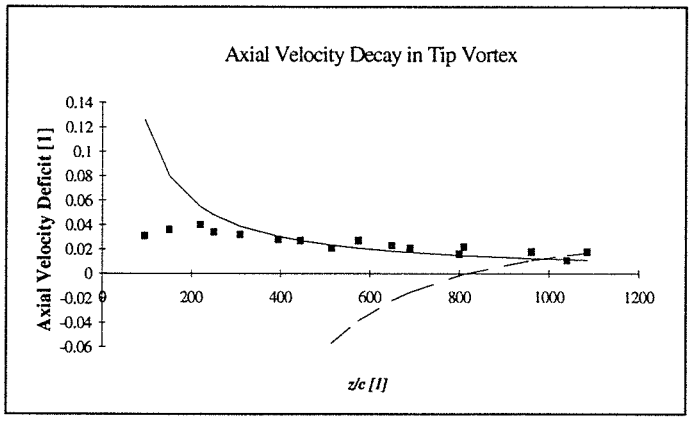

Figure 3.11 Axial velocity decay with downstream distance in a wing tip vortex. (The square symbols represent the experimental data, the solid line is the quasi-similar result and the dashed line is Batchelor's result)

The axial velocity defect data at 4° angle of attack are selected for comparison. Good agreement between the quasi-similarity theory and the experimental results occurs for $z/c > 300$ (Figure 3.11)* . This agreement was achieved by using a laminar viscosity ν and a drag coefficient, $C_D = 0.0005$. This drag coefficient is about twenty times smaller than a typical aircraft drag coefficient of $C_D = 0.01$.

There is a plausible explanation for the unreasonably low drag coefficient. The flow in a real wing tip vortex is probably turbulent. If one can model the effects of turbulence by means of an eddy viscosity ν_T that is constant spatially, then the quasi-similarity solution is still valid provided ν is replaced by ν_T. Modeling the flow of Figure 3.11 in this way, but enforcing the constraint $C_D = 0.01$, one determines $\nu_T \approx 20\nu$. Although no measurements of turbulent Reynolds stresses have ever been made in the far field of a tip vortex, a turbulent eddy viscosity twenty times the laminar viscosity is typical of many flows. Thus, although the quasi-similarity theory has effectively a free constant, which has been used here to match the theory with the experimental results, the constant (related to the drag coefficient) selected to give good agreement with experiment is reasonable.

Batchelor's theory gives much poorer agreement with the axial velocity results (Figure 3.11) at these small downstream distances owing to the logarithmic terms in (3.6.16). At <u>very</u> far downstream distances Batchelor's theory and the quasi-similar theory show the same dependence of axial velocity deficit on the downstream distance z because $\lim_{z\to\infty}(\log z)/z = \lim_{z\to\infty} 1/z$.

3.7.2 Maximum tangential velocity decay

A study of aircraft trailing vortex system, involving actual flight testing, was reported by McCormick et al.(1968). Detailed velocity measurements were made through the vortex immediately behind a test aircraft up to a distance of approximately 1000 chord lengths downstream of the aircraft. Flight testing was performed using a U.S. Army 0-1 aircraft and a Piper Cherokee. Measurement of the trailing vortices of each aircraft was

* The disagreement for $z/c < 300$ may be caused by varying eddy viscosity in the tip vortex near field and the limitations of the theory itself.

made using a vortimeter and a tuft grid. The vortimeter consisted of a vertical array of 30, 1-ft-long, 1/4-in.-diam cylinders. Each cylinder was supported on strain-gaged flexures so that the aerodynamic drag on each cylinder could be measured. Hence, the velocity distribution through the vortex could be determined as the vortex moves through the array, by measuring the forces acting on each cylinder as a function of time.

Velocity distributions through the trailing vortices shed by the 0-1 and Cherokee aircraft at several flight speeds were measured. The non-dimensional data are compared with our analytical results in Figure 3.12. For $z/c < 200$ the agreement is poor, likely because of turbulent flow in the tip vortex. In contrast, the agreement far downstream, $z/c > 200$, is satisfactory. This agreement confirms that the maximum tangential velocity decays as one over the square root of the downstream distance — one of the results predicted by the quasi-similarity method.

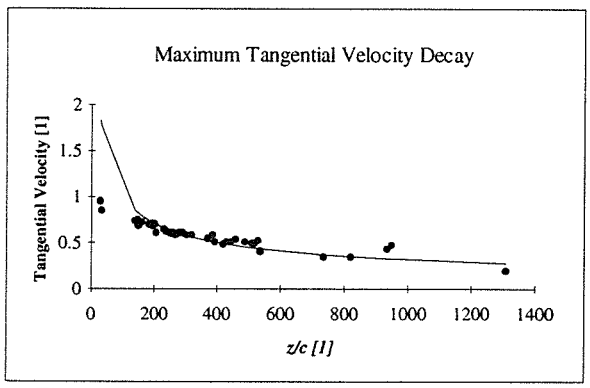

Figure 3.12 Maximum tangential velocity decay with downstream distance in a wing tip vortex. (The round symbols represent the experimental data, the solid line is the analytical result)

3.8 Conclusions

There are two major practical limitations on the quasi-similarity solution. One is the assumption that the axial velocity deficit or excess must not be significantly greater than the freestream velocity. Very near the wing this condition may not apply. The quasi-similarity method is limited as well by the assumption that the flow must be laminar.

The limitation on the quasi-similarity solution from the convergence requirement (2.7.3) can be rewritten (assuming a rectangular wing) as

$$z > \frac{C_D \cdot \mathrm{Re}_c \cdot S}{16\pi} \tag{3.8.1}$$

where C_D is the drag coefficient, Re_c is the Reynolds number based on the chord, and S is the span of the wing. This distance is about a hundred meters downstream of the wing

trailing edge for a typical drag coefficient $C_D \approx 0.01$, Reynolds number $\mathrm{Re}_c \approx 5\times10^5$, and a one meter span wing (for which the flow should be laminar). We can also make the following specific conclusions:

1. The quasi-similarity method represents an improvement over the solution of Batchelor. The limitation on the quasi-similarity method is $|U_1(z)|<1$, instead of $|U_\infty - \upsilon_z|/U_\infty << 1$ as required by Batchelor. Thus, the quasi-similarity method can be used in trailing vortices comparatively close to the wing.
2. The tangential velocity component and pressure in the Batchelor's vortex are the same as the first order quasi-similarity solution. The axial velocity field of Batchelor's vortex differs from the quasi-similarity vortex. Batchelor's vortex has an infinite drag due to a single vortex whereas a quasi-similar vortex has a finite drag due to a single vortex.
3. The first order tangential velocity and pressure distribution have the third order accuracy, $\mathrm{O}(U_1^3(z))$. That might explain why Batchelor's theory is a good model of the tangential velocity even at fairly short distances downstream of a wing.
4. The maximum tangential velocity results have been compared with experimental data. The agreement is satisfactory far downstream. The agreement confirms that the tangential velocity decays as one over the square root of the downstream distance, as predicted by the theory.
5. The axial velocity predictions on the vortex centerline has been compared with measurements. The agreement is good far downstream, which confirms that the axial velocity deficit on the vortex centerline decays as one over the downstream distance.
6. There are two main restrictions on the quasi-similarity method. One is the laminar flow assumption. The other is that quasi-similar solutions are only valid at fairly large downstream distances.

Chapter 4 Cavitation and Aerodynamic Performance of the Ducted-Tip Wing

A novel hydrofoil design, consisting of a small diameter flow-through duct affixed to the tip, has been studied. The tip vortex cavitation inception index, σ_i, of this hydrofoil geometry is about a factor of 2 lower than that of a conventional rounded hydrofoil tip. This inception improvement comes with little associated performance penalty. For angles of attack greater than 8° the non-cavitating lift-drag ratio is actually superior to that of an unducted hydrofoil of equal span, although with lower wing loadings the hydrofoil performance is diminished by application of the ducted-tip.

The ducted tip is effective at reducing the tip vortex inception index because, in contrast with the rounded tip for which shed vorticity in the transverse plane behind the wing (Trefftz plane) is confined to a line, the ducted tip shed vorticity at the trailing edge is distributed over a line and circle. Distributing the vorticity in this fashion causes the trailing vortex to roll up less tightly, and hence have a higher core pressure and lower σ_i, than a conventional hydrofoil tip. It is also suspected that the interaction at the microscale level between the flow through the duct, and the flow around it, makes the vortex core size larger, and therefore σ_i smaller. The superior lift performance of the ducted-tip wing at elevated angles of attack results from the redistribution of the shed vorticity as well. The downwash caused by the vorticity on one portion of the ring tip in the Trefftz plane is smaller than that by the same amount of vorticity positioned in the spanwise direction. Less downwash produces less induced drag. At small angles of attack the benefit from the ducted tip device of reducing the induced drag is more than offset by the increased parasite drag due its larger wetted area. The ducted tip design has many potential marine applications, including to ship and submarine propellers, submarine control fins, and ship rudders.

The following section reviews the previous work on tip modifications. The second section explains the rationale for the novel ducted tip geometry. The third section describes the experimental apparatus and procedures. Flow visualization, cavitation characteristics and aerodynamic performance of the ducted tip configuration are presented

and discussed in section four. The experimental uncertainties are estimated in section five. Finally, conclusions are presented in section six.

4.1 Previous Work on Tip Modifications

The purposes of tip modification can be grouped into three categories: attenuating vortex strength to alleviate the rolling moment on a following aircraft, reducing the vortex induced drag, and increasing the vortex core pressure to avoid cavitation.

Various kinds of tip devices have been tested to reduce the rolling moment. A leading edge disk flow spoiler, a trailing edge disk flow spoiler and a porous wing-span extension were investigated by Scheiman and Shivers (1971). They achieved vortex cross-sectional redistribution at the expense of wing lift and/or drag characteristics. "Vortex-attenuating splines" were tested by Hastings et al. (1975) and found to cause a considerable noise increase and a lift/drag ratio reduction. Snedeker (1972) measured the rolling moment on a simulated following aircraft caused by a tip vortex with and without axial injection (injection of fluid in the chordwise direction from the wing tip). He found that the injection reduced the rolling moment by only 13% (for vortex generating wings at α = 6°). The applicability of such a scheme to commercial aircraft is dubious. The Whitcomb wing tip (Whitcomb 1976 and Flechner et al. 1976) is the only wing tip modification device that has found commercial application. This wing tip consists of a short (about 1/2 chord high) lifting surface mounted almost normal to the wing at the tip. The wing is connected to the suction surface of the wing with a smooth fillet. Some of the aircraft that have flown with such a winglet are the MD-11, the Gulfstream III, the DC-10 and the B-767 (Webber and Dansby 1983 and Devoss 1986). The Whitcomb wing tip reduces marginally, by -1% to 2%, the drag on some aircraft (Shevell 1989). Closely related in concept to the Whitcomb winglet is a series of winglets set at varying angles to the planform plane, which are referred to as "wing tip sails." Spillman (1978) has reported up to a 29% reduction in lift dependent drag in flight tests of (small aspect ratio) wings fitted with sails.

Platzer and Souders (1979) is a good, though now somewhat dated, review of tip vortex cavitation knowledge. Cavitation inception is known to occur in the region immediately downstream, to as far as two chords downstream, of the generating wing (Arndt et al. 1991, Maines and Arndt 1993, Stinebring et al. 1991, Green 1991). Inception is generally highly unsteady, occurring first at one location and subsequently up or downstream from it. Upon further reducing the flow cavitation number below σ_i, a long portion of the tip vortex cavitates. These observations are consistent with the known minimum of vortex core pressure near the hydrofoil trailing edge (owing to rapid rollup), and with the small axial pressure gradient along a tip vortex centerline (resulting from the small variation in υ_θ with downstream distance).

Tip cavitation inception is highly dependent on small details of the flow near the tip. Stinebring et al. (1991) and McCormick (1962) have shown that merely roughening the pressure surface tip region of a hydrofoil substantially reduces σ_i. Drilling small holes in a hydrofoil from the pressure to the suction surfaces at the tip also reduces σ_i (Arakeri et al. 1985, Sharma et al. 1990). Recently, Chahine et al. (1993) have shown that injection of modest amounts of Polyox solution (a viscoelastic polymer) into a propeller tip vortex can, under optimum conditions, reduce the cavitation inception index by up to 35%. They attribute this reduction to a significant thickening of the vortex core caused by the viscoelasticity of the solution. The dependence of tip vortex σ_i on small details of the tip flow is congruent with the known sensitivity of the single phase tip flow to the same details. The size and quantity of freestream nuclei also has a substantial impact on σ_i. Arndt and Keller (1992) have measured a doubling of σ_i when the freestream fluid is changed from 'strong' water (few and small nuclei) to 'weak' water (many, large nuclei).

4.2 The ducted tip wing geometry

This chapter documents one successful tip cavitation inception delay device — the ducted tip. Before discussing our experimental studies of the ducted tip geometry, we begin with a brief explanation of the rationale for this novel geometry.

As a consequence of Helmholtz vortex laws, the total shed circulation from a wing is essentially established once the wing lift is specified. Therefore, the only way to modify the tip vortex core pressure (and thus the cavitation inception index, σ_i) is to redistribute this shed circulation. In particular, the less concentrated the shed circulation from a wing, the larger the tip vortex core will be, and hence the lower its inception index.

A conventional planar wing sheds (in theory, see e.g. Milne-Thomson (1958)) a line of vorticity in the Trefftz plane (Figure 4.1 (a)). Any wing with an elliptical or near elliptical loading (a desirable characteristic for maximizing L/D) has this shed vorticity concentrated at the wing tips, which accounts in part for the small vortex core radius and hence high σ_i of elliptically loaded wings*.

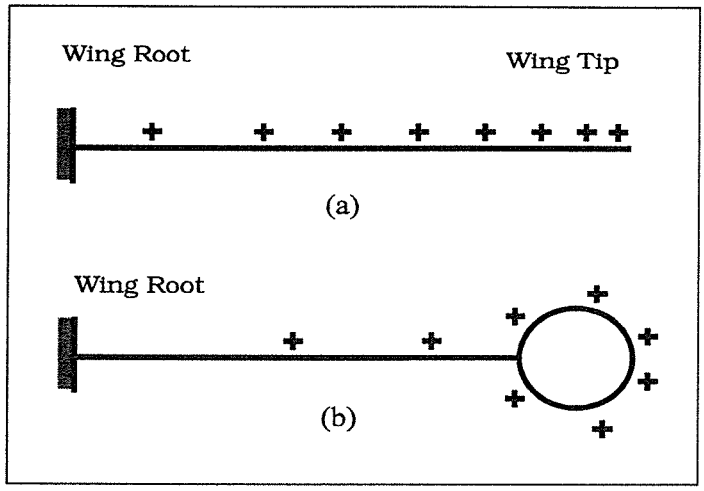

Figure 4.1 Shed vorticity in the Trefftz plane from (a) conventional and (b) ducted tip wings

Non-planar wings (Cone 1963) are not subject to the same near-elliptical loading constraint as conventional wings, and hence do not necessarily shed concentrated vorticity at the wing tip. They therefore potentially have much lower tip vortex cavitation inception indices and, according to Cone, less induced drag, than conventional wings.

The ducted-tip wing is one example of a non-planar wing. It consists of a conventional planar wing to which is mounted a hollow duct, approximately aligned with the wing chord (Figure 4.2). Figure 4.1 (b) is a Trefftz plane schematic of the configuration. Provided that the flow through the duct has little rotation (a reasonable assumption if the entrance to the duct is near the wing leading edge), and the flow around the exterior of the duct has a significant swirl (again, a reasonable assumption because the

* Real fluid effects that cause the formation of secondary vortices have only a slight impact (addition of a small amount of countersign vorticity near the tips, and smearing of the distribution) on the shed vorticity distribution.

large pressure gradient that exists near the wing tip, from the pressure surface to the suction surface, will cause a rapid tangential flow around the tip), there will be significant vorticity shed from the duct, as illustrated in Figure 4.1(b). Because this shed vorticity is spread over a region of radius comparable to the (large) duct radius, it seems plausible that the resulting tip vortex core radius will also be large. This insight into the distribution of shed vorticity encouraged us to explore experimentally the ducted tip geometry.

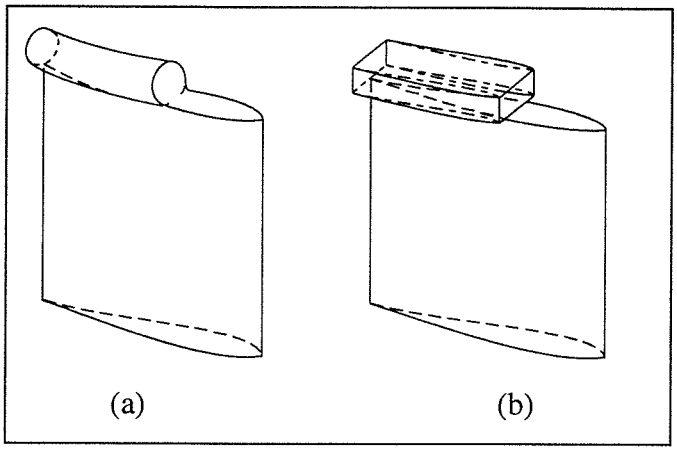

Figure 4.2 Schematics of wing tip devices. Flow is right to left. (a) Ring wing tip. (b) Bi-wing tip.

4.3 Experimental Apparatus and Procedures

The line-of-reasoning described in section 4.2 leads one to hope that the ducted tip wing geometry has superior tip cavitation characteristics. From a practical standpoint, one is not merely interested in improvements in tip σ_i, one must also know that these improvements are not coincident with a large lift reduction or drag increase. Consequently, the experimental program described here consisted of two discrete parts — measurement of the inception characteristics of a ducted tip wing, and measurement of the lift and drag behaviour of such a wing.

The tip vortex inception measurements were carried out by my supervisor, S. I. Green, in the Low Turbulence Water Tunnel (LTWT) at Caltech. The water tunnel facility has a test section of 30.5 cm × 30.5 cm × 2.5 m long, with a freestream velocity adjustable up to 10 m/s. The freestream pressure, p_∞, can be varied from slightly above atmospheric pressure to 25 kPa by means of a vacuum pump. By using a deaeration system and diatomaceous earth filtration, the freestream nuclei content of the water was controlled. A van Slyke device was used to measure the water's total dissolved air content.

A rectangular planform, untwisted, constant airfoil section (NACA 64-309 modified), hydrofoil was reflection-plane mounted in the LTWT. The chord of this hydrofoil was 15.2 cm, and the semispan was 17.8 cm, resulting in an effective aspect ratio of 2.3. The Reynolds number based on chord length for all the cavitation tests was in the range $1.1 \times 10^6 < \mathrm{Re} < 1.6 \times 10^6$.

This basic wing was fitted with two different tips. The first tip was a duct comprised of a 2.9 cm outside diameter (with a wall thickness of 0.2 cm) cambered brass pipe, 10.2 cm long, attached flush with the hydrofoil trailing edge, with axis aligned with the camberline (Figure 4.2(a)). The size of the duct selected for these studies is probably not optimum. A duct was designed based on intuition guided by the following considerations: too large a duct will cause excessive parasite drag, while a duct that is too small will have reduced flow through the duct and will cause little change to the shed vorticity distribution. The second tip, which was used for comparison purposes, was a rounded tip geometry with approximately semicircular cross-sections perpendicular to the chordwise direction, fitted onto the end of the basic wing (Figure 4.7).

Two different procedures were used to study the flow around these wing tip geometries. Surface flow visualization was accomplished using the paint drop technique (Green et al. 1988). With the hydrofoil out of the water tunnel, drops of oil-based paint were dotted on its surface. The hydrofoil was then returned to the tunnel, and the LTWT was quickly accelerated up to a set velocity, causing the paint drops to be smeared in the direction of the local shearing stress.

The second procedure involved cavitation inception measurement and cavitation photography. The large range of inception numbers encountered precluded us from maintaining a constant Reynolds number for all the tests. Instead, cavitation inception testing consisted of setting the hydrofoil angle of attack and gradually increasing U_∞ and decreasing p_∞ until cavitation inception was observed under stroboscopic illumination. Hydrofoil leading edge inception was defined to occur when cavitation was observed on the foil surface half way between the wing root and tip; trailing vortex inception when at least one cavitation event per second was seen. When the leading edge inception index, $(\sigma_i)_{le}$ was larger than the tip vortex inception index, $(\sigma_i)_{tv}$, it was necessary to achieve

$(\sigma_i)_{tv}$ quickly after $(\sigma_i)_{le}$ to avoid erroneous measurements due to the recirculation of cavitation nuclei in the LTWT. Photographs of cavitation were taken by illuminating the hydrofoil and tip vortex in the spanwise direction, and recording on film the light reflected normal to the hydrofoil planform. The cavitation behaviour of the rounded tip was studied first, and several weeks later, following attempts with different ducted tip geometries, testing of the final ducted tip geometry began.

The aerodynamic performance of the two tip geometries was evaluated in the Low Speed Wind Tunnel (LSWT) at the University of British Columbia (Figure 4.3). The truncated rectangular cross-section test section of this facility has dimensions 69 cm × 91 cm and is 4 m long. The maximum velocity attainable in the test section is 40 m/s, although the velocity was maintained at 30 m/s for these experiments. A six-axis strain-gauged force balance, combined with filters, amplifiers and a data acquisition sub-system (Figure 4.4), measures lift and drag forces on models in the test section. The sub-system consists of a Computerscope model ISC-16 for the IBM-PC family of computers, provided on a single plug in card. The ISC-16 model has a 12 bit 1 μsec A/D conversion, accepts analog input signals between -10 Volt and +10 Volt, and has a 1 to 16 channel programmable input multiplexer. About 10,000 samples were taken and averaged for one particular lift or drag measurement. This data acquisition system was calibrated and the results are summarized by the following relations:

$$\text{Drag Force [N]} = 0.579472 \times \text{[Volt]} + 0.029056$$

$$\text{Lift Force [N]} = 10.07694 \times \text{[Volt]} + 0.26435$$

where [Volt] is the corresponding digital reading in voltage from the A/D converter.

The data acquisition sub-system, together with a scanivalve/pressure transducer sub-system, which consists of four pressure transducers, a solenoid driver and a four-cap scanivalve (Figure 4.5) was used for pressure distribution measurements. Each pressure sensor converts the pressure difference (in the range -5 inches to +5 inches H_2O) between its two input connectors to an analog signal of between 1 and 6 Volts. The calibration results of the four pressure sensors are respectively,

$$p_1 - p_{ref}[\mathrm{N/m^2}] = 491.6743 \times [\text{Volt}] - 1730.78$$

$$p_2 - p_{ref}[\mathrm{N/m^2}] = 500.3630 \times [\mathrm{Volt}] - 1738.41$$

$$p_3 - p_{ref}[\mathrm{N/m^2}] = 484.0616 \times [\mathrm{Volt}] - 1730.47$$

$$p_4 - p_{ref}[\mathrm{N/m^2}] = 495.5708 \times [\mathrm{Volt}] - 1745.80$$

where [Volt] is again the digital output reading in voltage from the A/D convertor.

Aerodynamic testing in the LSWT was done on a rectangular planform, untwisted, constant airfoil section (NACA 66-209) basic wing. This acrylic wing is 30.5 cm in chord and 35.6 cm in semi-span, and is fitted with 92 surface pressure taps. Several different tips were attached to the basic wing, including a series of cambered circular aluminum ducts 3.8 cm in outside diameter (with a wall thickness of 0.2 cm) with lengths ranging from 19.8 cm to 30.5 cm (i.e. 65% of wing chord to 100% of wing chord). These ducts were aligned with the wing trailing edge and were affixed approximately parallel to the wing camberline (Figure 4.2(a)). An elliptical wing tip duct, with major axis 10.5 cm (aligned normal to the wing planform), minor axis 3.9 cm, and length 19.8 cm was also tested. The last type of ducted tip tested was a "bi-wing" configuration.

The "bi-wing" tip (Figure 4.2(b)) was constructed of two parallel NACA 0006 short airfoils of 15 cm chord and 3.5 cm span joined together at both span ends with thin aluminum plates. The chordline-to-chordline separation of these airfoils was 3.5 cm. This bi-wing tip was attached to the tip of the basic wing with the short airfoils aligned parallel, and in subsequent tests ±10° from parallel, with the basic wing. All plate/wing junctions were then faired with putty before aerodynamic testing.

For comparison purposes, two other tip geometries were also wind tunnel-tested. A semicircular tip constructed of acrylic and body filler 3.8 cm in span was one conventional geometry tested, and a square cut tip (i.e. constant airfoil section to the tip, where the wing chord falls abruptly to zero) 3.8 cm in span was also tested.

In summary, a number of different wing tip goemetries were tested in the wind tunnel, all with semi-spans of 39.4 cm, though with aspect ratios varying from 2.58 for the square cut tip, to 2.60 for the rounded tip, to 2.67 for the 65% partial chord ducted tip. The aerodynamic test configurations were not geometrically similar with the cavitation test models, but they were nearly so.

Three aerodynamic measurements were made in the LSWT: the lift coefficient, C_L, versus angle of attack α, the drag coefficient, C_D, versus α, and the pressure distribution on both sides of the basic wing. Flow visualization of the flow field around the ducted tip in the LSWT was carried out by using tufts on the model.

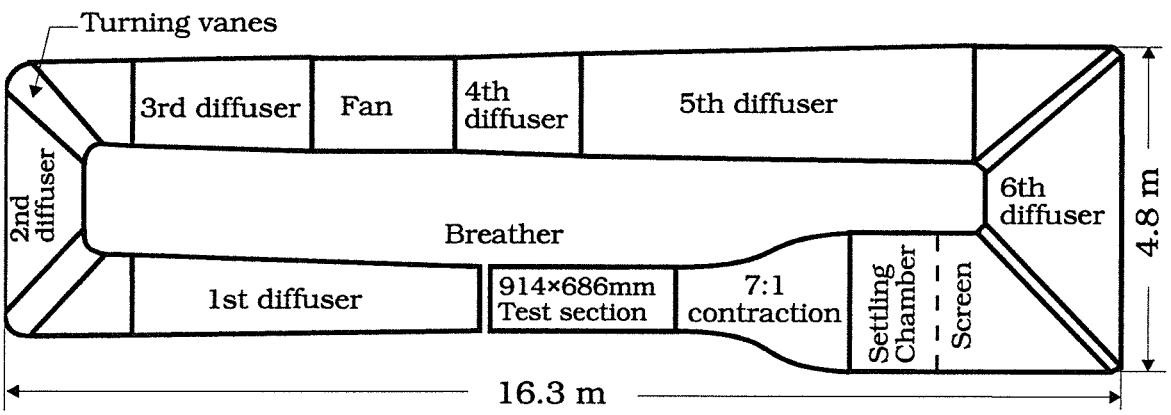

Figure 4.3 The Low Speed Wind Tunnel at the University of British Columbia.

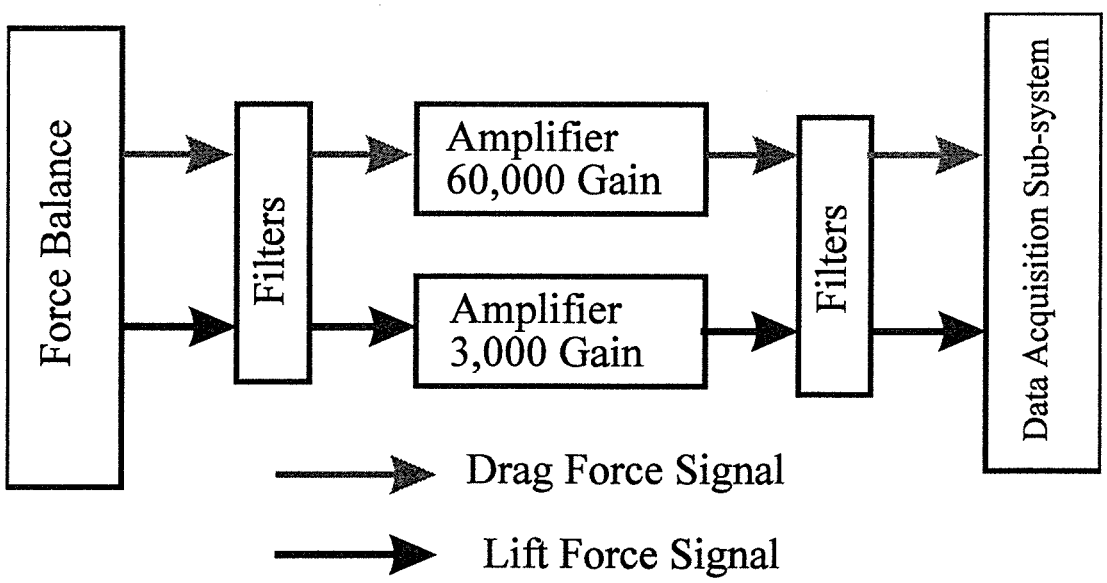

Figure 4.4 The data acquisition system for lift and drag measurement in the LSWT.

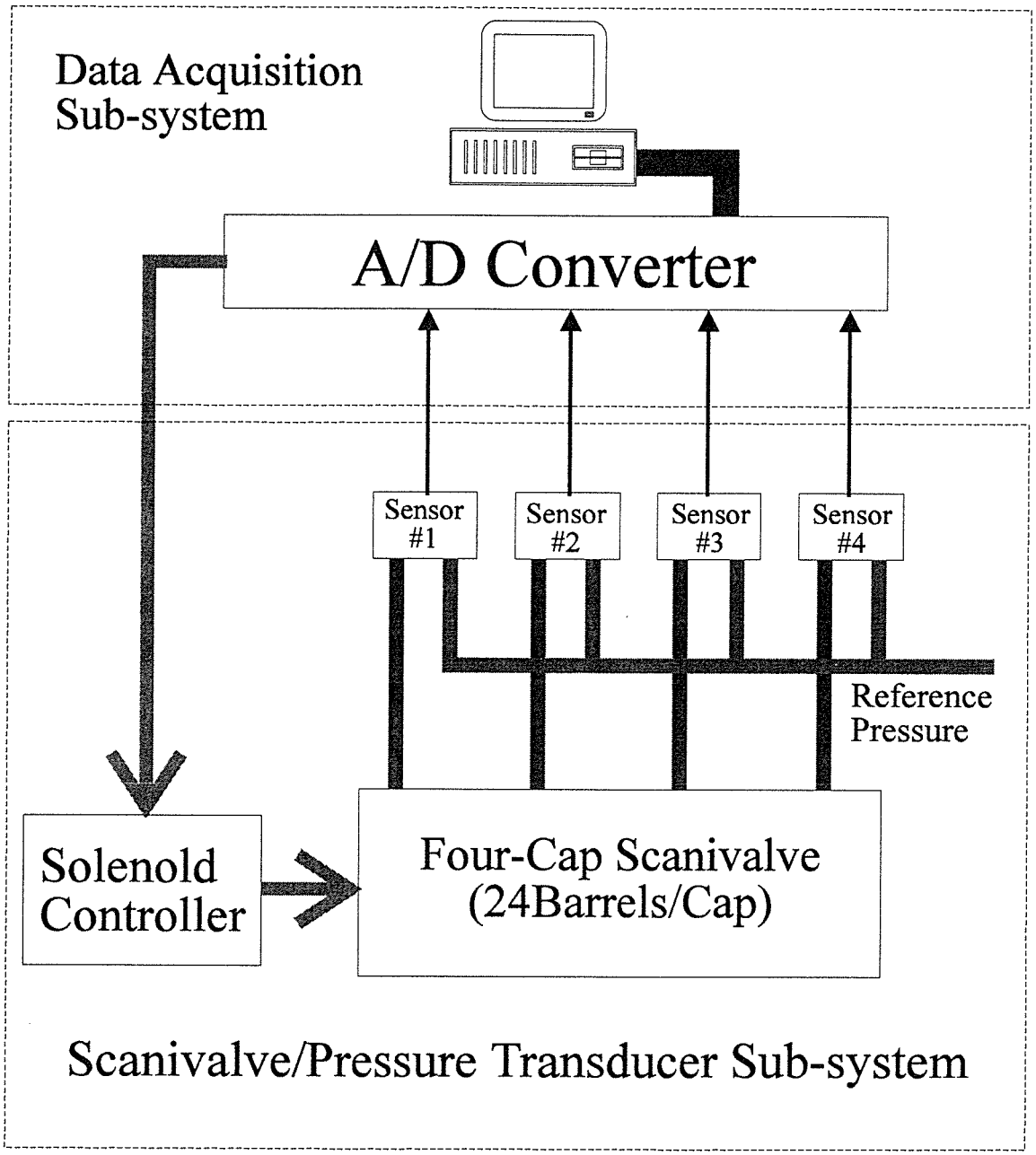

Figure 4.5 The data acquisition system for pressure measurements in the LSWT.

4.4 Results And Discussion

This section includes the cavitation results of the ducted tip, which were part of the work done by my supervisor at Caltech. A completed picture on the novel ducted tip will be presented in this manner.

4.4.1 Flow Visualization

Examining the surface flow over an airfoil is perhaps the easiest way to assess qualitatively the performance of different wing tip geometries. Figure 4.7(a) is a view of the surface flow over the pressure side of the rounded tip geometry. The flow direction is nearly streamwise near the reflection-plane mount (near the bottom of the photograph) and acquires an increasing spanwise component as the tip is approached. Over the majority of the suction side of the wing (Figure 4.7(b)) there is also an increasing spanwise velocity component (for this side, directed from the tip to the root) as the tip is approached. Streaklines directed toward the tip on the suction side result from, respectively, the tip vortex rollup in the region near the tip (refer to Figure 4.6), and a secondary vortex near the wing root. Note that the reflection plane mount seems to affect the wing only over the bottom 20% of the semi-span. The tip flow in particular is basically unaffected by the presence of the water tunnel floor.

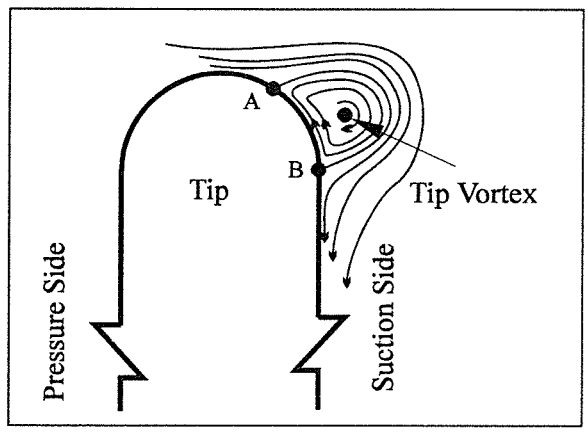

Figure 4.6 Tip vortex rollup in the Trefftz plane.

(a)

(b)

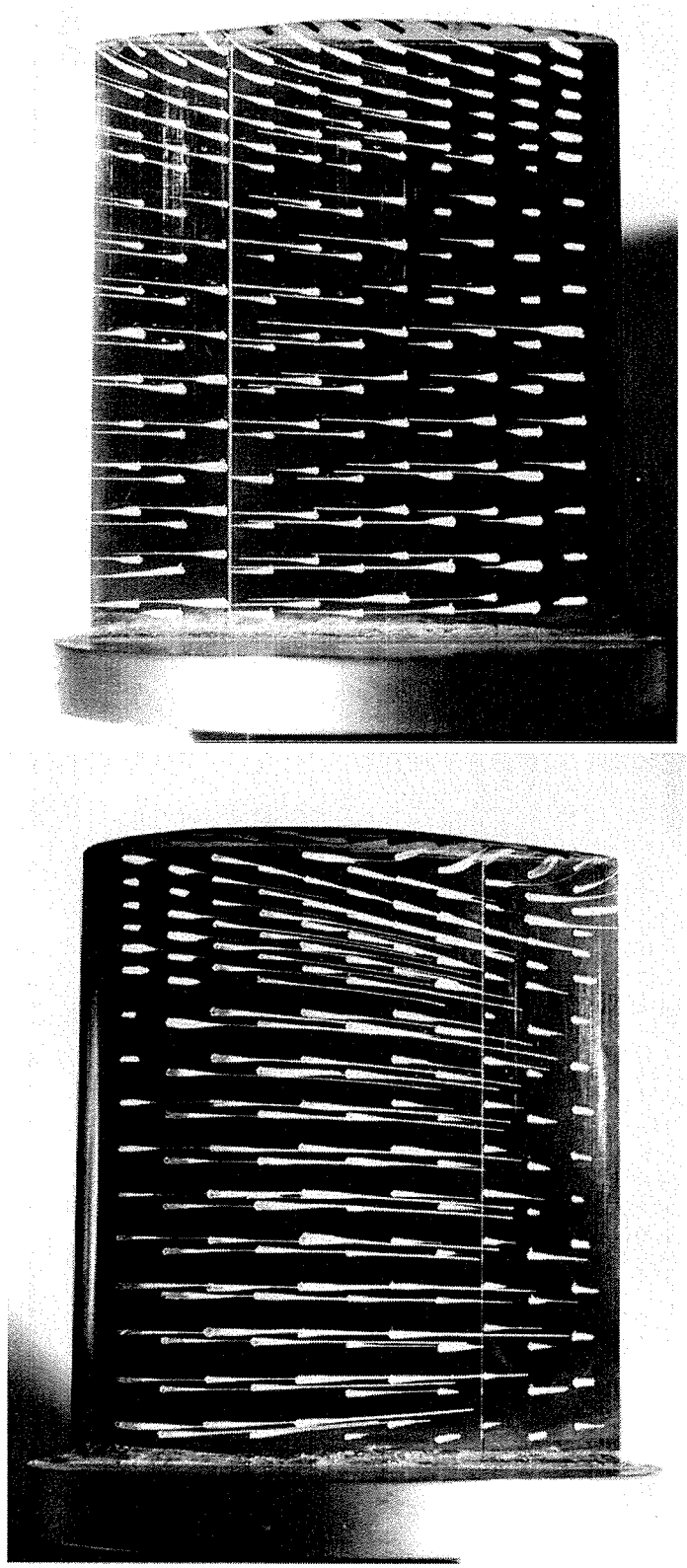

Figure 4.7 Surface flow visualization on the rounded tip geometry. (a) Pressure side. Flow is right to left. (b) Suction side. Flow is left to right. (Photograph source: Green 1988)

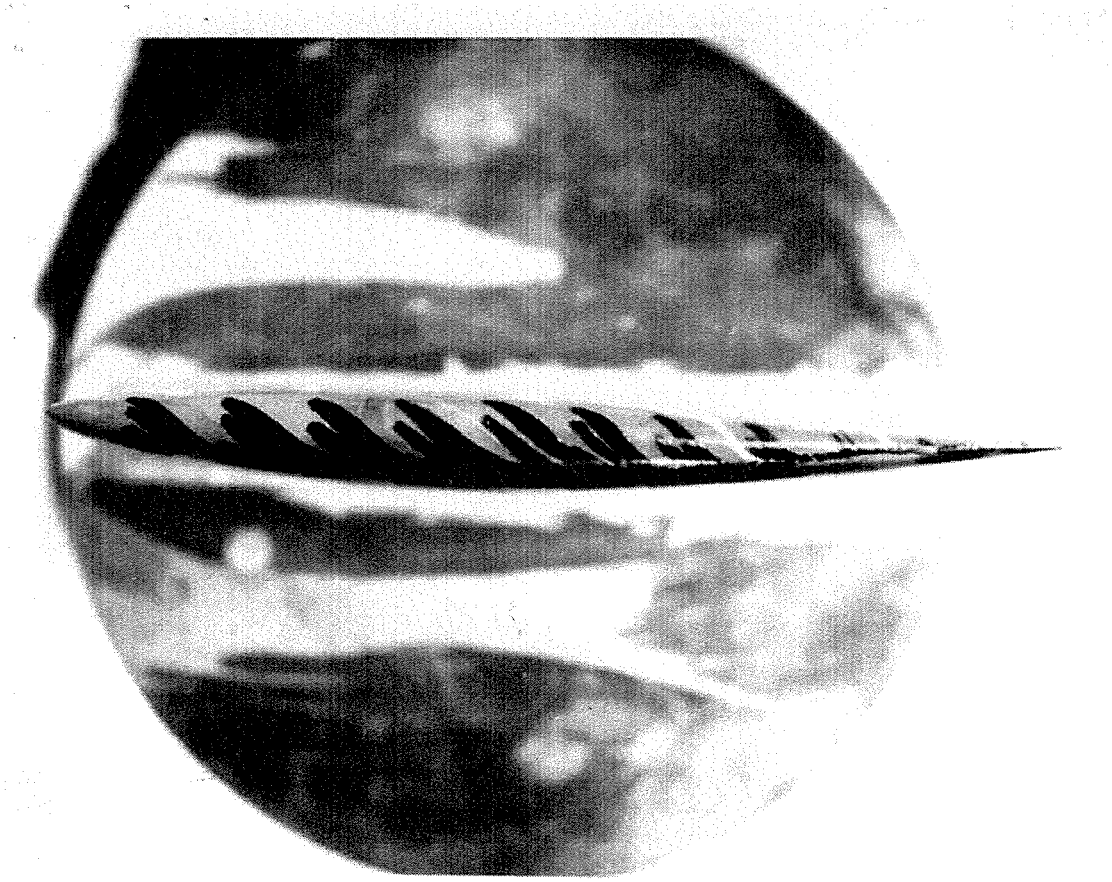

(c)

Figure 4.7 Surface flow visualization on the rounded tip geometry.
(c) Inboard view of tip. Flow is left to right. The wing pressure surface is at the top.
(Photograph source: Green 1988)

The surface flow over the ducted tip geometry is quite different from that over the conventional tip geometry. The spanwise velocity component at the trailing edge, on both the suction and pressure surfaces (Figure *4.8*), is substantially less than that of the rounded tip wing. At one third of the spanwise distance from the reflection plane mount, for example, the angle the rounded tip streaklines make with the freestream direction is about 50% greater than the streakline angles of the ducted tip. This difference in spanwise velocity component implies that the ducted tip wing sheds less bound circulation over the majority of the wing span than does the rounded wing tip. Smear lines in the duct (Figure 4.8(d)) have little swirl, whereas those on the duct exterior indicate a large tangential velocity. This observation confirms that substantial vorticity is shed from the duct, as indicated in Figure 4.1(b).

One may be concerned that the flow will separate from the ducted tip. Vibration of tufts located on the outside suction side close to the entrance of the duct implies that local flow separation occurs there at elevated angles of the attack (Figure 4.9). This flow separation will cause elevated parasite drag.

(a)

(b)

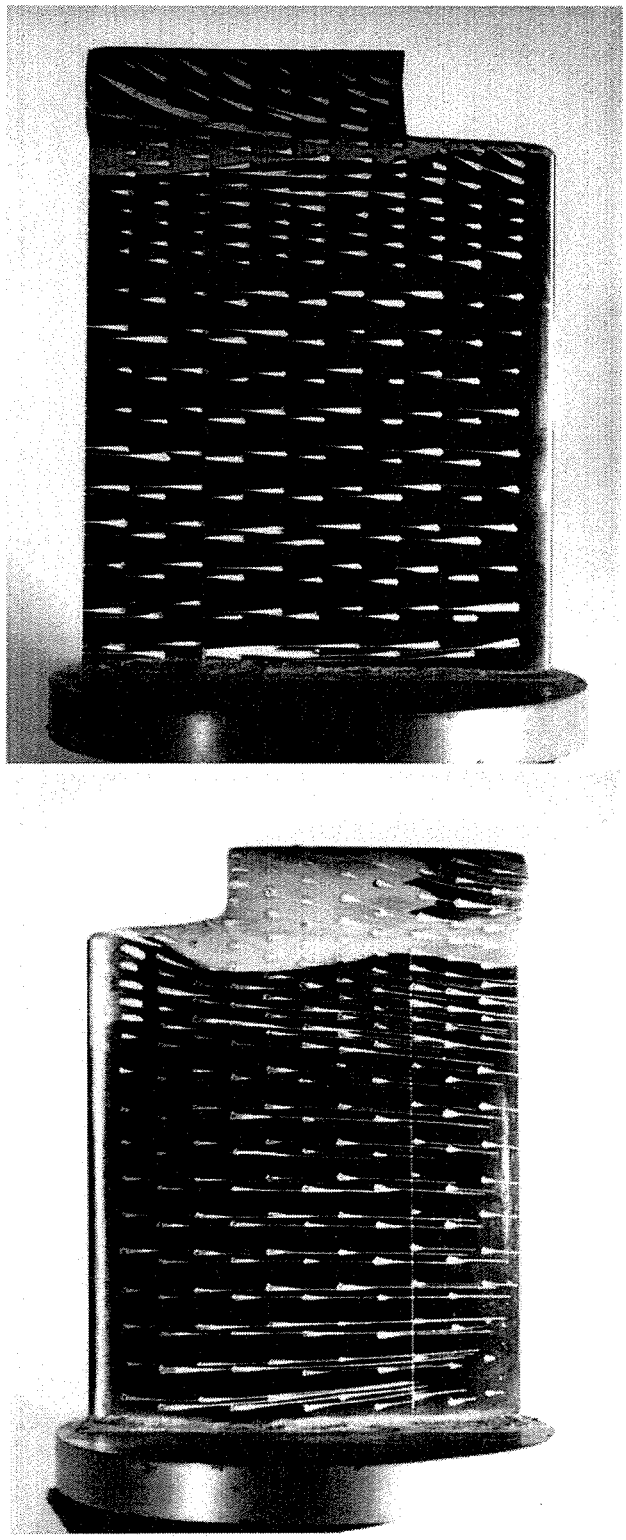

Figure 4.8 (a) Surface flow visualization on the pressure side of the ducted tip wing. The flow is right to left. $\alpha=7°$, $Re=1.2\times10^6$.
(b) Suction side view of the wing in Figure 4.8(a). Flow is left to right.
(Photograph source: Green 1988)

(c)

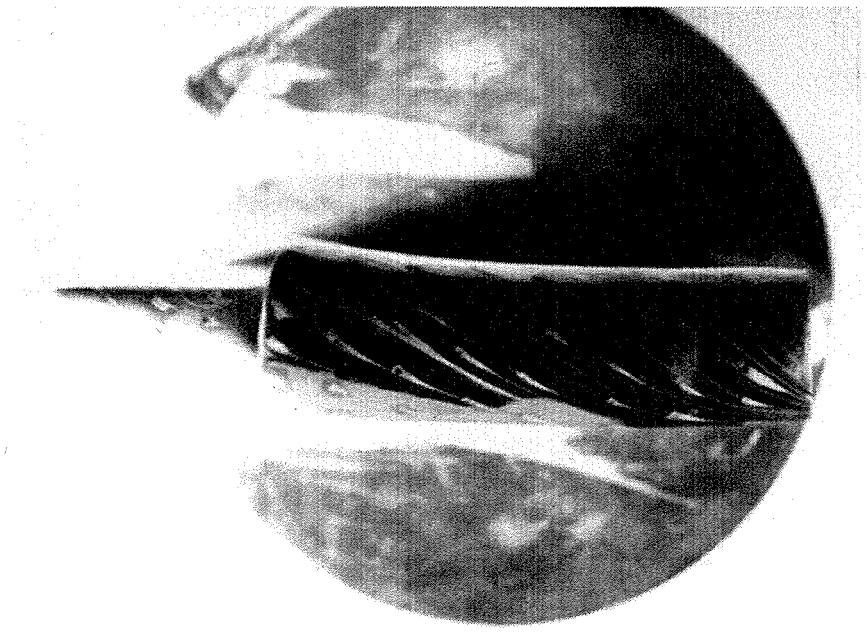

(d)

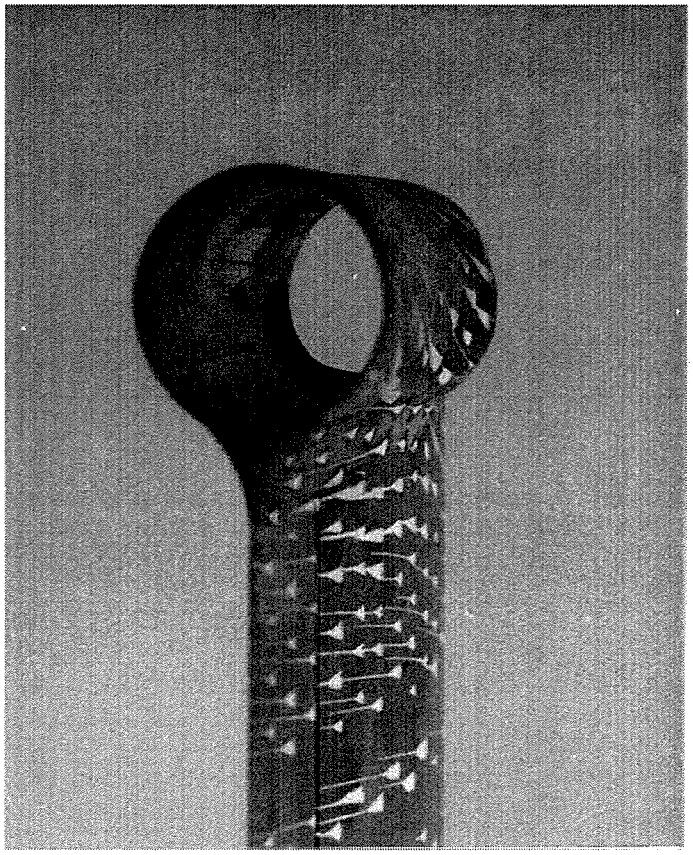

Figure 4.8 (c) Inboard view towards tip of the flow in Figure 4.8(a). The flow is left to right. The pressure surface is at the top of the photograph.
(d) Upstream view through the duct of the flow in Figure 4.8(a). The pressure surface is to the right.
(Photograph source: Green 1988)

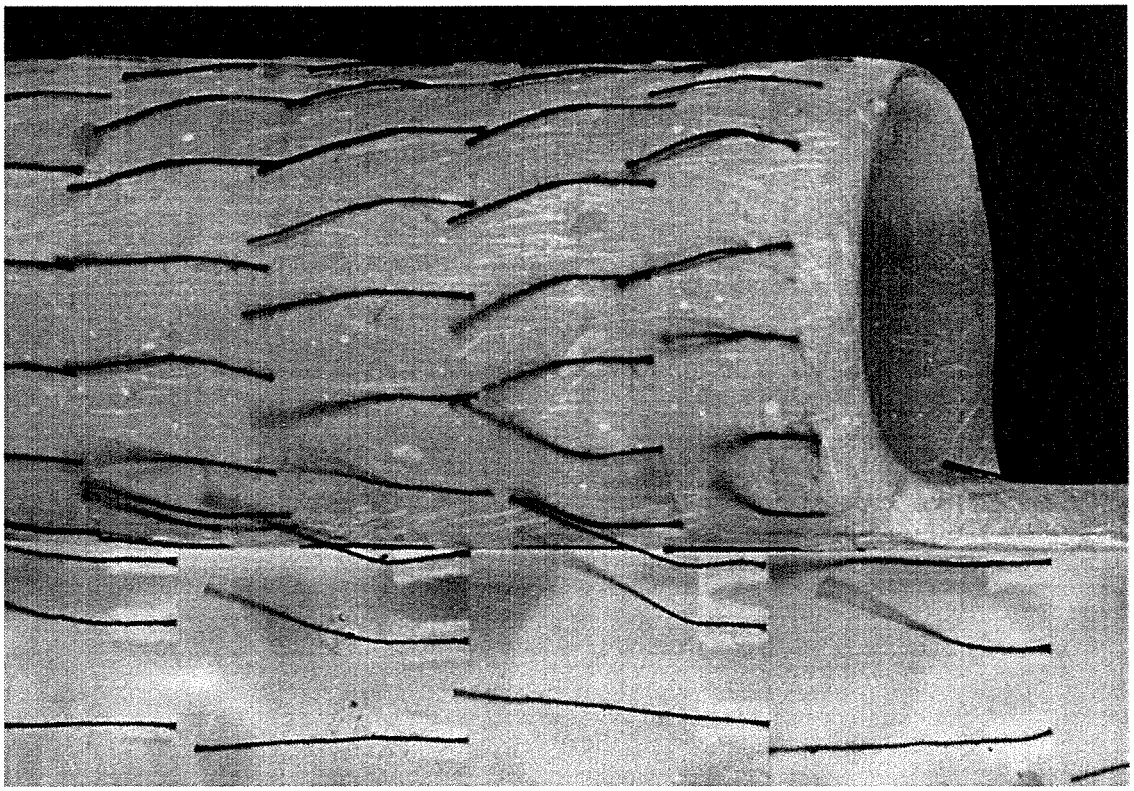

Figure 4.9 Separated flow near the entrance of the ducted tip. $\alpha=12°$. The flow is right to left.

4.4.2 Cavitation Characteristics

Figure 4.10 is a photograph of developed tip vortex cavitation behind the rounded tip geometry. The cavity cross-section is oval immediately downstream of the tip, and becomes nearly circular within one chord of the trailing edge. This shape is consistent with the known transition of the tip vortex velocity field from asymmetric at the hydrofoil trailing edge to nearly axisymmetric a short distance downstream (Fruman et al. 1991, Green and Acosta 1991). Development of this continuous vapour-filled tip vortex cavity occurs when the cavitation number is decreased by just 10-20% below σ_i. The rapidity of the cavitating vortex development implies that the axial pressure gradient along the core of a tip vortex is small, in agreement with recent measurements by Green (1991).

Unlike a developed trailing vortex cavity, which is a steady phenomenon, cavitation inception is highly unsteady. Cavitation inception in the rounded tip vortex is observed 0.3 to 1.5 chords downstream of the hydrofoil trailing edge; the exact location of trailing vortex inception fluctuates in an apparently random manner within this range. It is not known if the fluctuation of the inception location is due to variability in the location at which freestream nuclei are captured by the vortex (Ligneul and Latorre 1993), or due to the fluctuating pressure field within the tip vortex core (Green 1991).

Trailing vortex inception occurs for $\sigma_i = 1.8 \pm 0.2$ near the hydrofoil operating angle of attack, $\alpha = 7°$ (Figure 4.11). As α is varied about the operating angle of attack, the inception index varies much less rapidly than the $(\alpha - \alpha_0)^2$ dependence predicted by a simple Rankine vortex model. Arndt and Keller (1992) have observed the same effect, which they attribute to the significant tension that can be sustained by low-nuclei-content water prior to cavitation inception. Hydrofoil leading edge surface cavitation inception occurs for $\sigma_i = 0.9 \pm 0.1$, substantially lower than the value for tip vortex inception. This observation implies that tip vortex cavitation occurs in many situations for which surface cavitation on the hydrofoil is not present.

The inception indices plotted in Figure 4.11 were determined in 'strong' (i.e. low nuclei content) water. Water with more freestream nuclei exhibited much higher

inception indices (greater by a factor of 2 when the dissolved air content of the water was doubled from 4 to 8 ppm). Arndt and Keller (1992) and Arndt et al. (1991) observed a similarly strong dependence of σ_i on nuclei content.

Cavitation inception from the hydrofoil ducted tip was first observed on the outside edge of the suction surface portion of the duct. This surface cavitation is caused by the separation (Figure 4.9) that occurs as the flow, which has a high tangential velocity around the tip, encounters the duct leading edge. Figure 4.12 is a photograph of cavitation nuclei generated by the duct surface that have migrated into the ducted tip vortex. Note the diffuse appearance of the vortex.

True trailing vortex cavitation occurs only when σ is reduced well below the inception index of both the ducted tip surface cavitation and the hydrofoil leading edge cavitation. As a consequence, cavitation nuclei generated by both the wing leading edge and duct surface cavitation are swept into the tip vortex prior to inception there. Because the tip vortex is exposed to water of much higher nuclei content than the freestream water, the tip vortex will cavitate at relatively higher σ_i. The ducted tip vortex inception measurements are thus biased to high values.

Despite this "unfavourable" bias, the ducted tip vortex data (Figure 4.13) show a remarkable decrease in σ_i relative to the rounded tip geometry. For an angle of attack of 7°, the inception index of the ducted tip vortex is $\sigma_i = 0.9 \pm 0.1$. In contrast, at the same angle of attack, the rounded tip vortex has $\sigma_i = 1.8 \pm 0.2$ (i.e. σ_i of the ducted tip is 50% less). For angles of attack of 5° and 10°, the ducted tip vortex σ_i is 0.5 ± 0.05 and 1.8 ± 0.2. These values are respectively 61% and 28% less than the rounded tip σ_i values (1.3 ± 0.1 and 2.5 ± 0.1) at the same α.

As explained previously, the inception index of tip vortex cavitation is a strong function of the nuclei content of the water. One might therefore posit that the large reduction of σ_i, when the ducted tip is installed, results from a decrease in the nuclei content of the water between the time of the rounded tip tests and the ducted tip tests. In fact, two observations point to an <u>increase</u> in freestream nuclei between the tests. One such observation is the increase in the dissolved air content (from 5 ppm to 7 ppm with an

error of ± 0.5 ppm) between the rounded and ducted tip tests. The observed increase in hydrofoil leading edge σ_i (from 0.3 to 0.8 at $\alpha = 5°$, from 1.0 to 1.5 at $\alpha = 7°$, and from 3.0 to 3.5 at $\alpha = 10°$) between the rounded and ducted tip tests is another strong indicator of an increase in freestream nuclei concentrations.

In summary, two factors tend to bias the ducted tip σ_i to elevated values — the presence of more naturally-occurring freestream nuclei during testing of that geometry, and the generation of nuclei by cavitation from the hydrofoil leading edge. Despite these two influences, cavitation inception from the ducted tip geometry occurred at much lower inception indices than from the rounded tip geometry.

One may be concerned that the gains in cavitation inception improvement resulting from the ducted tip modification are negated by the increase in other forms of cavitation. For example, one might postulate that the ducted tip geometry would redistribute the hydrofoil loading, causing the wing leading edge σ_i increase referred to above. This is not the case. Except for a small region near the wing tip, the measured pressure distributions on the basic wing were virtually unchanged (refer to pressure distribution measurements shown in section 4.4.3; $\bar{c}_p$ the same to ±7%) with the addition of the ducted tip. The unchanged pressure distribution implies an unchanged wing loading. Therefore, leading edge cavitation is <u>not</u> significantly affected by the addition of the ducted tip, whereas tip vortex cavitation is significantly reduced by the ducted tip.

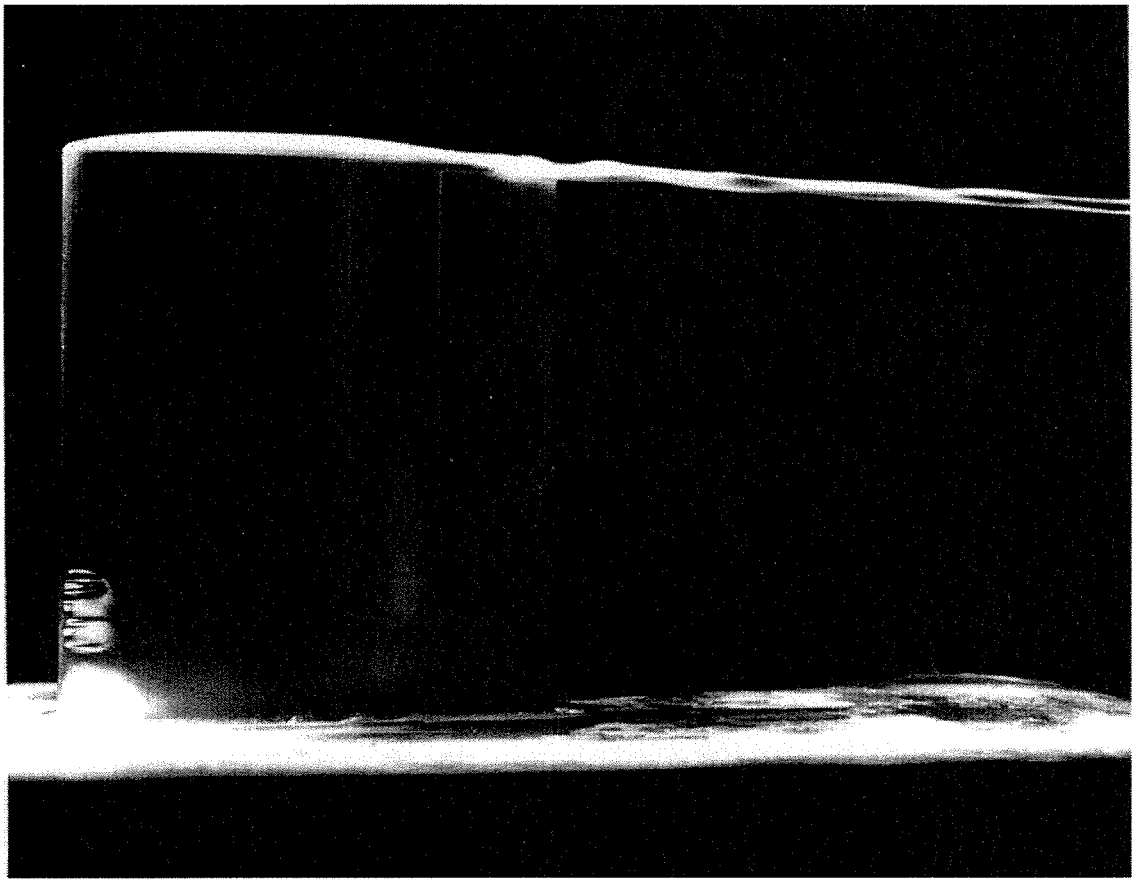

Figure 4.10 Developed trailing vortex cavitation behind the rounded tip geometry.
α=7°, Re=1.3×10^6, σ=1.8, DAC=5.4 ppm.
(Photograph source: Green 1988)

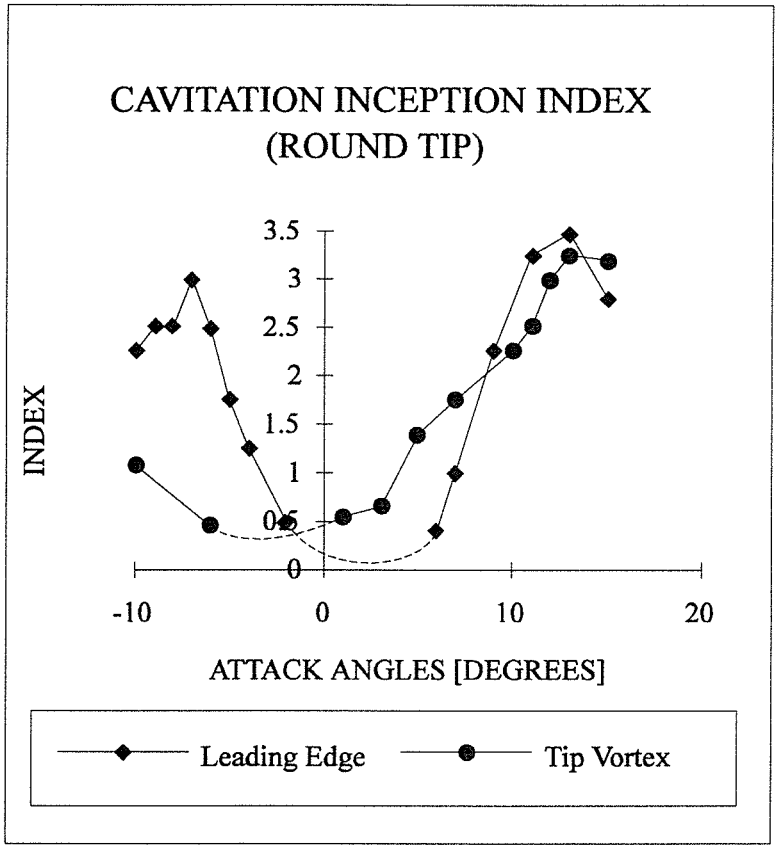

Figure 4.11 Cavitation inception index versus angle of attack for the rounded tip geometry. Re≈ 1.4×10⁶, DAC = 5.4 ppm (uncertainty in $\alpha = \pm 0.2°$ and in $\sigma_i = \pm 10\%$ at the 95% confidence level)

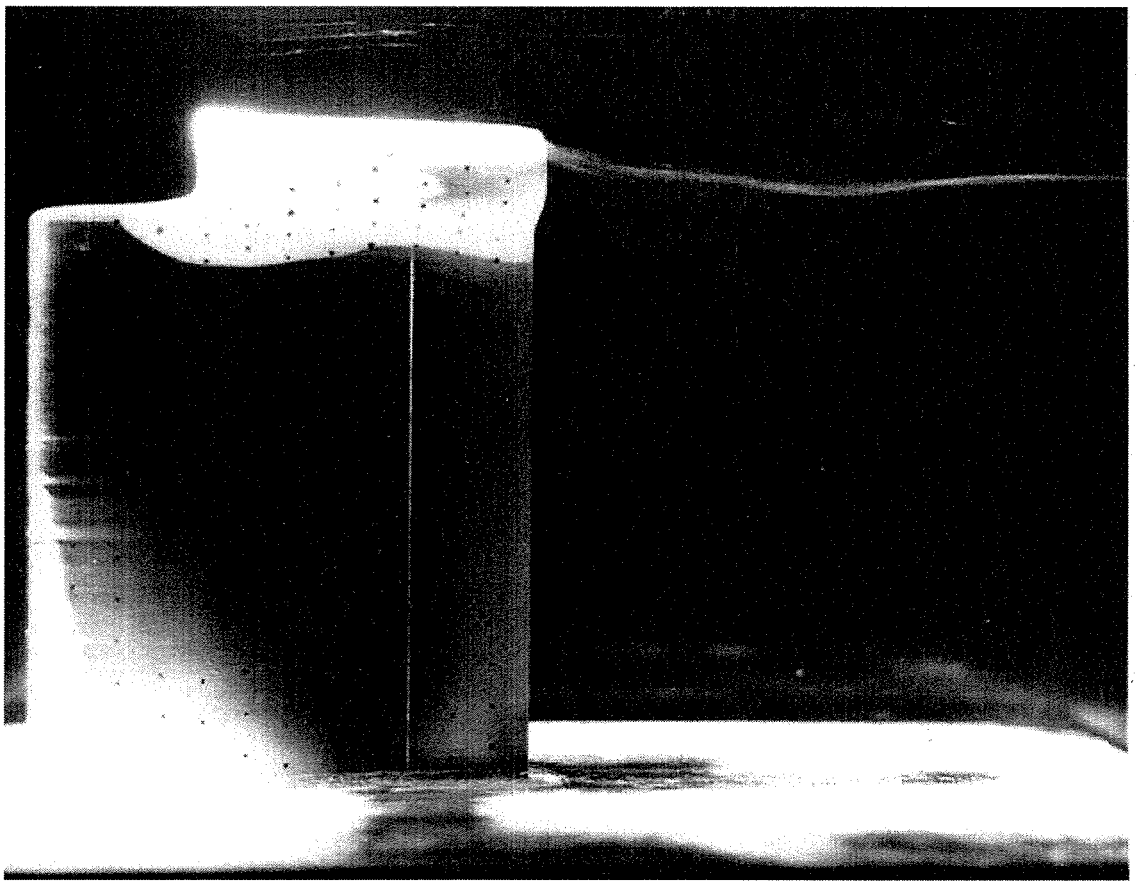

Figure 4.12 Ducted tip vortex made visible by migration of cavitation nuclei, generated at the duct leading edge, into the vortex.
α=7°, Re=1.2×10^6, σ=1.5, DAC=7.0 ppm.
(Photograph source: Green 1988)

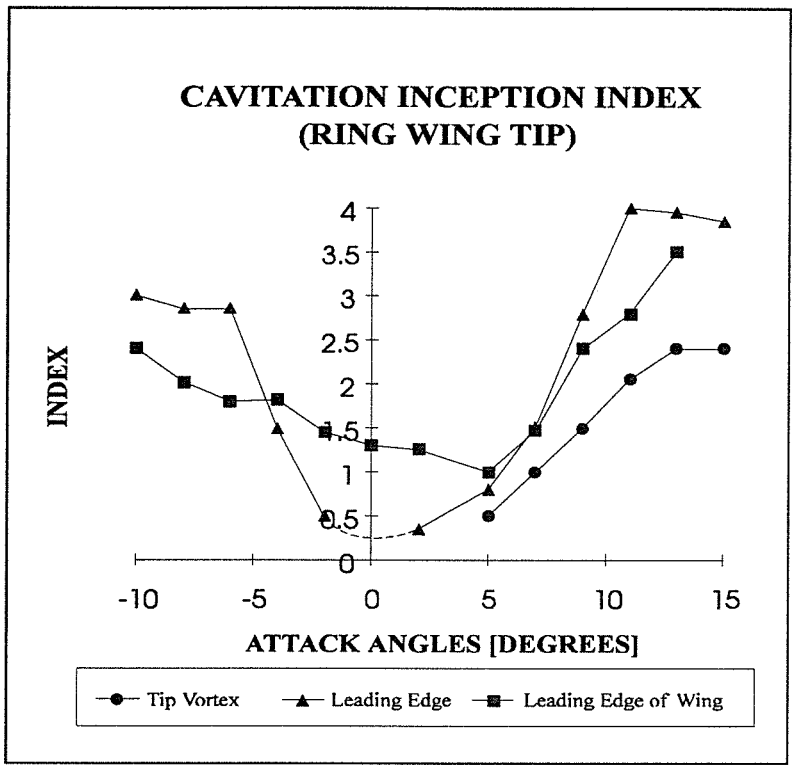

Figure 4.13 Cavitation inception index versus angle of attack for the ducted tip geometry. Re ≈ 1.4 × 10⁶, DAC = 7.0 ppm. (Uncertainty in $\alpha = \pm 0.2°$ and in $\sigma_i = \pm 10\%$ at the 95% confidence level).

4.4.3 Aerodynamic Performance

These encouraging cavitation inception results prompted a study of the aerodynamic performance of the ducted tip and other tip geometries.

Wind tunnel testing demonstrated that the aerodynamic performance of the square cut and rounded tip wings was identical to within the experimental error (±1% drag and ± 0.5% in lift). The partial chord circular duct tip had the best performance of any of the ducted tip geometries. Consequently, the aerodynamic characteristics of the partial chord ducted tip and the rounded tip — the same tip geometries whose cavitation behaviour was studied in section 4.4.2 — will be emphasized here.

4.4.3.1 The partial chord ducted tip

For all elevated angles of attack (α > 10°) the lift coefficient of the ducted tip geometry (where C_L is based on the planform area of the rounded tip) is about 4% less than that of the rounded tip (Table 4.1). However, the partial chord ducted tip geometry has a 3.4% smaller planform area than the rounded tip, and thus the actual lift coefficients for the two geometries are identical to within experimental error. Surface flow visualizations described in section 4.4.1 suggest that the ducted tip generates greater lift near the wing root. The implication of the congruity of the two lift coefficients is that the additional lift gained from the root of the ducted tip wing is almost precisely offset by the reduced lift attained in the vicinity of the tip.

Table 4.1: Lift Coefficients of the Ducted-tip Wing and the Conventional Wing.

	α=6°	8°	10°	11°	12°	14°	15°	17°
Conventional Tip	0.3797	0.4864	0.5946	0.6272	0.6614	0.7158	0.7484	0.7864
Ducted Tip	0.3730	0.4828	0.5703	0.6014	0.6309	0.6832	0.7181	0.7571
Improvement	-2%	-0.7%	-4%	-4%	-4.6%	-4.6%	-4%	-4%

Unlike the virtually unchanged wing lift, a significant difference in wing drag is observed when the ducted tip is installed (Figure 4.14). For $\alpha < 8°$ the ducted tip geometry has greater drag than the rounded tip, but for larger α the ducted tip geometry has less drag : 6% less at 10°, 8% less at 12°, and fully 10% less at 14° (Table 4.2). Even when allowance is made for the slightly reduced planform area of the ducted tip geometry, there is nonetheless an up to 6% drag coefficient benefit arising from the tip modification. This reduction in drag coefficient is somewhat surprising in view of the obviously increased parasite drag of the ducted wing (arising from both its additional wetted area and the likely existence of interference vortices at the duct-wing junction); the only explanation is that the duct attachment to the wing must reduce substantially its induced drag. This conclusion is borne out by the observation that the drag reduction of the ducted tip is most pronounced at elevated angles of attack, for which the induced drag is a larger fraction of the overall drag.

Table 4.2: Drag Coefficients of the Ducted-tip Wing and the Conventional Wing.

	α=6°	8°	10°	11°	12°	14°	15°	17°
Conventional Tip	0.0107	0.0183	0.0326	0.0488	0.0680	0.1135	0.1418	0.1932
Ducted Tip	0.0110	0.0183	0.0307	0.0449	0.0623	0.1018	0.1279	0.1770
Improvement	-3%	+0.0%	+6%	+8%	+8.3%	+10.3%	+10%	+8.4%

A simple model to explain the reduced induced drag of the ducted tip is shown in Figure 4.15. The downwash caused by shed circulation from the duct is less (by the factor $\cos^2 \Theta$, where Θ is the angle between a portion of the duct and a portion of the planar wing) than the downwash would be if the same shed circulation were redistributed along the duct diameter, in the spanwise direction. The reduction in downwash causes a consequent reduction in induced drag, as suggested by Cone (1963).

Owing to the large parasite drag of the ducted tip geometry, the lift-drag ratio of this geometry is inferior to the conventional tip geometry at low angles of attack. However, for $\alpha > 8°$ the aerodynamic performance of the ducted tip is superior. As shown in Figure

4.16, the improvement in lift/drag ratio with application of the ducted tip varies from 0% to 6% for α between 8° and 15°.

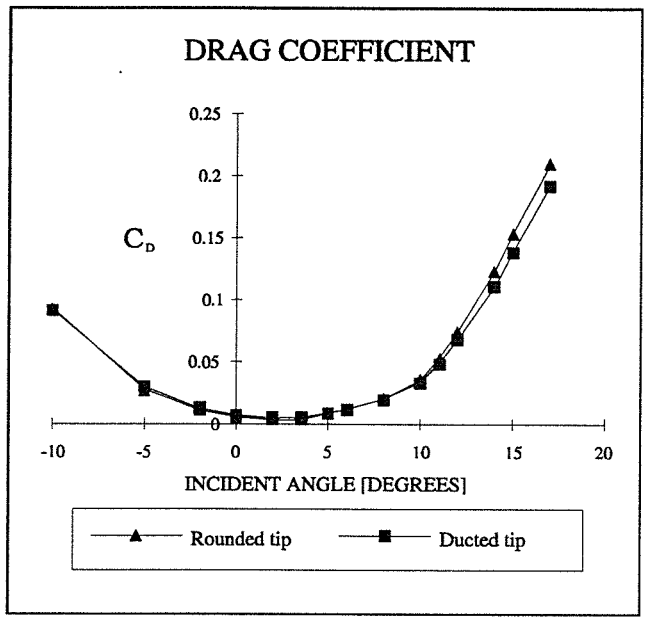

Figure 4.14 Drag coefficients of rounded and ducted tip wings. Re = 7.1 $\times 10^5$(The uncertainty in C_D is $\pm$ 0.0003 and in α is $\pm$ 0.1°, both at the 95% confidence level).

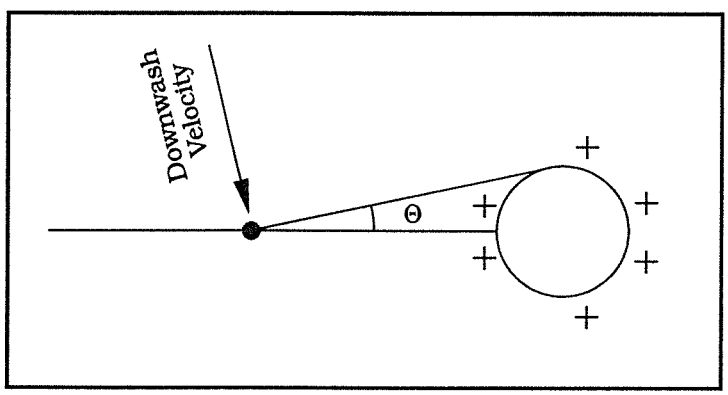

Figure 4.15 A simple model for the reduction in induced drag of the ducted tip geometry

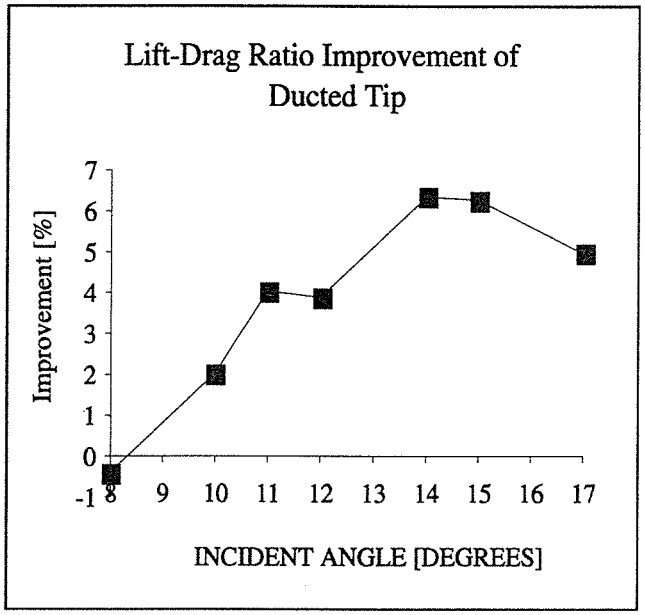

Figure 4.16 Lift/Drag ratio improvement of the ducted wing relative to the conventional tip (The uncertainty in L/D is ± 1%, and in α is ± 0.1° at the 95% confidence level).

Figure 4.17 shows the locations of the 92 pressure taps fitted on both the pressure and suction sides of the basic wing. Note that there are more taps on the suction side than the pressure side, and also that the area near the tip has a dense population of taps. From these measured point values of surface pressure, one can obtain the pressure distribution on both sides of the wing by interpolation and extrapolation. Because no pressure taps are installed on tip devices, only the pressure distributions on the basic wing can be compared for different tip configurations.

As can be seen in Figure 4.17, the pressure taps are quite sparse in some areas of the wing surface. There were only five pressure taps at the leading edge on the suction side and the pressure tap spacing was also very large in the centre of the wing. We had difficulty getting reasonable interpolated/extrapolated pressure data in those regions. For example, even though the experimental results from the five pressure taps at the leading edge decreased monotonically along the spanwise direction, the 2-D inter/extrapolation method we employed yielded a wavy pressure distribution. This difficulty was overcomed by combining 1-D and 2-D inter/extrapolation techniques in this region.

To give some indication of the accuracy of the interpolation procedure, the surface pressure distribution was numerically integrated to yield the lift force. The lift coefficients evaluated in this way at 5°, 8° and 12° angles of attack were compared with the force balance measurements. The maximum error was 7%. The error was likely due to poor resolution of the suction surface pressure peak owing to the large pressure tap spacing near the wing leading edge.

The pressure distribution on the pressure side of the basic wing with a conventional wing tip configuration is shown in Figure 4.18. Figure 4.19 shows the pressure distribution for the ducted tip configuration. Both of the two figures show the local reduction in pressure caused by the outboard crossflow near the tip region (fluid flow from high pressure to low pressure). It is interesting to observe in Figure 4.19 a pressure peak near the 35% chord position at the tip. This location marks the entrance to the duct, and the pressure peak is likely due to the existence of a stagnation point at the entrance of the ducted tip. The pressure behaviour in the leading edge-tip region is obviously different (Figure 4.20) for the two configurations because the conventional tip had a tip

extension all the way to the leading edge, whereas the ducted tip did not extend to the leading edge and therefore had more three-dimensional flow near the leading edge. The average pressure gradient from the wing root to the tip on the pressure side is related to the magnitude of the outboard crossflow and is characteristic of the strength of the tip vortex. We can evaluate the average pressure gradient qualitatively by looking at the tip views (Figures 4.18 (b) and 4.19 (b)). There is no significant difference between this pressure gradient on the conventional wing and on the ducted tip wing except near the wing tip. Figure 4.20 verifies this conclusion.

The three dimensional flow in the tip region is also evident on examination of the pressure distribution on the wing's suction side (Figure 4.21 and 4.22). There is no significant difference, on the majority of the wing surface, between the pressure distribution of the conventional configuration and the ducted tip configuration (Figure 4.23). Close to the midspan of the leading edge, the difference in $\bar{c}_p$ between the two configurations is about 10%. This difference is within the error caused by the extrapolation method we used. Consider pressure taps numbered 43 and 44 (Figure 4.17(b)) for example. A 7% error in the pressure measurement at those two taps will cause a maximum 10% error in the estimated $\bar{c}_p$ at the leading edge, if a linear extrapolation method is used. There is possibly a local suction peak in the trailing edge-tip region, as shown more clearly in the leading edge view (Figures 4.21(b) and 4.22(b)). The measurements do not capture the whole local peak because, due to the add-on tip, no pressure measurements were made within 10% of the semi-span from the tip. Figure 4.24 shows the pressure distribution on the suction side of the basic wing without any tip device installed. There is obviously a suction peak near the wing tip, near the locus of 3-D stagnation points (Point B in Figure 4.6), caused by the roll-up of the primary tip vortex. Such a suction peak has also been observed by Chow et al. (1993) in their pressure distribution measurements on a wing with a rounded tip.

In summary, no pressure distribution difference between tip geometries was observed over the majority of the wing surface. However, near the wing tips the pressure distribution was significantly changed by the addition of tip devices. The pressure measurements are not accurate enough (about ±7%) to confirm the Lift/Drag ratio

improvement, but they are supportive to the cavitation results — tip vortex cavitation is significantly modified by the ducted tip, whereas leading edge cavitation is not significantly affected by addition of the tip device.

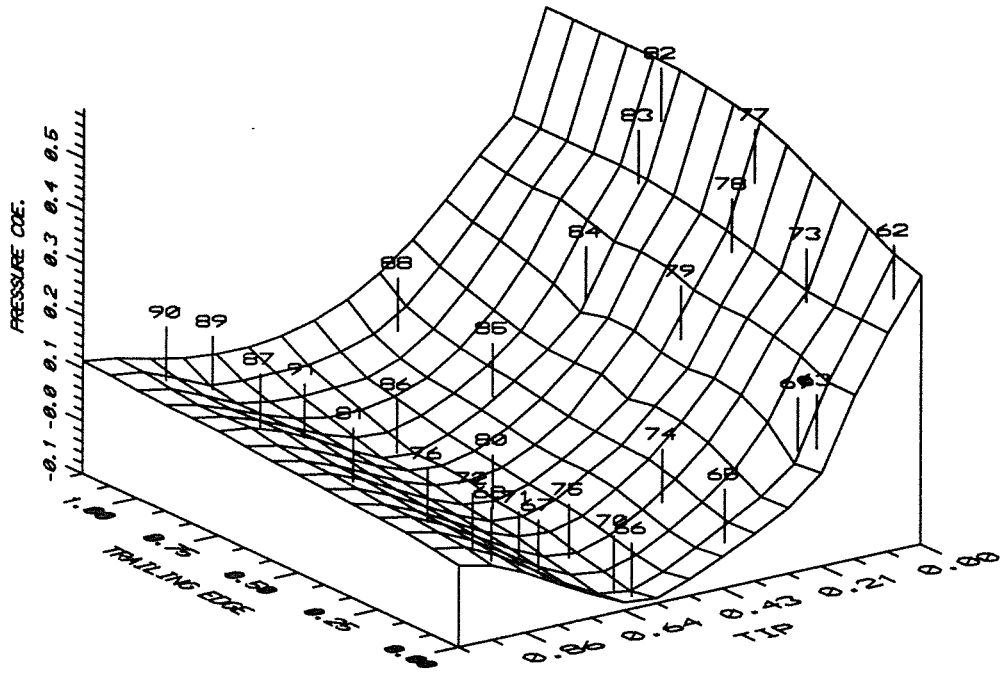

(a)

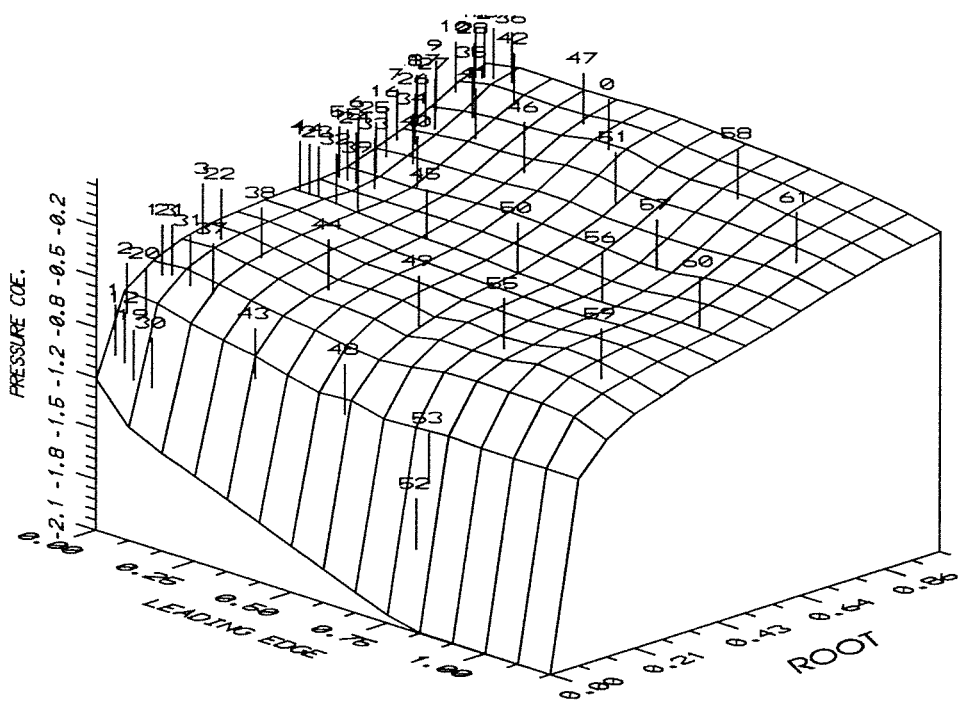

(b)

Figure 4.17: Pressure taps on the surfaces of the basic wing.
(a) pressure side, (b) suction side.

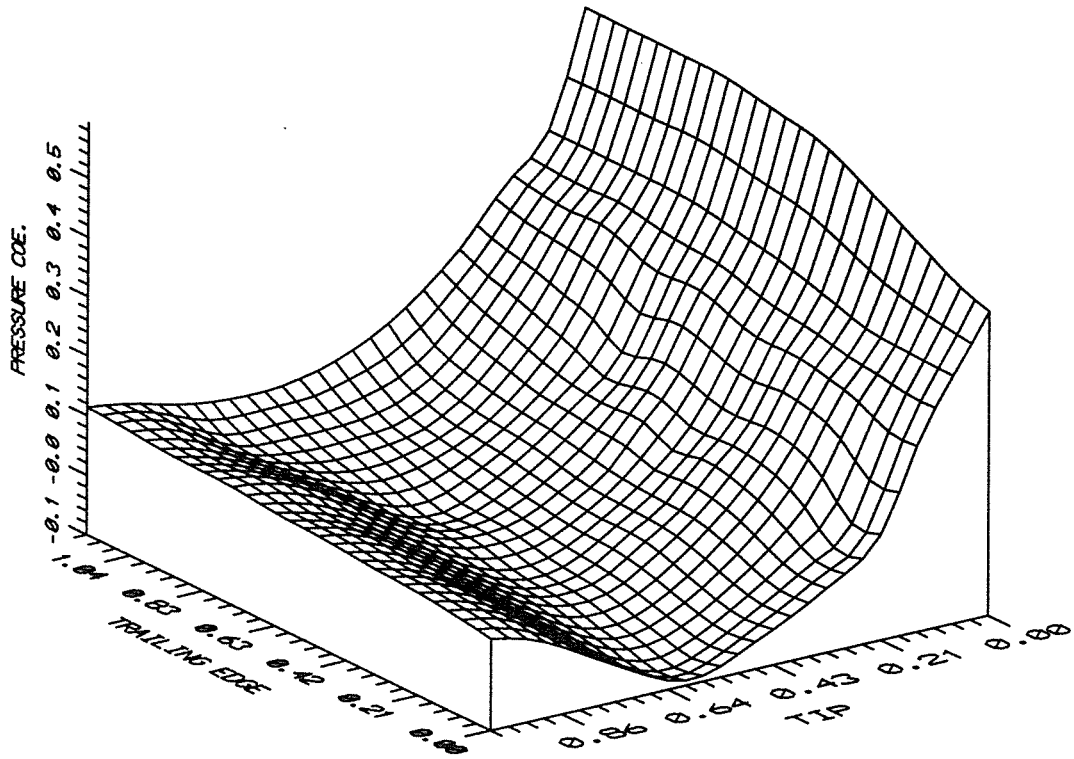

(a)

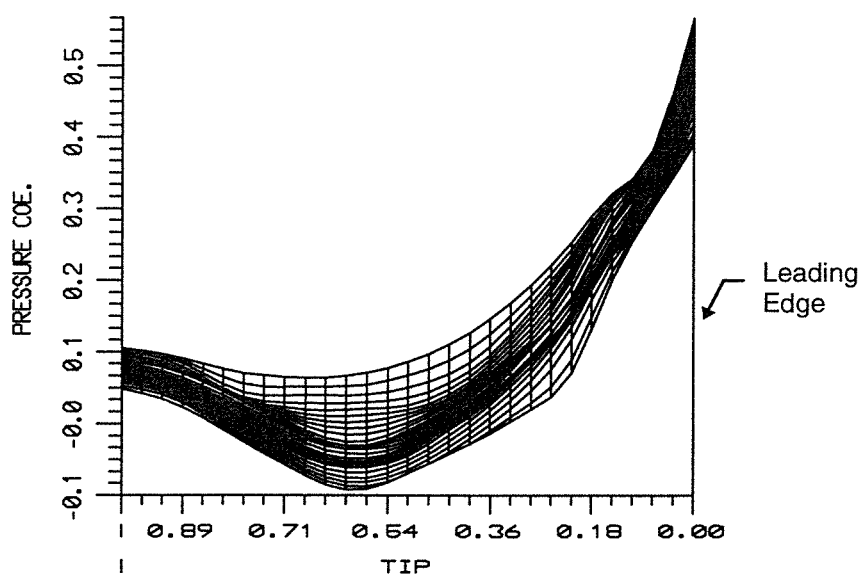

(b)

Figure 4.18 Pressure distribution on the pressure side of the wing with the conventional tip, α=8°. (a) the 3-D view, (b) the tip view.

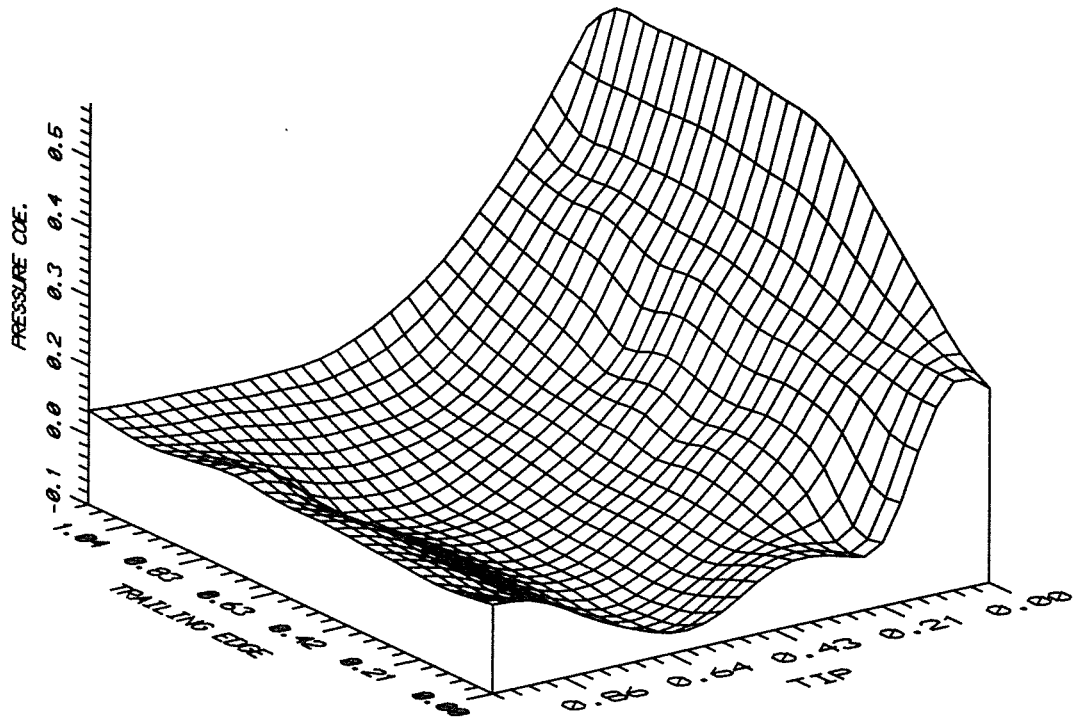

(a)

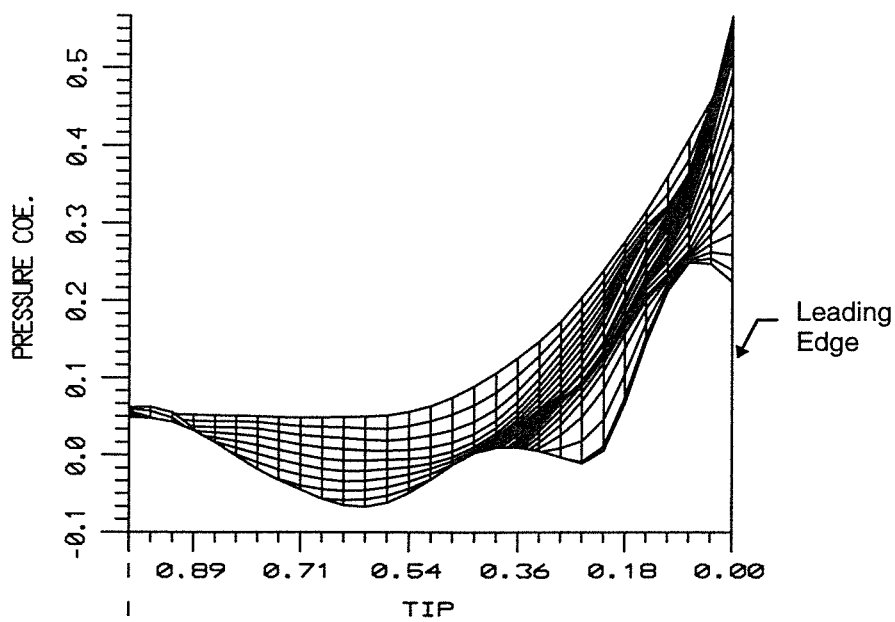

(b)

Figure 4.19 Pressure distribution on the pressure side of the wing with the ducted tip, α=8°. (a) the 3-D view, (b) the tip view.

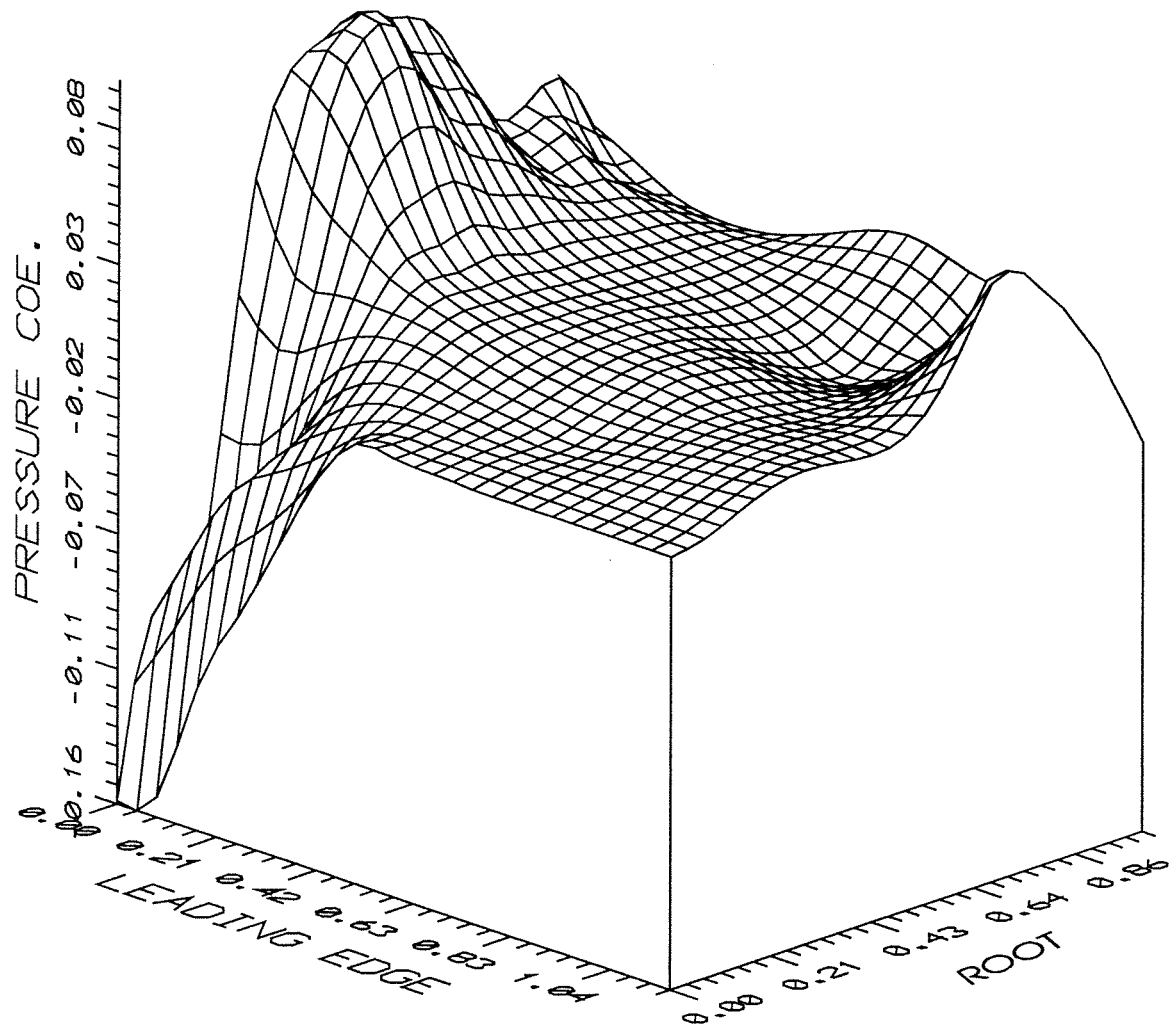

Figure 4.20 The difference between the ducted and conventional tip pressure coefficients on the pressure side of the basic wing, $\alpha = 8°$.

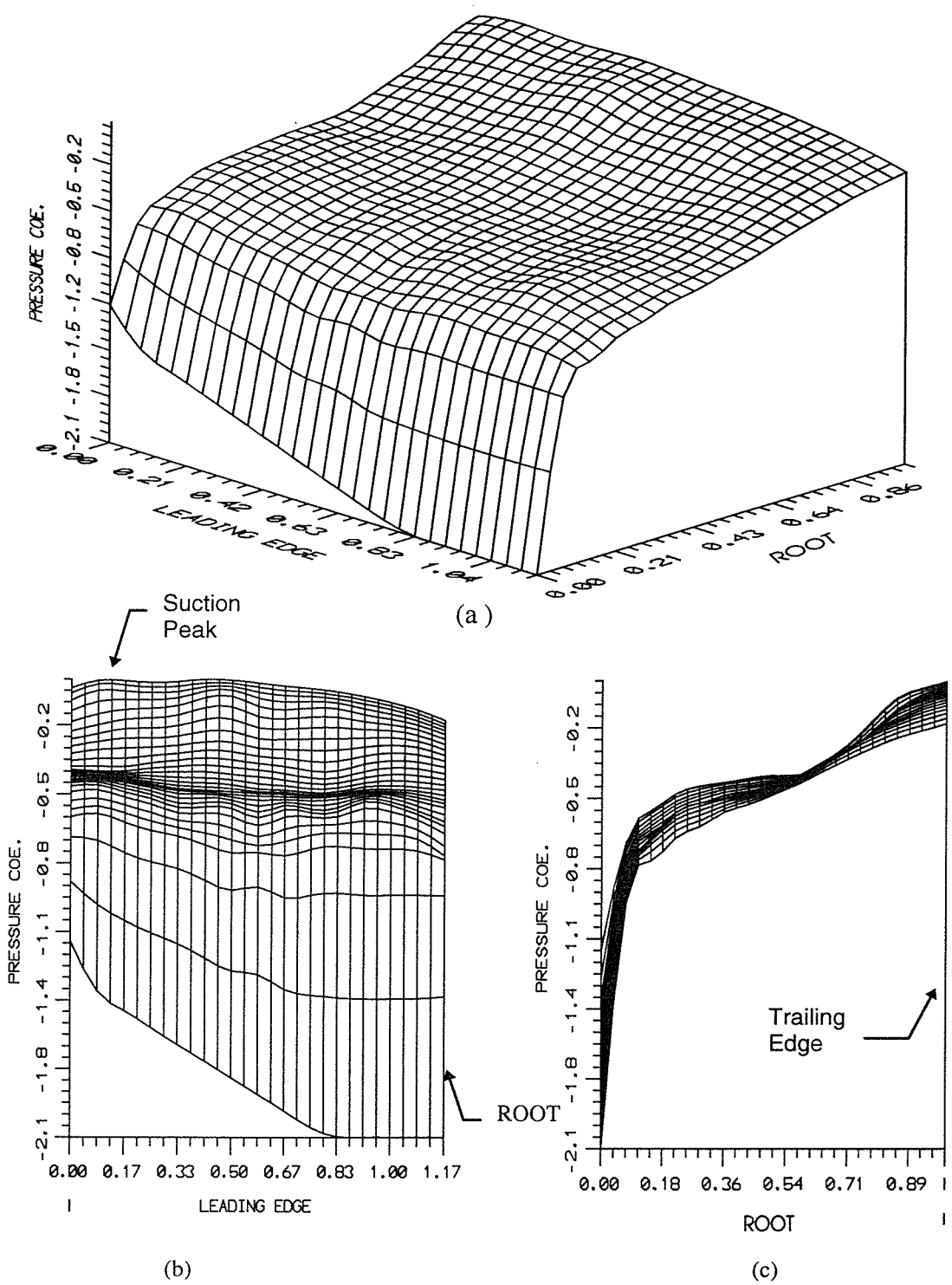

Figure 4.21 Pressure distribution on the suction side of the wing with the conventional tip, α=8°. (a) the 3-D view, (b) the leading edge view, (c) view from the wing root.

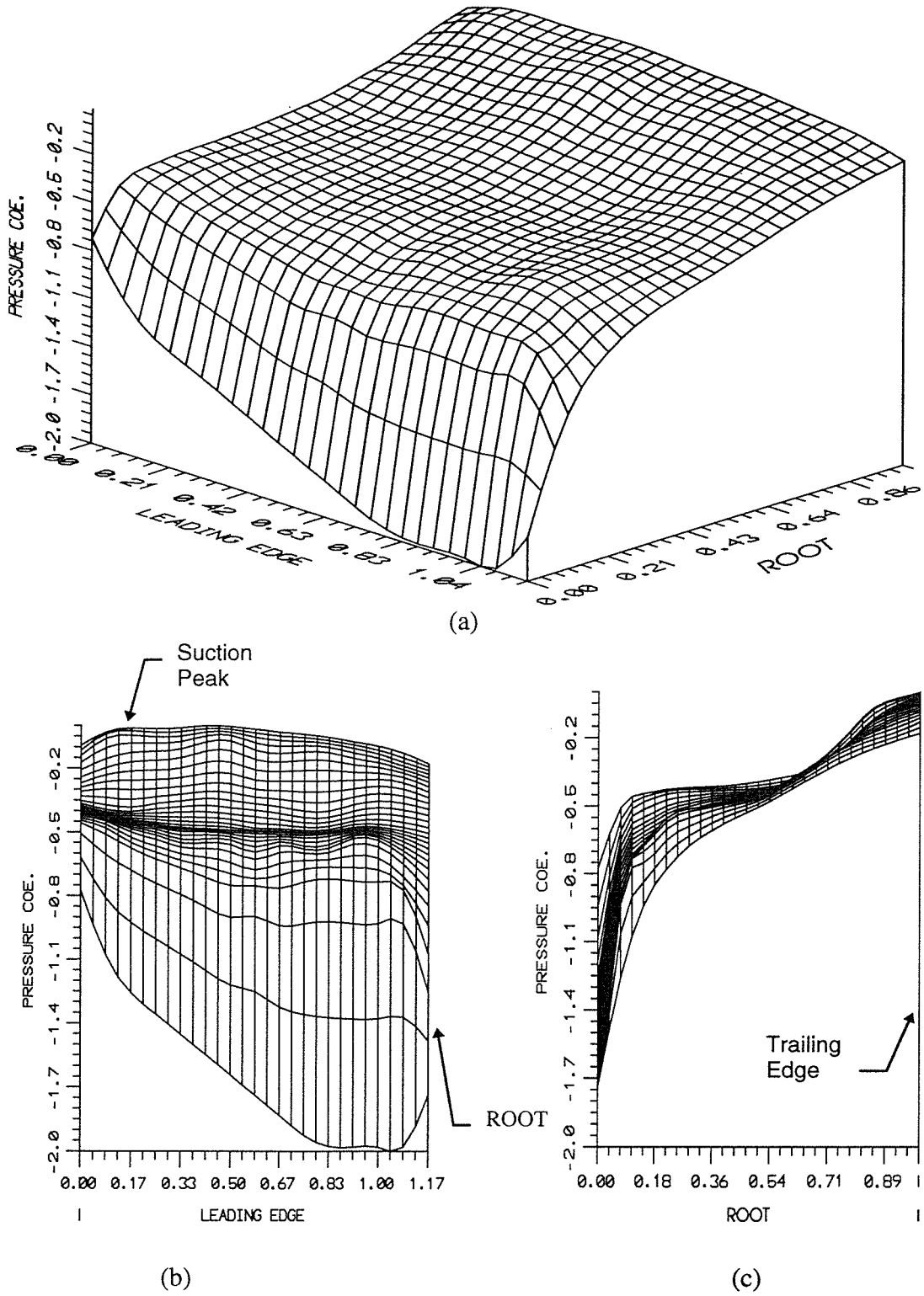

Figure 4.22 Pressure distribution on the suction side of the wing with the ducted tip, α=8°. (a) the 3-D view, (b) the leading edge view, (c) view from the wing root.

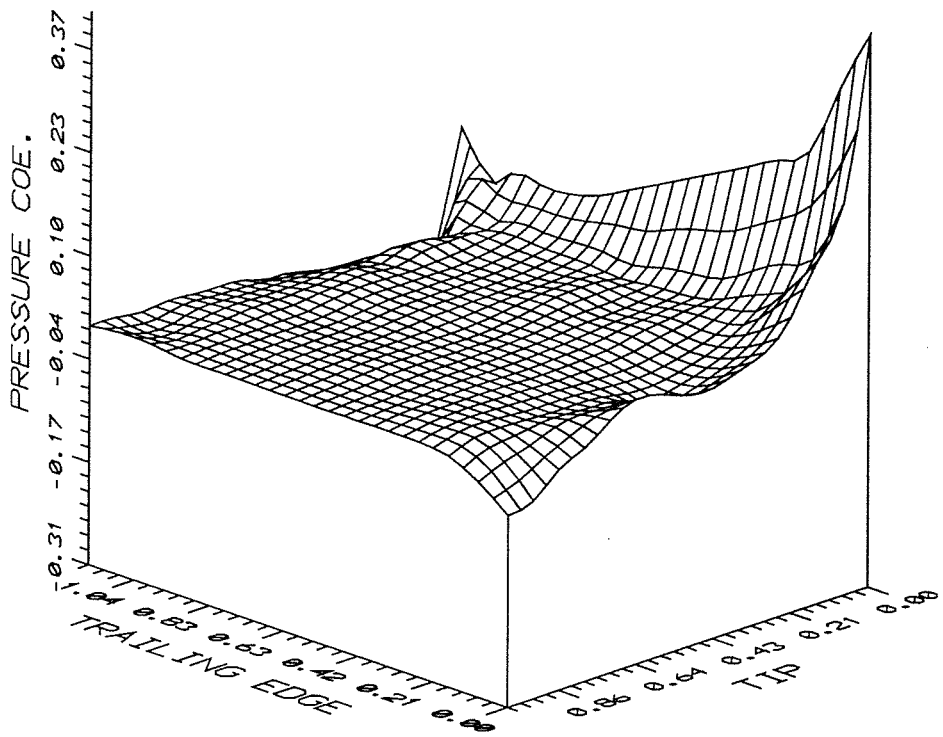

Figure 4.23 The difference between the ducted and conventional tip pressure coefficients on the suction side of the basic wing, $\alpha = 8°$

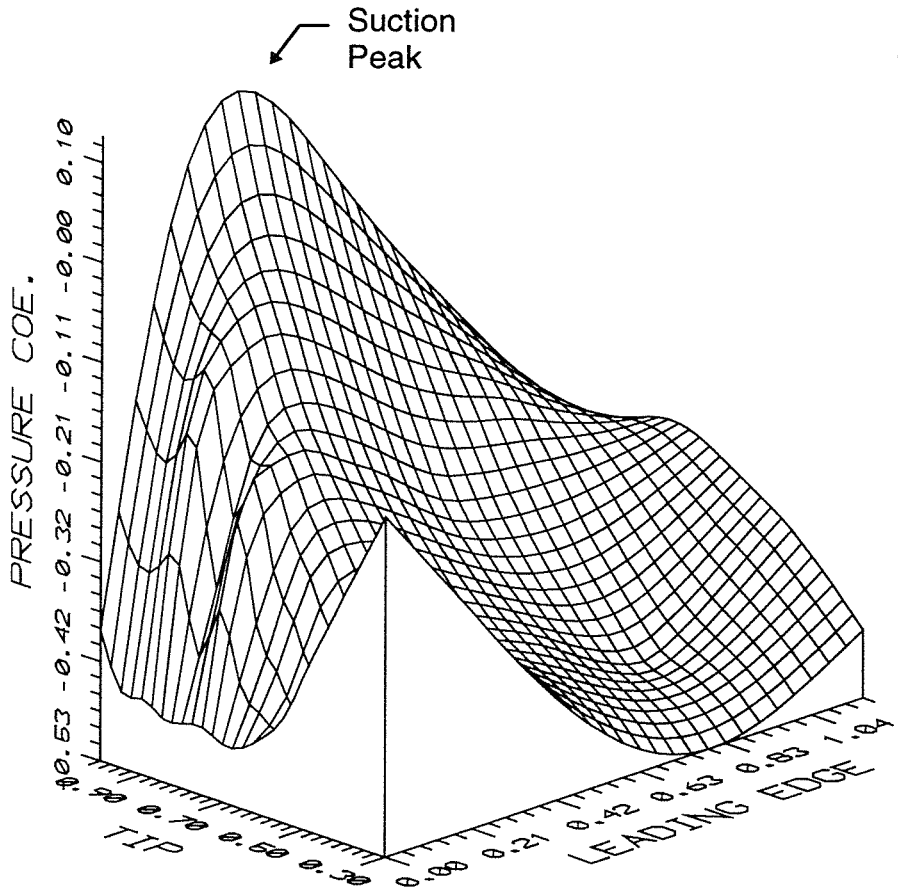

Figure 4.24 Pressure distribution

on the suction side of the basic wing without tip device, $\alpha = 6°$

4.4.3.2 The bi-wing tip

In order to improve the poor lift efficiency of the ducted wing surface, a bi-wing configuration was constructed, which was an improvement over the ducted tip in two respects. One respect was the ease with which the angle of attack of the bi-wing could be varied with respect to the wing chord. Another advantage of the bi-wing tip was that it consists of two smooth lifting surfaces. We chose NACA 64-0006 airfoil sections to build the bi-wing because that airfoil section has good stall characteristics.

Three variants of the bi-wing tip were studied — "underloaded" , "meanloaded" and "overloaded". The "underloaded" bi-wing has a local angle of attack that is less than that of the basic wing, and vice versa for the "overloaded" attachment. Experimental results for two angles of attack show that the underloaded arrangement of the bi-wing tip is the best of the three geometries.

A comparison between bi-wing tip configurations and the simple extended wing tip is shown in Table 4.3. The overload attachment produces a 1.4% increase in lift coefficient due to both the relatively higher angle of attack at the tip and the increased area of the bi-wing structure. The total drag coefficients of the three bi-wing tip configurations were bigger than that of a conventional tip at this angle of attack. At the same angle of attack, as mentioned before, the drag coefficients were virtually identical for the ring wing tip and conventional tip configurations. This difference in performance is due to the existence of sharp edges and corners in the bi-wing tip configuration. Those sharp edges and corners will generate interference vortices and possibly cause local flow separation.

Table 4.3: Comparison of Bi-Wing Tip to Conventional Tip at 8° Angle of Attack.

	C_D		C_L		C_L / C_D	
Conventional Tip	0.0188		0.4699		25.00	
Overload Bi-Wing Tip	0.0234	+24%	0.4767	+1.4%	20.4	-18%
Meanload Bi-Wing Tip	0.0211	+12%	0.4699	0%	22.3	-11%
Underload Bi-Wing Tip	0.0202	+7%	0.4641	-1.2%	23.0	-8%

The total drag coefficient at α=14° was successfully reduced by 4% by using an underloaded bi-wing tip configuration (Table 4.4). This reduction implies that there is an identical drag reduction mechanism for both ring wing tip and bi-wing tip configurations at elevated angles of attack. The higher lift coefficient attained by the bi-wing tips relative to the ducted tip (at α=14°) implies that the rationale for the bi-wing tip design — diminished separation at high α — was valid.

Table 4.4: Comparison of the Bi-Wing Tip to the Conventional Tip at α=14°.

	C_D		C_L		C_L / C_D	
Conventional Tip	0.1140		0.7093		6.22	
Overload Bi-Wing Tip	0.1142	+0.2%	0.7141	+0.7%	6.25	+0.5%
Meanload Bi-Wing Tip	0.1141	+0.1%	0.7021	-1%	6.15	-1%
Underload Bi-Wing Tip	0.1091	-4.4%	0.6949	-2%	6.37	+2.4%

4.5 Experimental Errors and Applicability of the Tip Device

There are several factors that affect the accuracy of lift and drag force measurements. These factors are:

(1). angles of attack;

(2). wind speed in the test section of the wind tunnel;

(3). the electronics in data acquisition system.

The effect of the incident angle can be eliminated by testing different tip devices with the angle of attack fixed. The wind speed in the wind tunnel is measured by a manometer, that reads the pressure difference between the test section and the settling chamber (refer to Figure 4.3) accurately to 0.05mm alcohol. The wind speed can thus be controlled at the testing speed, 30m/s, with an accuracy of better than 0.1%. The data acquisition system collects 10,000 samples within one second. The datum for lift or drag force is the average of those samples. In several minutes, a number of data for each set-up can be obtained. It

was found that lift force can be measured to ±0.5% and drag force to ±1% at elevated angle of attack. All experiments were redone several weeks later to confirm the repeatability of data.

The lift and drag measurements described in this chapter are of high precision (lift typically measured to ±0.5% and drag to ±1% at elevated angle of attack), but fairly low accuracy because of the interaction of the wind tunnel boundary layer with the wing. However, it is known (Green and Acosta 1991) that in the experimental configuration the domain of influence of the wing/wall interaction is confined to a region within 0.2 chords of the wing root. Consequently, it is highly unlikely that modifying the tip geometry would have a significant impact on this interference drag. It is therefore reasonable to argue that although the lift and drag measurements described here are likely to suffer from large errors for any particular wing geometry owing to wind tunnel floor interference, comparison between different wing geometries is valid because this interference effect is nearly constant.

The ring-wing tip modification improves the Lift/Drag performance of a small aspect ratio rectangular planform wing. Therefore, it seems worthwhile to speculate on the potential applications of this device. The most apparent immediate application of this technology is to marine propellers. Marine propellers, which are of small aspect ratio and often operate at high lift coefficients, would benefit from both the superior cavitation behaviour and the improved Lift/Drag ratio of the ring-wing tip. The potential for applying this technology to aircraft wings is much less evident. Aircraft wings commonly operate at a moderate lift coefficient, and have much larger aspect ratios than studied here. Both these factors would mitigate against the installation of ring-wing tips on normal aircraft wings.

4.6 CONCLUSIONS

A novel hydrofoil tip geometry, consisting of a flow-through duct attached to the hydrofoil tip, has been tested for both cavitation inception and lift/drag performance. The principle behind the ducted tip design is to cause the Trefftz-plane shed circulation of the

hydrofoil to take the form of a line with an attached circle, rather than the simple line of a conventional hydrofoil.

The tip vortex inception index of the ducted tip geometry is 50 ± 15% less than that of a conventional tip at normal operating angles (e.g. $\alpha = 7°$), and is at least 30% less for all positive angles of attack. Because the ducted tip hydrofoil shed vorticity has been redistributed relative to the baseline hydrofoil, the induced drag on the hydrofoil should also be reduced. Such a reduction in the induced drag has been observed. For $\alpha > 8°$ the total drag of the ducted tip hydrofoil is less than that of a conventional hydrofoil, despite the fact that the parasite drag of the conventional hydrofoil is less, owing to its much reduced wetted area. The overall lift-drag ratio of the ducted tip hydrofoil, for $\alpha > 8°$, is up to 6 ± 1% greater than that of a conventional tip. Thus, the much improved cavitation behaviour of the ducted tip comes at no cost (for elevated α), and even some benefit, in terms of the hydrodynamic (non-cavitating) performance of the hydrofoil.

The ducted tip geometry is most advantageous when the lifting surface is highly loaded. In practice, propellers on tugs and fishing trawlers are often highly loaded. Studies are presently underway to explore the effectiveness of the ducted tip geometry on such marine propellers.

Chapter 5 Summary and Conclusions

This final chapter is divided into two parts. The first section summarizes the "quasi-similarity" methodology and conclusions. The second section makes some suggestions for future work.

5.1 Summary and Conclusions

A wing tip vortex was studied both analytically and experimentally. In the analytical work, a new method was developed that describes the tip vortex structure from far downstream to a downstream distance fairly close to the vortex-generating wing. Wing drag is the key parameter affecting the tip vortex structure. In the experimental work, a hydrofoil with a novel ducted tip device was found to have superior cavitational and aerodynamic performance over a conventional rounded tip configuration. This section is divided into three sub-sections: analytical method, tip vortex structure and wing tip modification.

5.1.1 Analytical method

A new analytical method, referred to as the "quasi-similarity" method, has been developed for modelling vortices in a freestream. The new approach combines a polynomial solution with the similarity variable technique. By using this method, the non-linear partial differential governing equations are reduced to sets of ordinary differential equations. The fundamental idea of the "quasi-similarity" method can be applied to a broad range of non-linear problems that cannot be described by self-similar solutions.

The "quasi-similarity" method is used here to model wing tip vortex flow. It provides the first non-linear analytical wing tip vortex model. In this new method, each resulting set of ordinary differential equations describes the flow with varying degrees of faithfulness. The first order set of ODEs gives solutions that are second order accurate in the axial variable z; higher order sets of ODEs provide higher order accuracy. Fortunately,

the first order terms of the solution polynomial can be obtained analytically in complete function form. The second order tangential velocity component and pressure distribution are also obtained in complete function form. Other higher order terms must be calculated numerically by solving a set of ODEs with appropriate boundary conditions.

There are three major assumptions of the quasi-similarity method. These assumptions are:

(1). the axial velocity deficit or excess in tip vortices is not significantly greater than the freestream velocity;

(2). the vortex circulation remains constant with downstream distance;

(3). the flow is laminar.

The first limitation can be expressed mathematically (assuming a rectangular wing) as

$$z > C_D \cdot \mathrm{Re}_c \cdot S/16\pi$$

where z is the downstream distance, C_D is the wing total drag coefficient, Re_c is the Reynolds number based on the wing chord, and S is the span of the wing. This distance is about a hundred meters downstream of the wing trailing edge for a typical drag coefficient $C_D \approx 0.01$, Reynolds number $\mathrm{Re}_c \approx 5\times10^5$, and a one meter span wing (for which the flow should be laminar). The second assumption is a reasonable one after the vortex roll-up is complete. Therefore, very near the wing the first two conditions may not apply. The flow in a practical trailing vortex is usually turbulent, at least near the wing, due to large Reynolds number. This theory is still valid for a turbulent flow only if an eddy viscosity model is used and the eddy viscosity is a constant everywhere in the flow.

5.1.2 Tip vortex structure

All three velocity components in tip vortices decrease with increasing downstream distance at fairly large downstream distance of the vortex-generating wing. The radial velocity diminishes most rapidly, followed by the axial velocity. The tangential velocity decays most slowly. This prediction is consistent with many experimental observations.

At a fairly large distance downstream of the wing, only an axial velocity deficit can exist for a wing experiencing a positive drag force. An axial velocity excess can exist far downstream of a wing generating thrust (e.g. with wing tip-mounted engines).

A unique and important feature of the quasi-similar wing tip vortex model is that the predicted drag on a vortex-generating wing due to a single quasi-similar tip vortex is finite. To the author's knowledge, no other vortex model has this property.

The tangential velocity component and pressure of the first order quasi-similarity solution are exactly the same as those in an advanced linear tip vortex model (Batchelor 1964). The axial velocity field of the linear vortex model differs from that of the quasi-similarity model. This discrepancy in the axial velocity causes a single vortex in the linear model to have an infinite drag whereas the quasi-similar model indicates a finite drag.

The axial velocity and tangential velocity predicted by quasi-similarity theory have been compared with experimental measurements. The agreement is good at large downstream distances from a wing. The experimental results confirm that the axial velocity deficit on the vortex centerline decays as the reciprocal of the downstream distance; the tangential velocity in a tip vortex is proportional to the inverse square root of the downstream distance.

5.1.3 Wing tip modification

A novel ducted tip device has been tested in a wind tunnel and a water tunnel. Aerodynamic and cavitation performance of the ducted tip has been compared with that of a conventional rounded tip.

The ducted tip has up to 6% better Lift/Drag performance than a square cut wing tip* of equal span at higher angles of attack, roughly 8° or more. The principal cause of these performance improvements is the greatly reduced induced drag afforded by the ducted tip at high lift coefficients, which more than offsets the increase in parasitic drag resulting from the increased wetted area.

---

* Experimental data show that a square cut wing has similar aerodynamic performance to a rounded tip wing. The difference between those two conventional tip configurations is within experimental error.

The tip vortex cavitation inception index of the ducted tip geometry is at least 33% lower than that of a conventional rounded hydrofoil tip at all positive angles of attack.

No pressure distribution difference between tip geometries was observed over the majority of the wing surface (differences from one tip geometry to another were less than the experimental error, which is about 7%). However, near the wing tips the pressure distribution was significantly modified by the addition of tip devices. The pressure measurements are not accurate enough to confirm the Lift/Drag ratio improvement, but they are supportive of the cavitation results — tip vortex cavitation is significantly modified by the ducted tip, whereas leading edge cavitation is not significantly affected by addition of the tip device.

The ducted tip is effective at reducing the tip vortex inception index and the vortex induced drag. This tip design spreads the shed vorticity in the transverse plane behind the wing (Trefftz plane) over a line and circle, while a conventional wing tip spreads the vorticity only over a line.

The vastly reduced tip cavitation index, together with the improved Lift/Drag performance, suggests there is a significant role for the ducted tip device in both military and civilian marine propeller design.

5.2 Suggestions for future work

A careful experiment should be designed in order to further verify the quasi-similarity vortex model. The wing total drag and vortex circulation should be measured accurately in a direct or indirect way with the Reynolds number maintained low enough that the vortex flow is laminar.

Application of the "quasi-similarity" method to other non-self-similar problems could be possible. In fact, jets with a tangential velocity component (twisted jets) were studied in detail by Loitsyanski (1966) and Goldshtik et al. (1979 and 1986). They employed a non-similar power series to construct their analytical solutions. However, twisted jets are different from wing tip vortices. The swirling jets are characterized by the following conservation integrals: flowrate, axial momentum and angular momentum. In contrast,

the tip vortices are characterized by a freestream velocity, and the conservation of vortex circulation and axial momentum. Related problems, for instance, jet flows (with or without swirl) in a freestream seem amenable to treatment using the quasi-similarity technique.

A different set of polynomials, with an amplitude function proportional to z^i instead of the $1/z^i$ used in the theory developed in this thesis, is a possible solution of the simplified governing equation (2.1.1). This amplitude function has the general feature of vortex rollup — the magnitude of velocity components increases with increasing downstream distance. Is this a solution pertinent to the roll up of the wing tip vortex? Are there any physical problems related to the new polynomial solution? Further investigations are needed.

Instability of a trailing line vortex has attracted great interest in recent years. Some of the stability studies based on Batchelor's partly-linearized theory include works by Stewartson and Capell (1985), Stewartson and Brown (1985), Mayer and Powell (1992b), and Duck et al. (1992). The results in this thesis may prompt studies of the effect of wing drag on the stability of a single tip vortex, and the non-linear effect on tip vortex instability.

The potential for applying the novel ducted tip to aircraft wings is quite small, because aircraft wings commonly operate at moderate lift coefficients and have much larger aspect ratios than studied here. The most apparent immediate application of ducted tips is to marine propellers. Marine propellers, which have small aspect ratio and large operating angles of attack, would benefit from both the superior cavitation performance and the improved Lift/Drag ratio of a ducted tip. Future work should concentrate on further improving the tip geometry and establishing whether the ducted tip has a practical marine application.

Bibliography

Arakeri, V.H., Sharma, S.D., and Mani, K., 1985, "A Technique to Delay the Inception of Tip Vortex Cavitation from Marine Propellers," ASME Cavitation and Multiphase Flow Forum.

Arndt R. E. A. and Keller A. P., 1992, "Water Quality Effects on Cavitation Inception in a Trailing Vortex," J. Fluid Eng. Vol. 114, pp. 430-438.

Arndt R. E. A., Arakeri V. H. and Higuchi H., 1991, "Some Observations of Tip-Vortex Cavitation," J. Fluid Mech. vol.229, pp. 269-289.

Baber, M.R. et al., 1975, "Flight Test Investigation of the Vortex Wake Characteristics Behind a Boeing 727 During Two — Segment and Normal ILS Approaches", NASA TM X-62,398.

Baker, G.R., Barker, S.J., Bofah, K.K., and Saffman, P.G., 1974, "Laser Anemometer Measurements of Trailing Vortices in Water", J. Fluid Mech., Vol. 65, Part 2, pp. 325-336.

Bandyodpadhyay, P.R., Stead, D.F., and Ash, R.L., 1990, "The Organized Nature of a Turbulent Trailing Vortex", 21st Fluid Dynamics, Plasma Dynamics And Lasers Conference, Seattle,Wa.

Barnett R. A. and Ziegler M. R., 1991, Applied Mathematics, Dellen Macmillan.

Batchelor, G.K., 1964, "Axial Flow in Trailing Line Vortices", J. Fluid Mech., Vol. 20, Part 4, pp. 645-658.

Benjamin, T. B., 1962, "Theory of the Vortex Breakdown Phenomenon." J. Fluid Mech. 14, pp.593-629.

Betz, A., 1933, "Behavior of Vortex Systems", NACA TM 713.

Burgers J. M., 1948, "A Mathematical Model Illustrating the Theory of Turbulence", Advances in Applied Mechanics, pp.171-196.

Carlin, G., Dadone, L. and Spencer, R., 1989, " Results of an Experimental Investigation of Blade Tip Vortex Modifcation Devices", NASA CR-181853.

Chahine G. L. Frederick G. F. and Bateman R. D., 1993, "Propeller Tip Vortex Cavitation Suppression Using Selective Polymer Injection," J. Fluids Eng. vol. 115, pp. 497-503.

Chigier, N.A. and Corsiglia, V. R., 1972, "Wind Tunnel Studies of Wing Wake Turbulence", AIAA #72-41.

Chow, J. S., Zilliac, G. G. and Bradshaw, P., 1993, "Measurements in the Near-Field of a Turbulent Wing Tip Vortex", AIAA-93-0551.

Ciffone, D. L., and Orloff, K. L., 1974, "Axial Flow Measurement in Trailing Vortices," AIAA Journal, Vol.12, No.8, pp.1154-1155.

Cone, C.D., 1963, "The Theory of Induced Lift and Minimum Induced Drag of Non Planar Lifting Systems," NASA Technical Report, R-139, N63 16288.

Corsiglia, V. R., Schwind , R. G. and Chigier, N. A., 1973, "Rapid Scanning, 3-D Hot-Wire Anemometer Surveys of Wing — Tip Vortices," Journal of Aircraft, Vol.10, No.12, pp.752-757.

Critchley, J.B., 1991, "Wake Vortex — The Program in the United Kingdom," Proceedings of the FAA Wake Vortices Conference, Washington, D.C.

Crow, S. C., 1970, "Stability Theory for a Pair of Trailing Vortices", AIAA Journal, Vol. 8, No. 12, pp.2172-2179.

Devoss, D., 1986, "The Race To Recover The Cup," Los Angeles Times Magazine, Aug. 31, pp. 9+.

Donaldson, C. and Bilanin, A. J., 1975, "Vortex Wakes of Conventional Aircraft", AGARD-AG-204.

Donaldson, C. du P. and Sullivan, R. D., 1970, "In Aircraft Wake and Its Detection," Plenum, New York, p389.

Donaldson, C., 1971, "A Brief Review of the Aircraft Trailing Vortex Problem", AFOSR TR-71-1910.

Duck, P.W. and Khorrami M. R., 1992, "A Note on the Effects of Viscosity on the Stability of a Trailing-Line Vortex," JFM, vol. 245, pp.175-189.

El-Ramly, Z., and Rainbird, W. J., 1977, "Flow Survey of the Vortex Wake Behind Wings." Journal of Aircraft, Vol.14, No.11, pp.1102-1108.

Eliason, B. G., Gartshore, I.S. and Parkinson, G. V., 1975, "Wind Tunnel Investigation of Crow Instability." J. Aircraft 12, pp.985-988.

Falcao de Campos, J.A.C., George, M.F., and MacKay, M., 1989, "Experimental Investigation of Tip Vortex Cavitation for Elliptical and Rectangular Wings," ASME Cavitation and Multiphase Flow Forum, La Jolla, California.

Flechner, S.G., Jacobs, P.F. and Whitcomb, R.T., 1976, "A High Subsonic Speed Wind Tunnel Investigation of Winglets on a Representative Second Generation Jet Transport Wing" , NASA TN D-8264.

Fruman D. H., Cerrutti P., Pichon T. and Dupont P., 1995, "Effect of Hydrofoil Planform on Tip Vortex Roll-up and Cavitation," J. Fluids Eng., vol. 115, pp. 162-169.

Fruman, D.H., Dugue, C. and Cerruti, P., 1991, "Tip Vortex Roll-up and Cavitation," ASME Cavitation and Multiphase Flow Forum, Portland, Oregon.

Gartshore, I. S., 1963, "Some Numerical Solutions for the Viscous Core of an Irrotational Vortex," NRC Can. Aero. Rep. LR-378.

Goldshtik M. A., 1979, "On Twisted Jets", Izv. Akad. Nauk. SSSR, MzhG, 1.

Goldshtik, M. A. and Yavorskii, N. I., 1986, "On Submerged Jets." PMM USSR, Vol.50, No. 4, pp.438-445.

Gorsigtlia, V.R., Schwing, R.G. and Chigier, N.A., 1973, "Rapid Scanning, Three Dimensional Hot-Wire Anemometer Surveys of Wing Tip Vortices", J. Aircraft, Vol. 10, No. 12, pp. 752-757.

Govindaru, S.P. and Saffman, P.G., 1971, "Flow in a Turbulent Trailling Vortex", Physics Of Fluid, Vol.14, Number 10, Oct. 1971, pp. 2074-2080.

Green, S. I., 1988, "Tip Vortices — Signle Phase And Cavitating Flow Phenomena", Ph.D. Thesis, California Institute Of Technology, Report No. Eng. 183.17.

Green, S. I. and Duan, S. Z., 1995, "The Ducted Tip — A Hydrofoil Tip Geometry with Superior Cavitation Performance," accepted by the ASME Journal of Fluids Engineering.

Green, S. I. and Acosta, A.J., 1991, "Unsteady Flow in Trailing Vortices," Journal of Fluid Mechanics, Vol. 227, pp. 107-134.

Green, S. I., 1991, "Correlating Single Phase Flow Measurements with Observations of Trailing Vortex Cavitation," Journal of Fluids Engineering, Vol. 113, No. 1, pp. 125-129.

Green, S. I., 1994, "Wing Tip Vortices," to appear in Fluid Vortices, S. Green (ed.), Kluwer, Dordrecht.

Green, S. I., Acosta, A.J. and Akbar, R., 1988, "The Influence of Tip Geometry on Trailing Vortex Rollup and Cavitation," ASME Cavitation and Multiphase Flow Forum, Cincinnati, Ohio.

Green. S. I., 1987, "Three Tip Vortex Examination Techniques", International Symposium on Cavitation Research and Techniques, pp. 155-160.

Hall, H.W., Arndt, R.E.A. and Billit, M.L., 1972, " Limited Cavitation and the Related Scale Effects Problem", JSME Proc. 2nd Int. Symp. Fluid Mechanics And Fluidics, Tokyo, pp. 303-314.

Hastings, E.C. Patterson, J.C., Shanks, R.E., Champine, R.A., Copeland, W.L., and Young, D.C., 1975, "Development and Flight Tests of Vortex Attenuating Splines", NASA TN D- 8083.

Higuchi, H, Quadrelli, J.C. and Farell C., 1986, "Vortex Rollup From an Elliptical Wing at Moderately Low Reynolds Numbers", AIAA #86-0562.

Hoeijmakers, H.W.M., 1983, "Computational Vortex Flow Aerodynamics", AGARD Conference Proceedings #342, pp.18.1-18.35.

Hoffmann, E.R., and Joubert, P. N., 1963, "Turbulent Line Vortices," Journal of Fluid Mechanics, Vol.16, pp.395-411.

Huang, T., 1987, David Taylor Naval Ship Research And Development Center, Personal Communication.

Ikohagi, T., Higuchi, H. and Avndt, R.E.A., 1986, "The Structure of Trailing Vortices", In Advancement In Aerodynamics, Fluid Mechanics And Hydraulics, Joint AIAA, ASME And ASCE Symposium, Univ. of Minnesota.

Chow, J. S., Zilliac, G. G. and Bradshaw, P., 1991, "Initial Roll Up of a Wing Tip Vortex", Personal Communication.

Kaden, H., 1931, "Aufwickling einer unstabilen unstetigkeitsflache", Ing. Arch. 2, 140. (English translation, R. A., Library translation no. 403)

Kantha, H.L., Lewellen, W.S. and Durgin,F.H., 1971, "Qualitative Responses of a Vortex Core to Tip Blowing and Intersecting Airfoils", ASRL TR 153-4.

Katz, J. and Galdo, J. B., 1989, "The Effect of Roughness on Rollup of Tip Vortices on a Rectangular Hydrofoil." J. Aircraft 26, pp.247-253.

Kuiper, G., 1981, Cavitation Inception on Ship Propellor Models, M. Veenamnen Zonen B.V. Wageningen, pp. 130-159.

Lessen, M. and Paillet, F., 1974b, "The Stability of a Trailing Line Vortex, Part 2, Viscous Theory", J. Fluid Mech., 65, pp.769-779.

Lessen, M., Singh, P. J. and Paillet, F., 1974a, "The Stability of a Trailing Line Vortex, Part 1, Inviscid Theory", J. Fluid Mech., 63, pp.753-763.

Lewy, S. and Caplot, M., 1982, "Theoretical and Experimental Study of Helicopter Rotor Noise", ONERA TP 1982-74.

Lignueul P. and Latorre R., 1993, "Study of Nuclei Distribution and Vortex Diffusion Influence on Nuclei Capture by a Tip Vortex and Nuclei Capture Noise," J. Fluid Eng, vol. 115, pp. 504-507.

Logan A. H., 1971, "Vortex Velocity Distributions at Large Downstream Distance", J. Aircraft, vol.8, No. 11. pp.930-932.

Loitsyanski, L. G., 1966, "Mechanics of Fluids and Gases." Oxford University Press.

Long, R. R., 1961, "A Vortex in an Infinite Viscous Fluid", J. Fluid Mech., 11, pp.611-624.

Mager, A., 1972, "Dissipation and Breakdown of a Wing-Tip Vortex", J. Fluid Mech. 55, pp.609-628.

Maines, B.H. and Arndt, R.E.A., 1993, "Bubble Dynamics of Cavitation Inception in a Wing Tip Vortex," ASME Cavitation and Multiphase Flow Forum, Washington, D.C.

Martin, R.M., Elliott, J.W., and Head, D.R., 1984, "Comparison of Experimental and Analytical Predictations of Rotor Blade Vortex Interactions Using Model Scale Acoustic Data", AIAA #84-2269.

Mason, W.H. and Marchman J. F., 1972, "Far Field Structure of an Aircraft Trailing Vortex, Including Effects of Mass Injection", NASA CR-62078.

Mayer, E. W. and Powell, K. G., 1992a, "Similarity Solutions for Viscous Vortex Cores," JFM, vol.238, pp.487-507.

Mayer, E. W. and Powell, K. G., 1992b, "Viscous and Inviscid Instabilities of a Trailing Vortex", JFM, vol. 245, pp.91-114.

McCormick, B.W., 1962, "On Cavitation Produced by a Vortex Trailing from a Lifting Surface," ASME Journal of Basic Engineering, pp. 369-379.

McCormick, B.W., Tangler, J. L., and Sherrieb, H. E., 1968, "Structure of Trailing Vortices," Journal of Aircraft, Vol.5, No.3, pp.260-267.

Milne-Thomson, L.M., 1958, Theoretical Aerodynamics, Dover, New York.

Moordzij, L., 1977, "A Note on the Scaling of Tip Vortex Cavitation Inception", International Shipbuilding Progress, No. 24, pp. 233-236.

Moore, D. W. and Saffman, P. G., 1973, "Axial Flow in Laminar Trailing Vortices," Proceedings of the Royal Society of London, Series A. Vol.333, pp.491-508.

Moore, D.W., 1974, "A Numerical Study of the Rolling Up of a Finite Vortex Sheet", J. Fluid Mech., Vol. 63., Part 2, pp. 225-235.

Moore, D.W. and Saffman, P.G., 1973, " Axial Flow in Laminar Trailing Vortixes", Proc. Rey. Soc. Lond. A. Vol. 333, pp. 491-508.

Mosher, M. and Peterson, R.L., 1983, "Acoustic Measurements of a Full-Scale Coaxial Helicopter". AIAA #83 -0722.

Olsen, J.H., 1971, "Results of Trailing Vortex Studies in a Towing Tank", Publ. In "Aircraft Wake Turbulence and Its Detection", Ed. By J.H. Olsen et al. Plenum Press, New York, pp. 455.

Ooi, K.K., 1981, "Scale Effects on Cavitation Inception in Submerged Jets", Ph.D. Thesis, California Institute Of Technology, Report No. 183-6.

Orloff, K.L. and Grand, G.R., 1973, "The Application of a Scannig Laser Doppler Velocimeter to Trailing Vortex Definition and Alleviation", AIAA #73-680.

Oseen, C. W., 1912, Über wirbelbewegung ineiner reibenden flüssigkeit, Art. f. Mat. Astron. Fys. 7.14.

Pauchet, A., Briancon-Marjollet, L. and Fruman, D.H., 1993, "Recent Results on the Effect of Cross-Section on Hydrofoil Tip Vortex Occurrence at High Reynolds Numbers," ASME Cavitation and Multiphase Flow Forum, Washington, D.C.

Peckham, D. H. and Atkinson, S. A. 1957, "Preliminary Results of Low Speed Wind Tunnel Test on a Ghotic Wing of Aspect Ratio 1.0", British Aeronaut. Res. Council, CP508.

Phillips W., 1981, "Turbulent Trailing Vortex During Roll Up", Journal of Fluid Mechanics, Vol. 105, pp.451-467.

Platzer, G.P. and Souders, W.G., 1979, "Tip Vortex Cavitation Delay with Application to Marine Lifting Surfaces — A Literature Survey," DTNSRDC Report 79/051.

Poling, D.R., Dadone, L. and Telionis, D.P., 1989, "Blade-Vortex Interaction," AIAA Journal, Vol. 27, No. 6, pp. 694-699.

Prandtl, L., 1920a, "Theory of Lifting Surface Part I" , NACA TN #9.

Prandtl, L., 1920b, "Theory of Lifting Surface Part II", NACA TN #10.

Raines, D.A., 1954, " Tip Clearance Flows in Axial Compressors and Pumps", Report M.E.-5, Jet Propulsion Center, California Institute Of Technology.

Ruden, P., 1974, " Investigation of a Single Stage Axial Fan" , NACA TM-1062.

Sarpkaya, T., 1983, "Trailing Vortices in Homogeneous and Density Stratified Media", J. Fluid Mechs., Vol. 136, pp. 85-109.

Sarpkaya, T., 1992, "Interaction of a Turbulent Vortex With a Free Surface", Nineteenth Symposium On Naval Hydrodynamics. Seoul, Korea.

Sarpkaya, T. and Daly, J. J., 1987, "Effect of Ambient Turbulence on Trailing Vortices." J. Aircraft 24, pp.399-404.

Scheiman, J. and Shivers, J., 1971, "Exploratory Investigation of the Structure of the Tip Vortex of a Semispan Wing for Several Wing Tip Modifcation", NASA TN D-6101.

Sharma, S. D., Mani, K and Arakeri, V. H., 1990, "Cavitation Noise Studies on Marine Propellers," Journal of Sound and Vibration, Vol .138, No. 2, pp. 255-283.

Shekarriz, A., Fu, T.C., Katz, J., Liu, H.L. and Huang, T.T., 1992, "Study of Junction and Tip Vortices Using Particle Displacement Velocimetry," AIAA Journal, Vol. 30, No. 1, pp. 145-152.

Shekarriz, A., Fu, T. C. and Katz, J., 1993, "Near-Field Behavior of a Tip Vortex", AIAA J., vol. 31, No. 1, pp.112-118.

Shevell, R. S., 1989, Fundamentals of Flight, Prentice-Hall, p154.

Snedeker, R.S., 1972, "Effect of Air Injection on the Torque Produced by a Trailing Vortex", J. Aircraft. Vol. 9, No. 9, pp. 682-686.

Sounders, W.G. and Platzer, G.P., 1981, "Tip Vortex Cavitation Characteristics and Delay of Inception on a Three Dimensional Hydrofoil," David Taylor Maval Ship Research And Development Center, Rep. No. 81/007.

Spillman, J., 1978, "The Use of Wing Tip Sails to Reduce Vortex Darg", Aeronautical J., pp. 387-395.

Spivey, W.A., Morehouse, G.G., 1970, "New Insights into the Design of Swept Tip Rotor Blades", 26th Annual National Forum Of The American Helicopter Society.

Sponagle, N.C. and Leggat, L. J., 1984, "The Spatial Distribution of Acoustic Sources at Propellor Vortex Cavitation Inception", ASME International Symposium On Cavitation Inception, pp.191-198.

Srinvivasan, G.R. McCrosky, W.J., Baeder, F.D. and Edwards, T.A., 1980, "Numerical Simulation of Tip Vortices of Wings in Subsonic and Transonic Flows", AIAA Journal, Vol. 26, Number 10, pp. 1153-1162.

Stewartson K. and Brown S. N., 1985, "Near-Neutral Centre-Modes as Inviscid Perturbations to a Trailing Line Vortex," JFM, vol.156, pp.387-399.

Stewartson, K. and Capell, K., 1985, "On the stability of Ring Modes in a Trailing Line Vortex: the Upper Neutral Points," JFM, vol. 156, pp.369-386.

Stinebring, D.R., Farrell, K.J. and Billet, M.L., 1989, "The Structure of a Three-Dimensional Tip Vortex at High Reynolds Number," 22nd American Towing Tank Conference, St. John's, Newfoundland.

Stinebring, D.R., Farrell, K.J. and Billet, M.L., 1991, "The Structure of a Three-Dimensional Tip Vortex at High Reynolds Number," Journal of Fluids Engineering, Vol. 113, No. 3, pp. 496-503.

Summa, J.M., 1982, "Advanced Rotor Analysis Methods for the Aerodynamics of Vorex/Blade Interactions in Hover", Association Aeronautique et Astro-nautiqe de France, 8th European Rotorcraft Forum.

Takami, H., 1964, " A Numerical Experiment with Discrete Vortex Approximation with Reference to the Rolling Up of a Vortex Sheet", Stanford University, SUDAER 202.

Thompson, D. H., 1975, "Experimental Study of Axial Flow in Wing Tip Vortices", J. Aircraft, vol.12, No. 11, pp. 910-911.

Trigub, V. N., Blokhin, A. B. and Simakin, I. N., 1994, "The Asymptotic Study of Dissipation and Breakdown of a Wing-Tip Vortex", J. Fluid Mech., Vol.274, pp.293-337.

Vaczy, C.M. and McCormick, D.C., 1987, "A Study of the Leading Edge Vortex and Tip Vortex on Prop-Fan Blades", J. Turbomachinery, Vol. 109, pp. 325-331.

Vortex Wake Alleviation Workshop, 1980, NASA Langley Research Center, Hampton, VA.

Webber, G.W. and Dansby, T., 1983, "Wing Tip Devices for Energy Conservation and Other Purposes — Experimental and Analytical Work in Progress at the Lockheed-Georgia Company," Canadian Aeronautics and Space Journal., Vol. 29, No. 2, pp. 105-120.

Westwater, F.F., 1935, "Rolling Up of the Surface Discontinuity behind an Aerofoil of Finite Space" , Aero. Res. Counc. R. And M. # 1962.

Whitcomb, R.T., 1976, "A Design Approach and Selected Wind Tunnel Results at High Subsonic Speed for Wingtip Mounted Winglets", NASA TN D-8260.

Widnall, S.E. and Wolf, T.L., 1980, "Effect of Tip Vortex Structure on Helicopter Noise due to Blade Vortex Interaction", J. Aircraft, Vol. 17, pp. 705-711.

William, G. M., 1974, "Viscous Modeling of Wing-generated Trailing Vortices," Aeronautical Quarterly, Vol.25, pp.143-154.

Winter, H., 1991, "R and D for a Wake Vortex Warning System in Germany," Proceedings of the FAA Wake Vortices Conference, Washington, D.C.

Zalay, A.D., 1976, "Hot Wire and Velocity Meter Wake Vortex Surveys", AIAA J., Vol. 15, No.5, pp. 694-696.

Zhao, Z. J., 1993, "A System for the Efficient Automated Analysis of Reconstructed Double-Pulsed Holograms." M.Sc. Thesis, Dept. of Mech. Eng., University of British Columbia.